6-27-2022

Climatology of Rainfall Distribution and Asymmetries of Tropical Cyclones: A Global Perspective

Oscar Guzman Rey
oguzm013@fiu.edu

FLORIDA INTERNATIONAL UNIVERSITY

Miami, Florida

CLIMATOLOGY OF RAINFALL DISTRIBUTION AND ASYMMETRIES OF TROPICAL CYCLONES: A GLOBAL PERSPECTIVE

A dissertation submitted in partial fulfillment of

the requirements for the degree of

DOCTOR OF PHILOSOPHY

in

EARTH SYSTEMS SCIENCE

by

Oscar F. Guzman Rey

2022

To: Dean Michael R. Heithaus
College of Arts, Sciences and Education

This dissertation, written by Oscar F. Guzman Rey, and entitled Climatology of Rainfall Distribution and Asymmetries of Tropical Cyclones: A Global Perspective has been approved regarding style and intellectual content, is submitted to you for judgment.

We have read this dissertation and recommend that it be approved.

_____
Hugh Willoughby

_____
Ping Zhu

_____
Arturo Leon

_____
Haiyan Jiang, Major Professor

Date of Defense: June 27, 2022

The dissertation of Oscar F. Guzman Rey is approved.

_____
Dean Michael R. Heithaus
College of Arts, Sciences and Education

_____
Andrés G. Gil
Vice President for Research and Economic Development
and Dean of the University Graduate School

Florida International University, 2022

ACKNOWLEDGMENTS

First, I would like to express my gratitude to Dr. Haiyan Jiang for her continuous support during the Ph.D. process in the past 4 years. Without her guidance, expertise, and above all patience, most accomplishments achieved today would not have been possible.

I also would like to give my sincere appreciation to the rest of my committee members: Dr. Hugh Willoughby, Dr. Ping Zhu, and Dr. Arturo Leon, as they generously provided their knowledge and insightful advice in various fields, which contributed greatly to this manuscript. In addition to my committee members, I would like to thank my fellow graduate students Adrian Lopez and Xinxi Wang. They provided useful and opportune comments on different aspects of this research.

This work was partially supported by the joint effort between the Fulbright Program and the National Science Foundation of Colombia (Colciencias). Without their logistic support, completing the objectives of my doctoral program in the United States of America would not have been possible.

Finally, I want to thank my wife Sandra, my mother Martha, my sister Tatiana, and my aunt Alicia for their constant encouragement during my time in graduate school. Especially for their gestures of unconditional support despite my absence during key moments of precious family time.

ABSTRACT OF THE DISSERTATION

CLIMATOLOGY OF RAINFALL DISTRIBUTION AND ASYMMETRIES OF TROPICAL CYCLONES: A GLOBAL PERSPECTIVE

by

Oscar F. Guzman Rey

Florida International University, 2022

Miami, Florida

Professor Haiyan Jiang, Major Professor

Estimating the magnitude of tropical cyclone (TC) rainfall at different landfalling states is an important aspect of the TC forecast that directly affects the level of response from emergency managers in coastal areas. This research analyses the spatial distribution of the rainfall magnitude in tropical cyclones (TCs) at different stages over global oceans. The research's central hypothesis is that TC rainfall exhibits distinct features in the long-term satellite dataset due to the evolution of the spatial distribution, radial variation, and asymmetries at the stages before, during, and after landfall. The resulting patterns are analyzed through a statistical approach that takes advantage of a 20-year global satellite database of rainfall retrievals from the TRMM/GPM constellation, with the aim to achieve two main objectives: 1) The first objective was to explore the global trends of TC rainfall rates using observational evidence provided by a satellite-based climatology. Results indicate there is an increasing trend in the global average TC rainfall rate of about 1.3% per year, with a more pronounced trend in the northern hemisphere than in the southern hemisphere. 2) The second objective was to examine the spatial distribution of the magnitude and axisymmetric intensity profiles of rainfall over the six TC-prone basins.

The obtained differences were quantitatively investigated in terms of geographic location, sub-regions within the storm, and TC intensities. Results indicate that major hurricanes in the Atlantic basin exhibit heavier inner-core rainfall rates than those in any other basins, and this difference is highly correlated to specific environmental conditions. Overall, with the achievement of the above-described objectives, this document identifies and summarizes the dominant factors that control rainfall distribution in global TCs, mainly focused on the differences during landfilling processes.

TABLE OF CONTENTS

CHAPTER PAGE

LIST OF TABLES

TABLE PAGE

LIST OF FIGURES

FIGURE PAGE

LIST OF ACRONYMS AND ABBREVIATIONS

ATL	Atlantic
CAPE	Convective Available Potential Energy
CAT 12	Category 1 and category 2 hurricanes
CAT 35	Category 3 to category 5 hurricanes
CDF	Cumulative Distribution Function
ECPA	East and central Pacific
EM	Electromagnetic
FOV	Field of View
IB	Inner rainband
IC	Inner core
ITCZ	Inter-Tropical Convergence Zone
NIO	North Indian Ocean
NWP	Northwest Pacific
OB	Outer rainband
PR	Precipitation Radar
PF	Precipitation Feature
RMW	Radius of maximum wind
RMR	Radius of maximum rainfall
SIO	South Indian Ocean
SPA	South Pacific
TC	Tropical Cyclone

TCPF	Tropical Cyclone Precipitation Feature
TD	Tropical Depression
TMI	TRMM Microwave Imager
TRMM	Tropical Rainfall Measuring Mission
TS	Tropical Storm
VIRS	Visible and Infrared Scanner

1. INTRODUCTION AND BACKGROUND

1.1 Tropical Cyclone Generalities

1.1.1 Tropical Cyclone Definition and Structure

A tropical cyclone (TC) is defined as a rotating storm system characterized by low central pressure and warm-core temperature structure that develops over the warm tropical oceans. The term tropical cyclone encompasses all the denominations given to systems whirling around their center, including the term “hurricanes” in the western hemisphere, “typhoons” in the northwestern Pacific Ocean, and “severe cyclonic storms” in the southern Pacific and the Indian Ocean. Tropical cyclones obtain their energy from the underlying warm waters, which means they are natural heat engines that release energy through moist adiabatic expansions that convert the stored latent heat into sensible heat. This thermodynamic behavior nearly follows the same principles of a Carnot Cycle used in steam engines.

The intensity of a TC is determined by its maximum sustained wind speed measured at a high of 10 meters above the surface over an average either over a 1-minute or 10-minute period, depending on the standards used on a particular region or weather agency. At their initial state, called Tropical Depression (TD), TCs exhibit a disorganized pattern of clustered storms that begin to follow a closed wind circulation with a maximum rotational speed up to 33 knots. Later, when the maximum 10-minute average wind is between 34 and 64 knots, the storm is named a tropical storm (TS), and finally, when a storm surpasses 64 knots, it is upgraded to a hurricane. In the case of the hurricanes occurring over the North Atlantic and East-Central Pacific basins, the Saffir-Simpson scale

is adopted; this scale ranges from categories 1 to 5 using intervals from 65-83, 84-95, 96-113, 114-134, and > 135 knots, respectively.

At their mature state, all tropical cyclones exhibit common structural elements: 1) The boundary layer inflow, 2) eyewall, 3) cirrus shield, 4) rainbands, and 5) the upper-tropospheric outflow. An oversimplified description of the airflow in a tropical cyclone would be that the air spirals rise from the surface to the tropopause along the eyewall and then through the spirals outward from the eyewall at tropopause levels. In general, the hurricane literature describes two types of circulations: the primary and the secondary. The primary circulation accounts for the horizontal movements produced by the force balance between the pressure gradient force, the centrifugal force, the Coriolis force, the centrifugal force, and the friction (figure 1.1a). As a resulting balance, winds spiral towards the storm center clockwise in the southern hemisphere and counterclockwise in the northern hemisphere. Another interesting feature of the primary circulation is that storm intensity is higher in the right side of the eye relative to the translation direction. Figure 1.1a shows how the translational speed adds strength to the eastern side and removes the same amount from the storm's western side. This situation is well known for mariners who differentiate the hurricane features between the two sides as a risk function (figure 1.1b). Figure 1.1b also shows some key elements distinguishable in primary circulation plots, such as the radius of maximum wind, maximum precipitation, and the rainbands. Further discussion and definition of these elements will be developed in the next sections of this document.

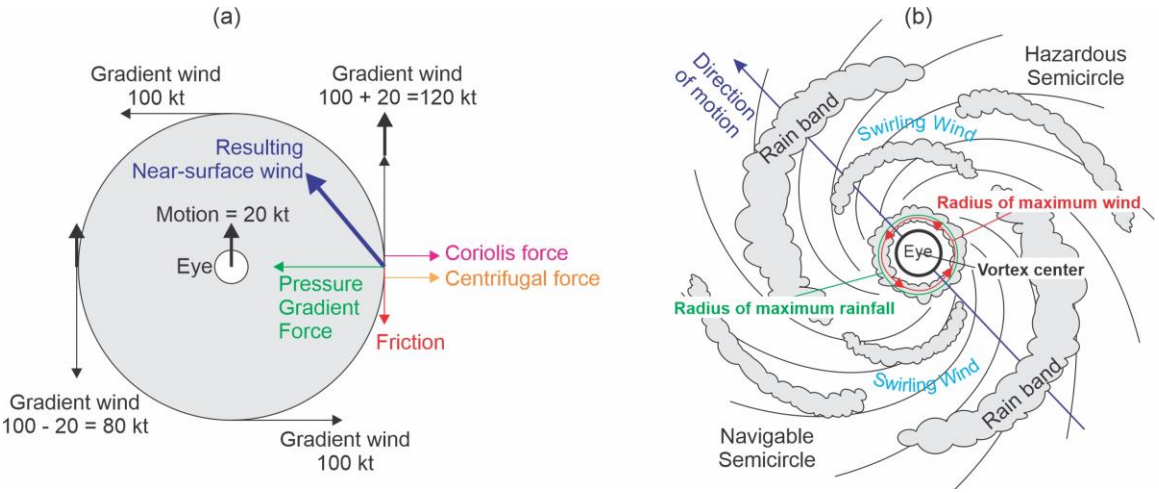

Figure 1-1: Illustration showing the primary circulation of TCs. a) force balance between pressure gradient, centrifugal, Coriolis, and friction forces. Diagram also shows an example explaining why winds are stronger on the right side. b) Typical features observed in a primary circulation plot, including the eye, rainbands, and radius of maximum wind.

Tropical cyclones also have a secondary circulation that accounts for the vertical flows that relates the eye, spiral bands, and transitional regions. This circulation is shown in a cross-section in figure 1.2. The top portion of the figure shows the wind patterns in a typical hurricane. Here, the air in the upper and middle troposphere descends within the eye but does not descend completely to the ocean surface. Instead, the base of descending air is determined by an inversion responsible for the appearance of small clouds visible at the base of the eye in some hurricanes. In the eyewall, air ascends from the surface to the tropopause and can no longer rise further. As a result, most air exhausts outward away from the center, creating a large shield of clouds visible on satellite images. Other secondary circulations involve the rainbands where some of the air converging towards the center of the hurricane rises along preferred regions. These zones spiral out from the center and coincide with the location of the spiral bands.

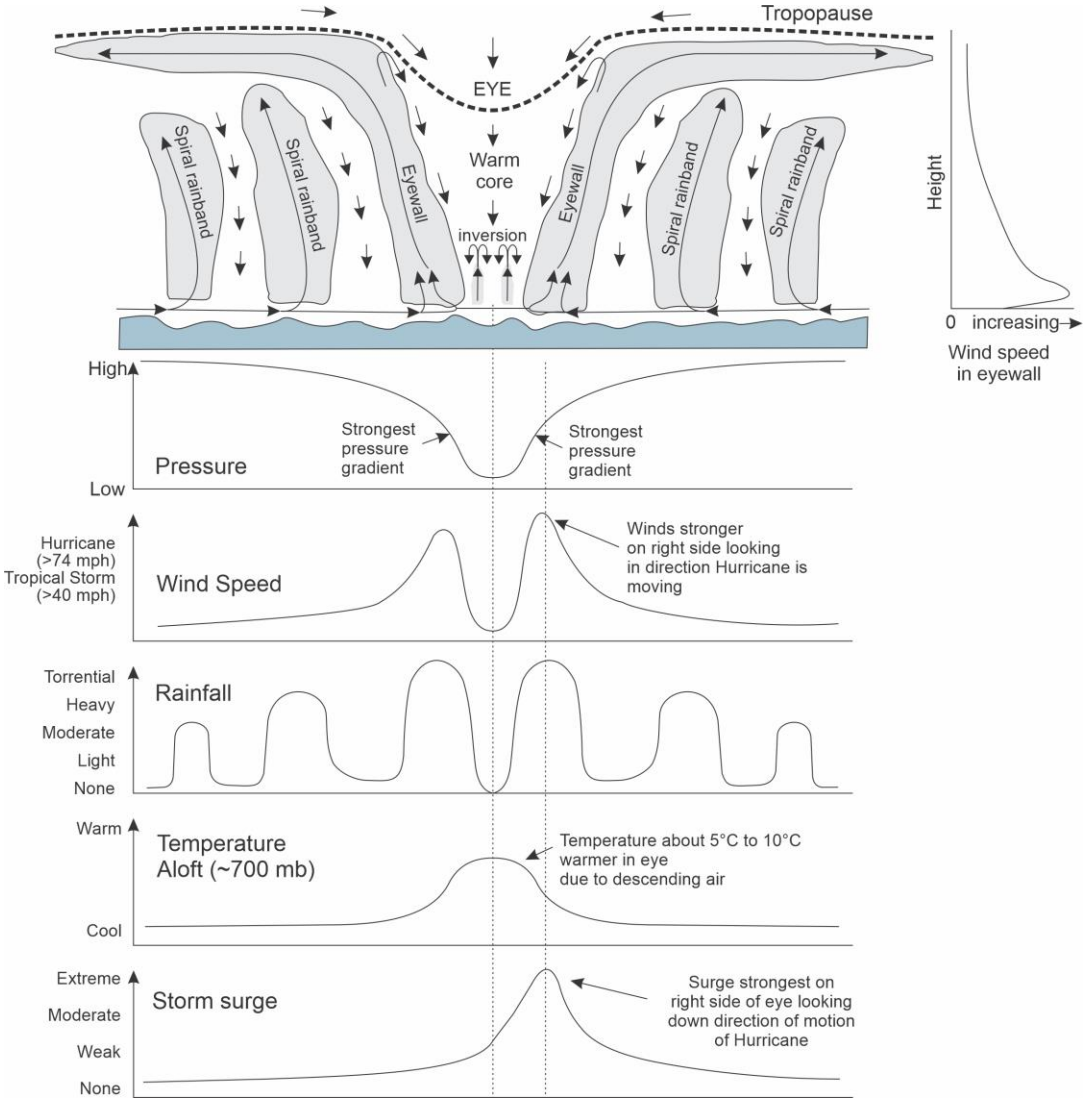

Figure 1-2: Cross-section through a hurricane showing hurricane structure and typical behavior of pressure, wind speed, rainfall, temperature, and storm surge. Awaiting permissions from *Severe and Hazardous Weather: An introduction to high impact meteorology*, *Fifth Edition*, R. Rauber, p. 477.

Figure 1.2 also describes how the pressure, wind speed, rainfall, temperature, and storm surge vary across the tropical cyclone structure. In terms of pressure, it drops slowly at first but then decreases rapidly as it gets closer to the eye, particularly in the eyewall region. This strong pressure gradient is responsible for the most intense winds within the storm, confined to the eyewall and its neighboring regions. From Figure 1.2, it can be noticed that inside the eye, winds are nearly calm, and wind speeds are higher on the right

side of the eye. The diagram to the right of the first panel describes the variation of wind speed with height within the eyewall. In terms of the storm surge, its intensity is favored by the strongest winds on the right side of the hurricane, this looking in the direction the storm is moving.

Finally, in the case of rainfall intensity, it varies across the storm structure similarly to the wind speed intensity but at a slightly slower pace, with interspersed events of rain and no-rain as the availability of rainbands. Moderate to heavy rainfall can fall within the rainbands, with higher rain typically occurring in the inner-most spiral bands. No rain falls in the eye. When viewed from radar, the hurricane's precipitation patterns become more evident. Two elements are the most distinct, a ring of heavy precipitation within the eyewall and spiral rainbands that extend outward for several kilometers until the outermost part of the storm. These two elements are the key to understanding the precipitation field within the tropical cyclone structure. Further details about the appearance of tropical cyclone features in remote sensing data will be presented in the following sections.

1.1.2 Geographic Distribution of Tropical Cyclones

Areas of tropical cyclones formation are distributed across global oceans from a few degrees of North or South latitude until mid-latitudes. Tropical cyclones do not form very close to the equator (Figure 1.3). Since the track of tropical cyclones can affect several countries, a transnational approach is required to monitor and provide early warnings. The World Meteorological Organization (WMO) has designated official forecasting centers to coordinate the surveillance responsibilities across the following six global basins: North Atlantic (ATL), East and Center Pacific (ECPA), Northwestern Pacific (NWP), North

Indian Ocean (NIO), South Indian Ocean (SIO), and South Pacific Ocean (SPA). Under unusual circumstances, the South Atlantic is considered an eighth basin; however, it is usually omitted from the hurricane literature due to its very low occurrence. Figure 1.3 shows the geographic distribution and traditional boundaries used to differentiate between basins. According to NOAA's National Hurricane Center, approximately 69 percent of the tropical cyclones occur in the Northern Hemisphere, while only 31 percent can be found in the Southern Hemisphere. Approximately 12 percent occur in the Atlantic Ocean, 57 percent occur in the Pacific, and the remaining 31 percent occur in the Indian Ocean.

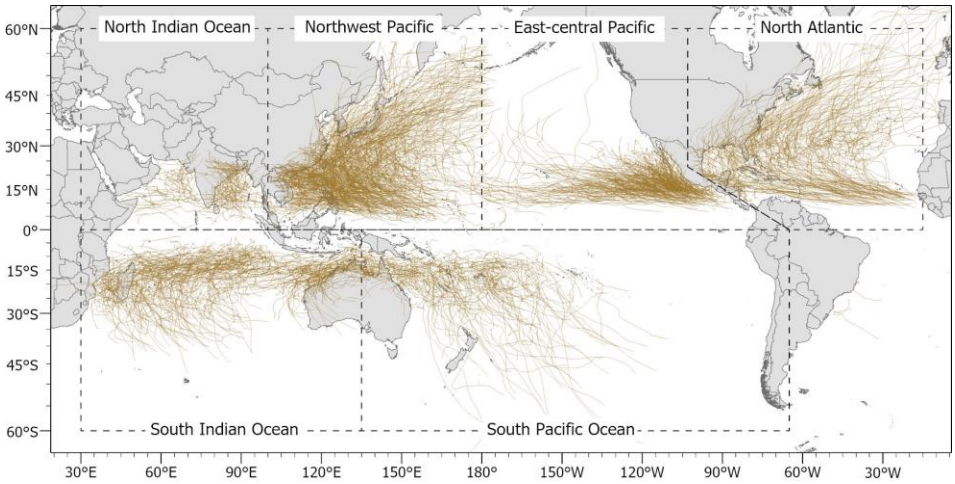

Figure 1-3: Tropical cyclone formation regions and WMO traditional basin division. Tracks are obtained from a subset of the International Best Track Archive (IBTrACS) in the period 1998-2020.

In terms of frequency, each basin experience seasons at different times. In general, global basins have their peak during the summer months except for NIO, where the TCs tend to occur during both the early and late transitions of the monsoon cycle, in May-June, and October-November respectively. Figure 1.4 shows the frequency of TC events for the six global basins. In the ATL basin, the TC season spans from June to November with a well-defined peak in September; in the ECPA region, the TC season is from May to

November with a peak in August; in the NWP basin, there is a continuous TC season along the year, with more frequent events from May to December and a peak in August. In the case of the two southern hemisphere basins, their TC season begins in October and ends in May, which means that their TC season does not fit within a regular calendar year. For instance, Hurricane Zoe is the sixth storm of the 2003 season (2003-06), but its lifetime spans from December 12th, 2002, to January 02^{nd,} 2003. In other words, TC season in the southern hemisphere starts in October of the previous year until May the current. From figure 1.4, It can also be noticed that NWP and NIO are the most active and the less active basins, respectively.

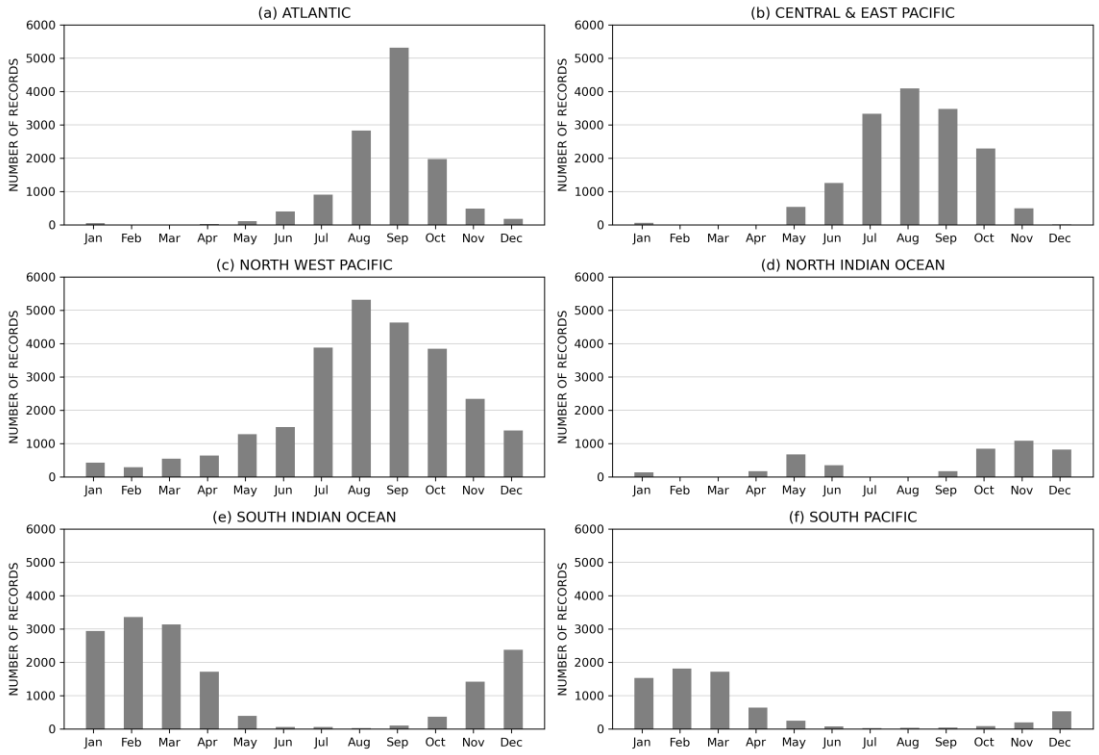

Figure 1-4: Monthly distribution of Tropical cyclone events during 1998-2020 as derived from NHC and JTWC agencies reported in the International Best Track Archive (IBTrACS). Each panel represents the frequency of Best Track positions in a) Atlantic, b) Central and east pacific, c) Northwest pacific. d) North Indian Ocean, e) South Indian Ocean, and f) South Pacific Ocean.

1.1.3 Tropical Cyclone Contribution to Global Rainfall Balance

Rain is the main source of fresh water that supports the subsistence of all kinds of life across Earth's landscapes. Controversially, the study of rainfall distribution at a global scale was poorly understood for many decades, especially over the oceans. However, since the beginning of the space era, significant advancements have been made to tackle this problem because of the development of remote sensing techniques that allow global hydrometeors detection. The overall geographic distribution of rainfall rates is shown in Figure 1.5a. as derived from data recorded by the NASA Tropical Rainfall Measuring Mission (TRMM) and its successor, the Global Precipitation Mission GPM. From this figure, it can be noticed that precipitation near the equator is the highest due to the heavy rainfall patterns triggered by the influence of the Inter-Tropical Convergence Zone (ITCZ). Thus, extreme precipitation values are very localized in places like the west coast of Colombia, New Guinea, Indonesia, Sumatra, and certain regions in west India. In contrast, droughts tend to be widespread over vast areas like the eastern Pacific, eastern Atlantic, and dessert areas near the 30 degrees of latitude (South and North), where the equatorial air begins to descend through the Hadley cells.

TC rainfall is mostly concentrated in the belts between 10 to 20 degrees of latitude in both hemispheres (Figure 1.5b), with clusters of very high concentration in the east coast of the Philippines in NWP and the west coast of Mexico, near Isla Socorro in the ECPA basin. TC rainfall across other global basins is fairly spread over each basin extension with more accumulation over open ocean areas with the absence of big islands. In terms of the TC rainfall contribution to the total rainfall balance, Figure 1.5c shows the TC rain percentage. It indicates that the maximum percentages are located either at the same place

where the TC-rain itself is concentrated (ATL, NWP, SIO, and NIO) or even more poleward than the TC-rain (ECPA, NIO, and SIO). The peak of the TC rain is located in ECPA, with a contribution near 58%.

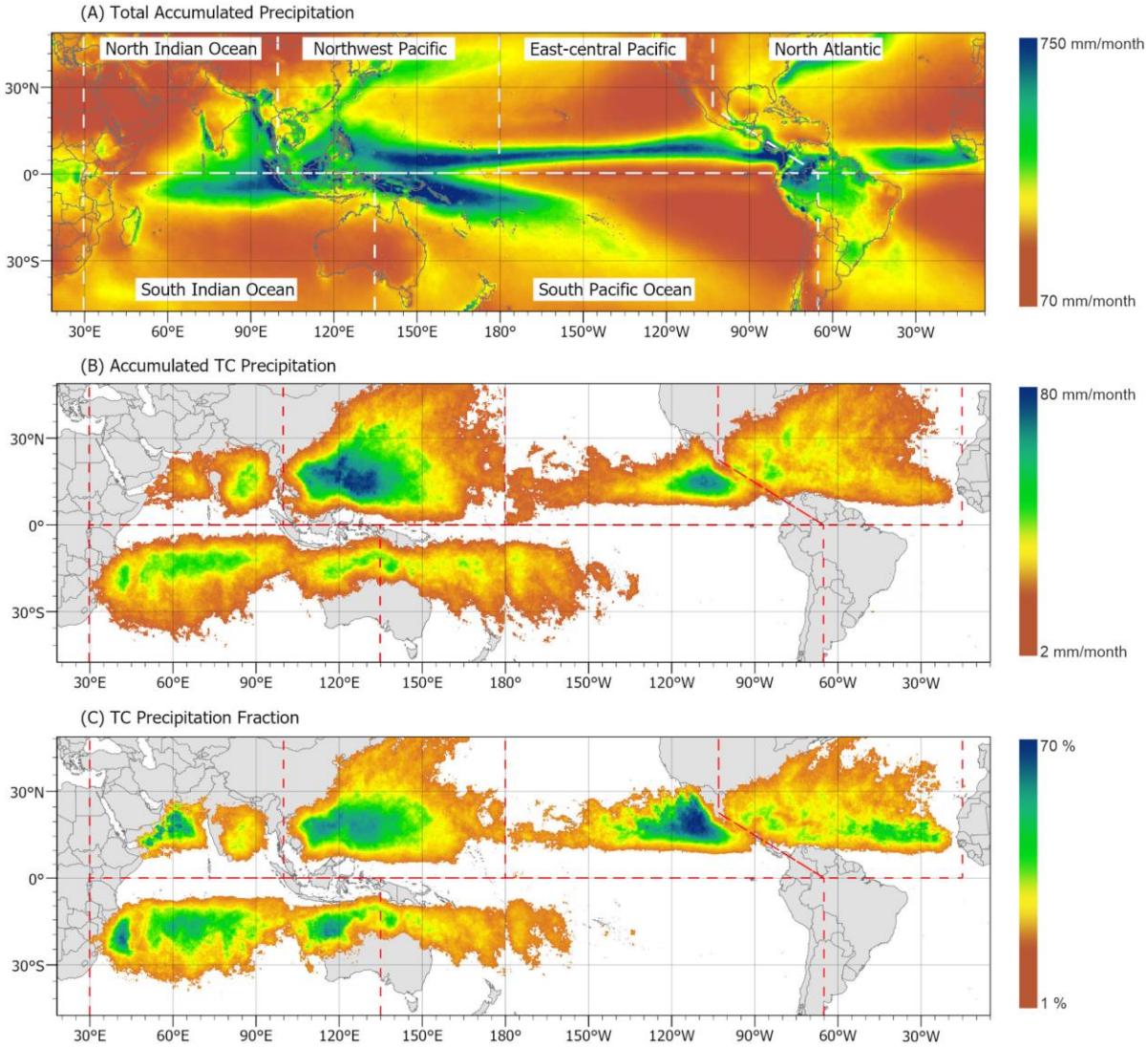

Figure 1-5: Maps showing the contribution of TC rainfall to the global water balance. a) Global distribution of total precipitation, b) rainfall produced by tropical cyclone precipitation, and c) tropical cyclone precipitation fraction. Computations are for the period 1998-2016 using satellite data.

In a closer look at each basin's particularities, the Atlantic basin shows that both accumulated TC-rainfall and the percent of their contributions are not distributed homogeneously across the region. There are two main distinguishable areas (Figure 1.6a).

The first area extends from the Cape Verde basin to 60°W longitude (the right flank of the Lesser Antilles), where the TCs travel across the open ocean without the interference of landmasses. In this zone, the TCs contribution smoothly oscillates between 15% and 25% within its maxima on an axis slightly tilted northwestward between 15° and 18°N latitude. The second area extends from 60°W longitude to the eastern coast of the Americas; in this zone, TCs interact with several islands and the continent itself, a situation that leads to an intricate precipitation pattern, in which the TC-rain maxima tend to be positioned over open waters and gradually reduce as the TC approaches shallow waters and continental landmass. In the Gulf of Mexico zone, the precipitation cluster seems highly correlated with the oceanic circulation pattern described by the Loop Current. However, further research is required to understand the influence and mechanisms of this feature in the TC rain produced over this area.

The Northwestern Pacific basin has the highest accumulation of TC-induced rain due to more frequent events. Maximum accumulation occurs from 134°W to the eastern coast of the Philippines and south of Taiwan, in the belt between 11° and 22°N. In terms of precipitation fraction, NWP shows a well-defined distribution characterized by a rainier region confined between 146°W (in the vicinity of the Mariana-Izu-Japan trench) and west coast of China-Vietnam, with two main concentrations separated by the Philippines, Taiwan, and the chain of islands between them (Figure 1.6b). Both peaks have TC contributions of approximately 32% relative to the total accumulated precipitation. Across the NWP basin, TCs also interact with major islands. The reduction of the TC rainfall is distinguishable due to the influence of Luzon (Philippines), Hainan (China), and Taiwan.

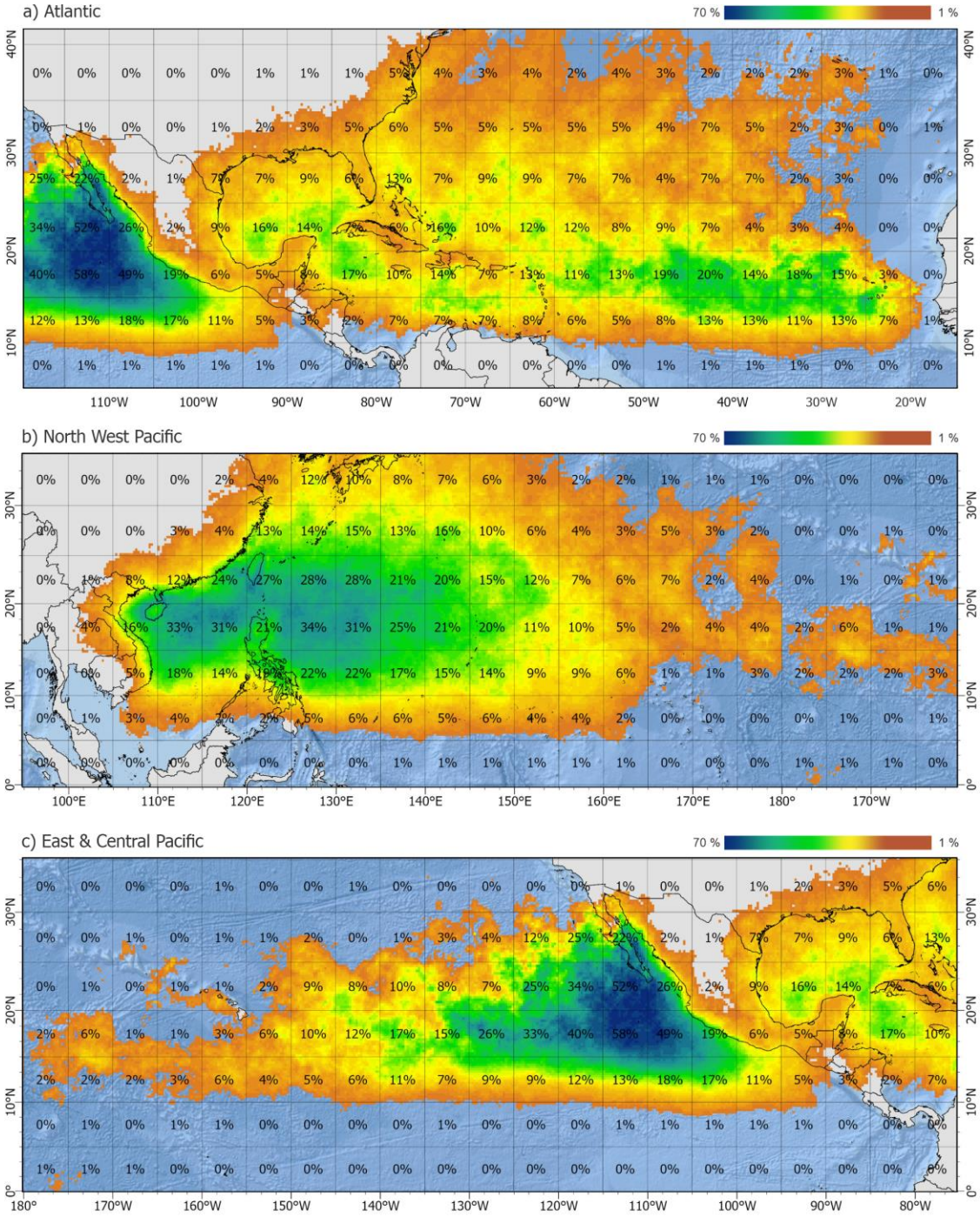

Figure 1-6: Maps showing the contribution of TC rainfall in a) Atlantic, b) Northwest Pacific, and c) East and Central Pacific. Percentages on top of the map represent the averaged contribution over a grid of 5° x 5° for the period 1998-2016 using satellite data.

TC rainfall produced in the Central and East Pacific basin is highly concentrated on the southwestern Mexican coast (Figure 1.6c). This basin has the second largest peak of

accumulated TC precipitation, behind NPW, as well as the maximum local precipitation contribution out of all of the global basins (more than 58% near the Isla Socorro). For most of this region, TC rainfall is unaffected by landmasses except for those hurricanes following tracks parallel to the Mexican coast or crossing near the Hawaiian Islands. The absence of major islands might be one of the reasons for the high concentration and homogeneity of TC rain.

In the Northern Indian Ocean, there are two active TC rainfall areas separated by the landmasses of India and Sri Lanka. In the first cluster, located over the Bay of Bengal, accumulated precipitation tends to be more concentrated westward over the influential area of the East Indian Coastal Current (EICC), with a contribution of 13% with respect to the total precipitation. The second cluster is located over the Arabian Sea with a much lower TC rainfall accumulation; however, it has a higher contribution (23%) due to the dry precipitation regime near the coast of Oman and Yemen (Figure 1.7a).

TC rainfall produced in the Southern Indian Ocean is concentrated in three different geographic areas; the northwestern coast of Australia, the zone between the Mid- Indian Ocean basin and the west coast of Madagascar, and the Mozambique Channel (Figure 1.7b). In the case of the first area, TC rainfall accumulation is concentrated from the Timor Sea westward, between the northwestern coast of Australia and the Java trench, with a maximum TC rainfall contribution of 27% near the Pilbara coast of Western Australia. The second area has the rainiest TC behavior from 88° to 50°E and from 9° to 20°S, with a uniform distribution and a TC rainfall contribution peak of 31% in its center. Last, the third area is confined between the west coast of Madagascar and the coast of Mozambique;

although this area has similar values of accumulated precipitation, its contribution is about 42% due to low precipitation trends in the zone.

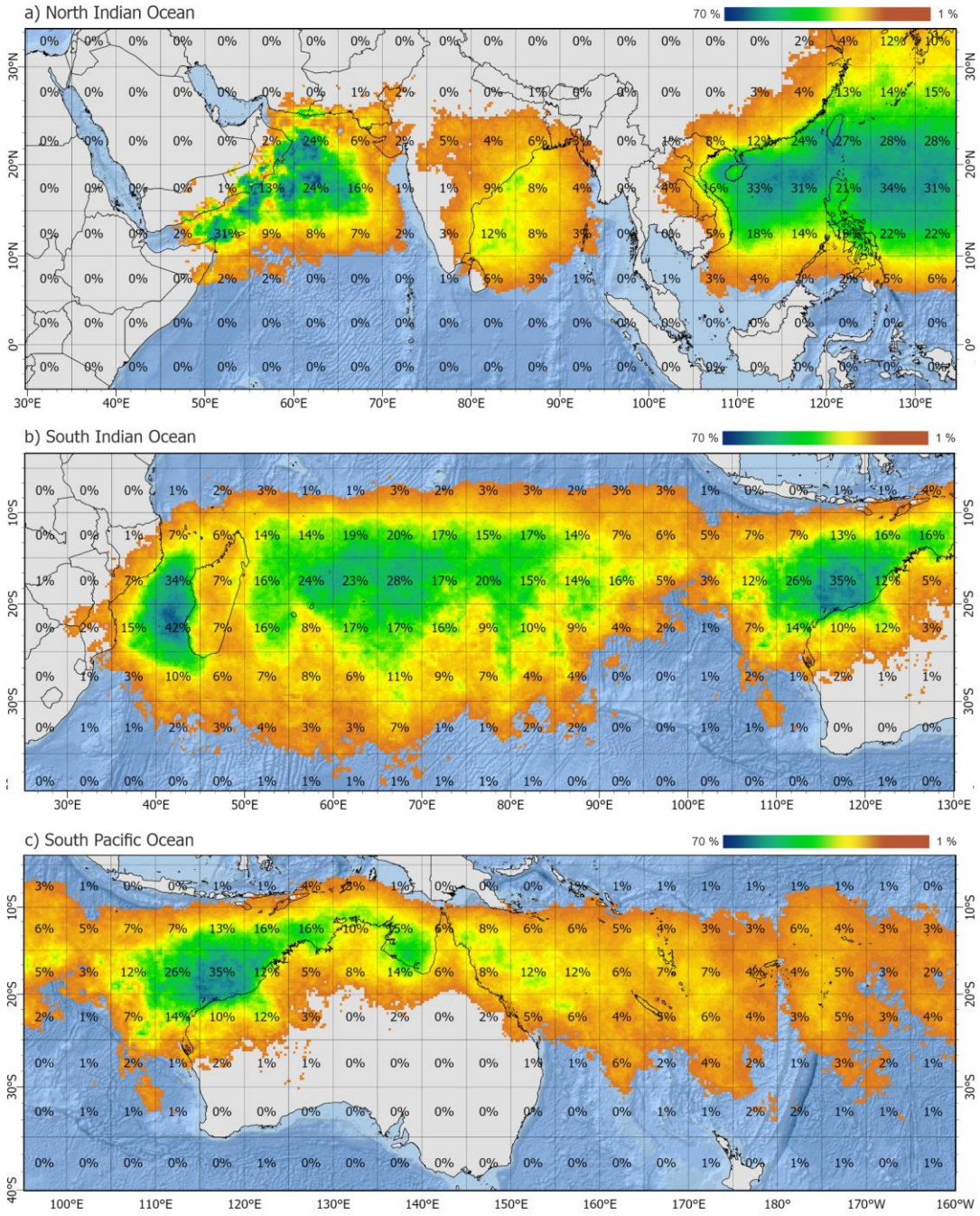

Figure 1-7: Maps showing the contribution of TC rainfall in a) North Indian Ocean, b) South Indian Ocean, and c) South Pacific. Percentages on top of the map represent the averaged contribution over a grid of 5° x 5° for the period 1998-2016 using satellite data.

Finally, the main TC rainfall region across the southern Pacific basin extends from 157°W to the eastern coast of Australia with three relative peaks over the open Pacific Ocean and one absolute peak over the waters of the Arafura Sea within the Gulf of Carpentaria (Figure 1.7c). Their percentual contributions are 6, 10, 13, and 19%, respectively. Although there are many islands in the western part, their influence is not as pronounced as in other basins.

1.1.4 Axisymmetric component Tropical Cyclone Rainfall

The reconstruction of the rain field produced by tropical cyclones requires analytic methods to describe the distribution of hydrometeors within the structure of the hurricane's swirling flows. A common assumption is to consider the rain field as an axisymmetric flow. This approach allows the construction of azimuthal averages describing the approximated radial distribution of the rainfall magnitude at any distance from the tropical cyclone center. Considering the gridded pattern of most remote sensing measurements, the calculation of radial azimuthally averaged rainfall rates is a consistent task that has served as input in several models and to draw conclusions on the high correlation between tropical cyclone intensity (wind) and the precipitation field (e.g., Rodgers and Pierce, 1995; Rodgers et al., 1994, Lonfat et al. 2004).

From the practical standpoint, the process is based on segmentation of the rainfall field in as many annuli as allowed by the spatial resolution of the satellite information. Then, for each individual annulus, the average rain is calculated either considering or ignoring zero values (conditional or unconditional averages) to have a metric of the precipitation behavior at the corresponding annulus radius. This procedure is equivalent to

the calculation of the wavenumber zero of the Fast Fourier Transformation. Figure 1.8 shows an example of the global axisymmetric decomposition of 1834 storms in the period 2000-2019 from satellite observations. In this example, it can be inferred that the rain field follows similar patterns to the wind analytical model proposed by Holland (1980).

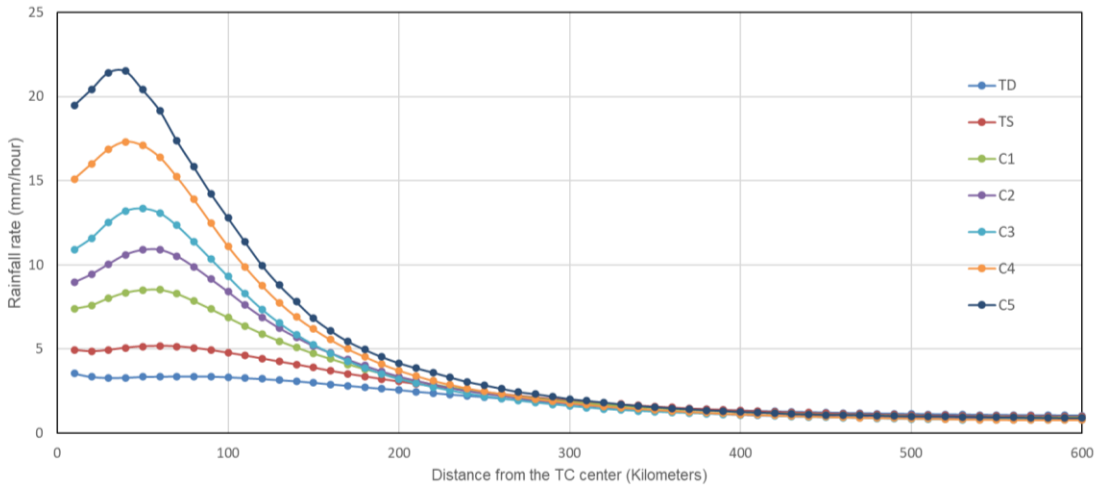

Figure 1-8: Example of the radial distribution of azimuthally averaged rainfall rate of global TCs during 2000-2019 in different intensity categories, using satellite data. TD represents Tropical Depression, TS – Tropical Storms, C1 to C5 correspond to the categories of the Saffir Simpson scale.

1.1.5 Tropical Cyclone Rainfall Anisotropies

High-resolution observations reveal that tropical cyclones can deviate from a perfectly axisymmetric pattern and become asymmetric. TC asymmetric features can be characterized using Fourier decompositions, in which the analysis of the wavenumbers provides the basis for asymmetries detection and quantification. As the first step of this procedure, satellite information is transformed from a geographic coordinate system into a polar system using the TC center as the origin. Next, the gridded observations are rotated relative to the storm motion and wind shear directions (Figure 1.9). Then the spatial

asymmetries are computed by binning the satellite information in steps with a size equivalent to the spatial resolution of the satellite information. Finally, in each annulus, the Fourier coefficients are computed using the following equations (Stull, 1987):

$$a_n = \frac{1}{N}\sum_{k=0}^{N-1} R(k)\cos\left(\frac{2\pi nk}{N}\right), \quad (1)$$

$$b_n = -\frac{1}{N}\sum_{k=0}^{N-1} R(k)\sin\left(\frac{2\pi nk}{N}\right), \quad (2)$$

Where *R(k)* is each of the individual rain rate estimates, and *n* is the wavenumber. *N* is equal to 360, which is the total number of points being analyzed in each annulus. N is also the highest wavenumber that we can resolve in this Fourier decomposition. *k* is the index of each point. The complex formula of Fourier coefficient c_n is:

$$c_n = a_n + ib_n, \quad (3)$$

where *i* is the imaginary unit, which is defined by its property $i^2 = -1$. Then the asymmetric rainfall component of wavenumber n, R_n, can be represented by:

$$R_n = a_n\cos\left(\frac{2\pi nk}{n}\right) - b_n\sin\left(\frac{2\pi nk}{n}\right), \quad (4)$$

Figure 1.9 shows an example of Fourier decomposition for hurricane Sudal (2004-03) when it was category four in the northwest pacific basin. Three panels at the top show the rainfall field relative to its geographic orientation, the direction of motion, and the wind shear vector. The remaining panels at the bottom represent the wavenumber 0, wavenumber 1, and the asymmetric component, respectively.

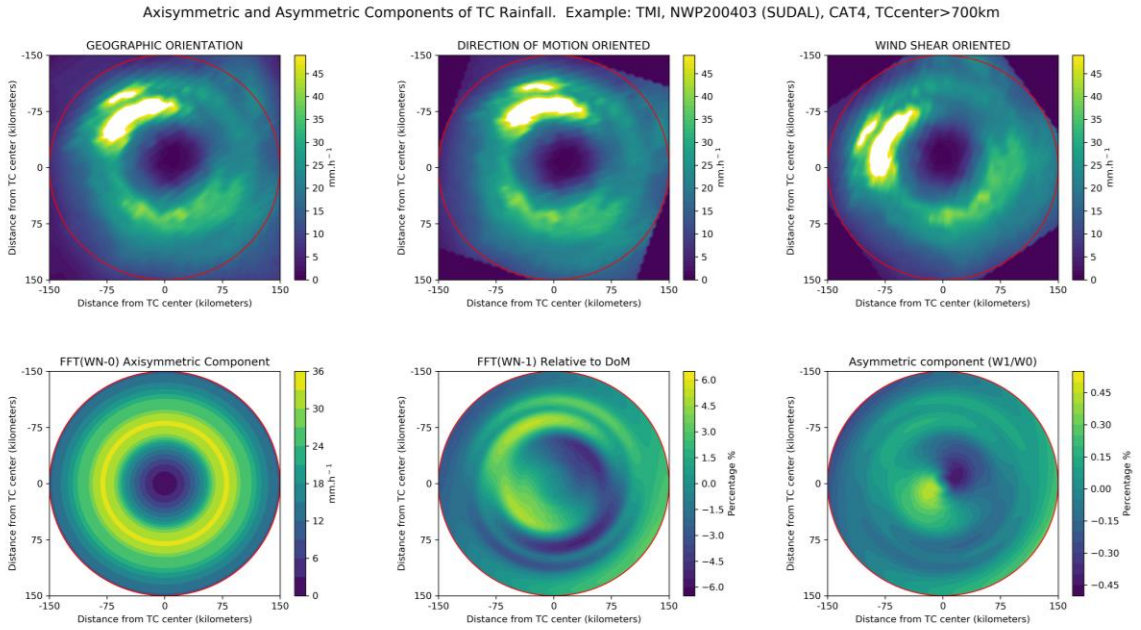

Figure 1-9: Example of Fourier decomposition for hurricane Sudal (2004-03) when it was category four in the northwest pacific basin. Three panels at the top show the rainfall field relative to its geographic orientation, the direction of motion, and the wind shear vector. The remaining panels at the bottom represent the wavenumber 0, wavenumber 1, and the asymmetric component, respectively.

1.2 Remote Sensing of Precipitation

1.2.1 Overview

Remote sensing is defined as the acquisition of information about an object without being in physical contact with it. Information is acquired by measuring the emitted or reflected electromagnetic radiation of the observed object. The term remote sensing is most commonly used in connection with electromagnetic techniques of information acquisition from airborne, unmanaged aerial vehicles or satellites. Considering the societal relevance of water, remote sensing of precipitation is one of the strategic priorities of the scientific community since it is one of the cornerstones in understanding water cycles in the global climate system. Remote sensing of parameters associated with precipitation is possible at

several wavelengths; however, microwave frequencies are preferred thanks to sensitivity to direct hydrometeor detection that can be used to infer important features such as size, distribution, and speed. Remote sensing techniques include two general approaches, passive and active. Active techniques involve the transmission of a pulse of energy and measuring the backscattered radiation produced by water droplets. In contrast, passive techniques measure the incoming natural radiation reflected, emitted, or transmitted by the hydrometeors.

1.2.2 Passive Microwave Remote Sensing of Precipitation

Passive microwave sensors have flown on both research and operational missions for over 40 years. They have the ability to penetrate through cirrus clouds and respond to liquid and frozen hydrometeors which are highly correlated to surface precipitation (Aonashi and Ferraro, 2020). A classification based on physical processes that govern the interaction of electromagnetic radiation with matter is commonly used for the research community, emission-based and scattering-based techniques. However, a formal description of those theoretical approaches is beyond the scope of this research and can be found in the traditional remote sensing literature (e.g., Kummerov, 2020). In addition, two types of sensors are used in passive microwave remote sensing, imaging sensor and sounding sensors. For the specific purposes of this research, only imagers are described since the analysis of the precipitation field was performed in a 2D framework.

Microwave imagers (MWIs) are based on the observation of brightness temperatures mainly in the microwave spectrum; however, some MWIs also have additional channels used for retrievals of precipitable water content (22.3 GHz), Cloud

liquid content (23 and 37 GHz), rain over oceans (10-19 GHz), and frozen precipitation (89 GHz and higher). Table 1.1 presents a list of the major microwave imagers since the beginning of the satellite era, their corresponding frequencies, coverage, and spatial resolution. Unfortunately, MWIs still have coarse spatial resolution compared to other remote sensing systems due to their antenna size constraints, though the use of synthetic aperture antennas will become a reality in the coming decades.

Table 1-1: Major satellite with passive microwave imagers from 1970 to the present. Information adapted from Levizzani et al. and upgraded to date in this research.

Satellite / Launch year	Sensor	Frequencies	Swath width (km)	Highest horizontal resolution (km)
Nimbus5, 1972	ESMR	19.35	3,000	25 x 25
Nimbus6, 1972	ESMR	37	1,300	20 x 40
Nimbus7, 1972	SMMR	6.6, 10.69, 18, 21, 37	800	18 x 27
SEASAT, 1978	SMMR	6.6, 10.69, 18, 21, 37	600	14 x 21
DMSP5D2, 1987	SSM/I	19.35, 22.23, 37, 85.5	1,394	13 x 15
TRMM, 1997	TMI	10.65, 19.35, 21.3, 37, 85.5	759	5 x 7
Coriolis, 2003	WindSat	6.8, 10.7, 18.7, 23.8	950	8 x 13
Aqua, 2003	AMSR-E	6.29, 10.65, 18.7, 23.8, 36.5, 89	1,445	4 x 6
GCOMW, 2012	AMSR2	6.29, 7.3, 10.65, 18.7, 23.8, 36.5, 89	1,450	3 x 5
GMI, 2014	GMI	10.65, 18.7, 23.8, 36.5, 89, 165.5, 183	885	4 x 6

1.2.3 Active Microwave Remote Sensing of Precipitation

Active remote sensing, often referred to as radar, transmits EM pulses at known frequencies and measures the strength of the returned backscattering from cloud and precipitation particles. The signal returned to the radar receiver (called radar reflectivity)

provides a measure of the size and number of raindrops at multiple vertical layers in the atmosphere. Clouds are usually not detectable by most weather radars, as the radar echoes from clouds are very weak. Nevertheless, radars can detect rain and hails very easily, making them extremely useful for detecting local storms, mesoscale weather, and TCs.

The radar observes many raindrops or cloud particles simultaneously, so the power returned to the radar is the combination of the returns from all individual targets within the radar beam. Mathematically, this can be expressed as:

$$\sigma_t = \sum_{i=1}^{n} \sigma_i \tag{1.19}$$

where, σ_i is the individual backscattering cross-sectional area for all *n* particles, and σ_t is the total backscattering cross-sectional area of a meteorological target. The backscattering cross-sectional area of a target depends on the size, shape, kind of matter making up the target, and the wavelength of the radar viewing it. For most meteorological radars (wavelengths of 3 cm or larger), almost all precipitation hydrometeors can be considered small compared to the wavelength, where the Rayleigh approximation yields. Thus, the backscattering cross-sectional area of the i^{th} sphere, σ_i, can be simplified as:

$$\sigma_i = \frac{\pi^5 D^6}{\lambda^4} \left| \frac{m^2-1}{m^2+2} \right|^2 \tag{1.20}$$

where *D* is the diameter of a spherical target.

Another way to calculate the total backscattering cross-sectional area of targets (σ_t) is to multiply the backscattering cross-sectional area of a *unit* volume by the total sample volume (*V*), which is given by:

$$\sigma_t = V \sum_{vol} \sigma_i \tag{1.21}$$

Here, $\sum_{vol} \sigma_i$ is the summation of the individual backscattering cross-sectional area over a *unit* volume, most known as radar reflectivity η. For Rayleigh scattering, the radar reflectivity is expressed by:

$$\eta = \frac{\pi^5}{\lambda^4} \left| \frac{m^2-1}{m^2+2} \right|^2 z \tag{1.22}$$

Here, *z* is called the radar reflectivity factor, defined as:

$$z = \sum_{vol} D^6 = \int_0^\infty N(D) D^6 dD \tag{1.23}$$

where *N(D)* is the function of the drop size distribution (DSD).

One of the advantages of using the radar reflectivity factor, *z*, instead of radar reflectivity η, is that the radar reflectivity factor only depends on the number and sizes of the raindrops and is independent of the radar's wavelength. The term "reflectivity" used in this study represents the "radar reflectivity factor". Reflectivity can range from very small values such as in fog ($\sim 0.001 mm^6/m^3$) to very large values such as in very large hail ($> 30{,}000{,}000\ mm^6/m^3$). For this reason, the logarithmic radar reflectivity, *Z*, is more commonly used in meteorology, which follows:

$$Z = 10 log_{10} \left(\frac{z}{1 mm^6/m^3} \right) \tag{1.24}$$

where *Z* is measured in units of dBZ (decibels relative to a reflectivity of 1 mm^6/m^3) and *z* is the linear radar reflectivity factor in mm^6/m^3. Typical weather radar measures reflectivity ranging from -20 to 70 dBZ.

1.2.4 The TRMM and GPM Missions

The Tropical Rainfall Measuring Mission (TRMM) satellite, a joint mission between the United States and Japan, was primarily proposed to provide precise

measurement of rainfall over global tropical and subtropical regions, where more than two-thirds of global precipitation occurs (Simpson et al. 1988). The satellite was equipped with two main sensors: 1) The TRMM Precipitation Radar (PR) was a 13.8 GHz (wavelength of 2.17 cm) electronically scanning radar that constructs a three-dimensional observation of precipitation along its path. It was also the first spaceborne radar, with a vertical resolution of 250 m from the surface up to a height of 20 km. The TRMM satellite was boosted in August 2001 to extend its lifetime; and 2) The TRMM Microwave Imager (TMI) was a nine-channel passive microwave radiometer, operating at frequencies of 10.65 GHz, 19.35 GHz, 21.3 GHz, 37.0 GHz, and 85.5 GHz. Dual polarization at all frequencies except 21.3 GHz, which is vertically polarized only.

The Global Precipitation Measurement (GPM) mission follows the successful TRMM (Kummerov et al. 1998, 2000), with some improvements. While the latitudinal range of TRMM observations was from 35°N to 35°S, GPM expanded coverage to 65°N to 65°S to cover 91% of the globe. Besides, to increase the ability to measure frozen and light precipitation, the GPM radar (called DPR) consists of a 13.6 GHz Ku-band radar similar to PR and a new 35.5 GHz Ka-band. In terms of the microwave imager, GPM includes a 13-channel sensor in the same TMI frequencies, plus two additional high frequencies bands at 165.5 GHz and 183.31 GHz. Since frequent sampling over the entire globe cannot be achieved by only one satellite, an international constellation of space-borne passive microwaves is employed to fill the Spatio-temporal gaps of the GPM-Core satellite; this is possible thanks to the non-sun synchronous nature of the GPM allowing frequent cross-calibration with the observations of the other satellites of the constellation. Therefore, by combining the observations from the GPM-core, the microwave imagers from the

satellite constellation, and infrared data from geostationary satellites, two representative high temporal and spatial resolution mapped products are publically available for various applications; these products are called 3B42 and IMERG.

1.2.4.1 TRMM Multi-satellite Precipitation Analysis (TMPA/3B42)

The TRMM Multi-satellite precipitation analysis (TMPA) is a precipitation retrieval that merges microwave precipitation estimates and variable rain rate infrared measurements to create a mosaic with a 3-hour temporal resolution and a 0.25-degree by 0.25-degree spatial resolution in a global belt extending from 50 degrees South to 50 degrees North latitude. The 3B42 estimates are produced in four stages (Huffman et al. 2007): 1) the microwave precipitation estimates are calibrated and combined, 2) infrared precipitation estimates are created using the calibrated microwave precipitation, 3) the microwave and IR estimates are combined, and 4) rescaling to monthly data is applied. Each precipitation field is best interpreted as the precipitation rate effective at the nominal observation time (Huffman et al., 2007).

As its input datasets, 3B42 merges passive microwave data collected by nearly polar satellites, including the sensors SSM/I, SSMIS, AMSR-E, AMSR-2, and the AMSU-B. Each individual satellite provides very sparse sampling, requiring their combination to reduce the gaps in the creation of global composites. Raw values of the microwave fields are converted to precipitation by specific versions of the Goddard Profiling Algorithm (GPROF) originally proposed by Kummerov et al. 1996; and Olson et al. 1999. In the particular case of AMSU-B precipitation estimates uses the Zhao and Weng (2002) and Weng et al. (2003) algorithms. The second data source are the infrared data recorded by

international geostationary satellites resampled to 4 km x 4km with a temporal resolution of 30 minutes. The IR brightness temperatures are corrected by zenith-angle viewing effects and intersatellite calibration differences (Janowiak et al. 2001). Finally, 3B42 also makes use of retrievals from the TRMM and GPM algorithms that combine TMI/GMI and PR/DPR measurements.

1.2.4.2 Integrated Multi-satellite Retrieval for the Global Precipitation Measurement Mission (IMERG)

The Integrated Multi-Satellite Retrieval for the GPM mission is a precipitation retrieval intended to inter-calibrate, merge, and interpolate all available satellite microwave estimations, precipitation gauge analyses, and other precipitation estimators to produce a fine product covering the entire globe. IMERG is computed three times for each observation time, first providing an initial estimate and then successive refined estimations as more data is available to improve de calculations. The final product, employed in the current research, is improved by using gauge data to create a consistent and research-level precipitation retrieval. This product is usually available 3 to 4 months after the observation day.

The IMERG product is assembled from 5 main sources of information: 1) The GPM core, in which the microwave imager is used as the reference for the inter-calibration with other satellite microwave imagers. The GPM core also carries the DPR, which is the key to the inter-calibration process that uses the Combined radar-radiometer algorithm proposed by Olson et al. (2001). 2) The second source is the precipitation microwave constellation, including satellites listed in Table 1.1 and some microwave sounders.

Observations from all these sensors are processed using the Goddard Profiling algorithm (GPROF) proposed by Kummerov et al. (2015). 3) The third input is the geostationary infrared satellite constellation, including the US geostationary GOES satellites, the Japanese Himawari, and the European Meteosat series. The data are processed into a precipitation retrieval using the Remotely Sensed Information using Artificial Neural Networks – Cloud Classification System (PERSIAN-CCS) proposed by Hong et al. (2004). 4) the Fourth source of information is the rain gauge analysis produced and maintained by the Deutscher Wetterdienst (DWD) Global Precipitation Climatology Center (GPCC) that uses the method proposed by Becker et al. (2013) and Schenider et al. (2014). And 5) Finally, some ancillary products describing the Earth's surface type from NASA, NOAA, and ECMWF analysis, are also considered.

1.3 Outline

This dissertation consists of three main sections, each addressing separate but related issues involving the climatology of tropical cyclone precipitation across global basins. The first section (chapter 2) uses a global database of TCs to study the trends in the overall precipitation rates in each TC-prone basin. The resulting trends are analyzed in terms of magnitude and compared to environmental conditions around the storms. The distinction between the trends at the inner-core level vs. rainband is presented to explain the dynamics within these two regions within the tropical cyclone structure. The second section (chapter 3) focuses on describing precipitation characteristics with climatological significance at different landfalling stages. TC rainfall magnitude is analyzed before, during, and after landfall; then stratified as a function of the net precipitating area, total volumetric rain, and

mean areal rainfall rate. Results are also analyzed in light of environmental conditions and TC itself parameters. Finally, the third section (Chapter 4) compares the axisymmetric component of the inner core TC region across the global basins and explains the inner-core variability based on the analysis of the tropical cyclone environment.

2. GLOBAL INCREASE IN TROPICAL CYCLONE RAIN RATES.

2.1 Abstract

Theoretical models of the potential intensity of tropical cyclones (TCs) suggest that TC rainfall rates should increase in a warmer environment but limited observational evidence has been studied to test these hypotheses on a global scale. The present study explores the general trends of TC rainfall rates based on a 19-year (1998–2016) time series of continuous observational data collected by the Tropical Rainfall Measuring Mission and the Global Precipitation Measurement mission. Overall, observations exhibit an increasing trend in the average TC rainfall rate of about 1.3% per year, a fact that is contributed mainly by the combined effect of the reduction in the inner-core rainfall rate with the increase in rainfall rate on the rainband region. We found that the increasing trend is more pronounced in the Northwestern Pacific and North Atlantic than in other global basins, and it is relatively uniform for all TC intensities. Further analysis shows that these trends are associated with increases in sea surface temperature and total precipitable water in the TC environment.

2.2 Introduction

Over the last decades, precipitation associated with tropical cyclones (TCs) has received more and more attention from the scientific community because of its potential to trigger freshwater flooding and landslide events that have caused the loss of lives and immeasurable damages in coastal areas (e.g., Willoughby 2012; Rappaport 2000, 2014;

Park et al. 2016). Current theoretical models suggest that TC potential intensity is expected to increase with the increasing global mean sea surface temperatures (Emanuel 1987; Holland 1997).

It has been reported that TC's destructive power has increased during the past few decades (Emanuel 2005), but it is still under debate whether the number and intensity of TCs have increased under global warming due to limitations in data availability of long-term homogenous TC records (Webster et al. 2005; Landsea et al. 2006; Kossin et al. 2007; Knutson et al. 2007). Nevertheless, numerical models have predicted that the increase in rainfall rates associated with TCs is an expected response of increased evaporation from the ocean surface and increased moisture in the atmosphere on global warming scenarios (Lin et al. 2015; Knutson et al. 2013; Villanari et al. 2014; Scoccimarro et al. 2017; Patricola and Wehner 2018). In the most recent Intergovernmental Panel on Climate Change (IPCC) report, Christensen et al. (2013) noted that an important majority of the models predict an increasing range between 5 and 20% with consistent results in all TC basins. That finding has received more support from the scientific community, as noted by the Knutson et al. (2020) in Part II of the Tropical Cyclone and Climate Change Assessment, in which they combined rainfall projections from multiple model-based studies to create an aggregate result of 14% TC rain rate increase for a 2 °C temperature increase, or broadly close to the rate of tropical water vapor increase expected for warming at constant relative humidity. Knutson et al. (2020) also suggested a lower confidence level of the TC rainfall rate increase for Southern Hemisphere basins.

However, the availability of continuous observations during long periods has limited the validation of these numerical predictions over TC-prone basins at a global scale.

Although previous research has not yet detected any global trends in TC rainfall rates (Peterson et al. 2014), Lau and Zhou (2012) found an increasing trend of total TC lifetime accumulate rain in the Atlantic and a decreasing trend in the northeast and northwest Pacific during two recent decades (1988–2007) using relatively low-resolution Global Precipitation Climatology Project (GPCP) data. They recognized that the total TC lifetime accumulated rain measure derived from the low-resolution rainfall data is not ideal and determining realistic trends of TC rain rates will require long-term (multi-decadal), high temporal (3-hourly or at least daily), and spatial resolution (25 km or less) rainfall data (Lau and Zhou 2012).

In this study, we examine how the TC rainfall rate has changed in all TC-prone basins, including Northern Atlantic (ATL), East & Central Pacific (ECPA), Northwestern Pacific (NWP), Northern Indian Ocean (NIO), Southern Indian Ocean (SIO), and Southern Pacific (SPA); using the 3-hourly, 0.25 × 0.25 degrees of the Tropical Rainfall Measuring Mission (TRMM) 3B42 data for almost two decades (1998–2016) derived from TRMM and Global Precipitation Measurement (GPM) missions. Globally, we found an increasing trend that is more pronounced in the northern hemisphere basins (except for the ECPA). Analysis of environmental parameters shows that these trends are associated with increases in sea surface temperature and total precipitable water that can affect the TC rainband environment. In contrast with the northern hemisphere, southern hemisphere basins show much smaller increasing trends due to slight variations of the environmental conditions in that part of the world. These results have important implications in understanding TC rainfall mechanisms and evaluating current climate models for future projections under a warming environment.

2.3 Data and Methods

2.3.1 Data

The time series cover the period from 1998 to 2016 including all the basins with TC activity. A total of 81,242 satellite observations are analyzed with the intensity categories and per-basin sample distribution shown in Table 2.1. Yearly samples oscillate between 3171 and 5315, with an average of 4232 observations per year (Table 2.2). TCs in the Southern Atlantic basin are excluded because of their unusual occurrence and insufficient sample size.

Table 2-1: Number of best track records (3B42 observations) for TCs during 1998-2016 in different TC intensity categories and different TC-prone basins.

Category/Basin	ATL	ECPA	NWP	NIO	SIO	SPA	Total
Tropical Depression	2,914	4,537	7,809	1,728	6,425	2,423	25,836
Tropical Storm	6,336	6,348	8,695	1,635	6,519	2,861	32,394
Category 1	2,073	1,732	3,438	264	1,746	767	10,020
Category 2	760	800	1,854	69	795	403	4,681
Category 3	589	642	1,506	101	800	344	3,982
Category 4	476	410	1,478	78	598	260	3,300
Category 5	125	64	595	33	97	115	1,029
Total	13,273	14,533	25,375	3,908	16,980	7,173	81,242

Precipitation information is extracted from TRMM 3B42 satellite estimations (version 7, Huffman et al. 2007) for the period from January 1998 to September 2014, and the transitional product that uses the new GPM constellation for the period from September 2014 to December 2016. This product was selected as the most extended available time series with homogeneous spatial-temporal data over tropical areas (3-hourly with 0.25° × 0.25° resolution), and it was used to characterize TC precipitation with the best possible climatological significance. TC characteristics, including location, time, and intensity, are

extracted from the International Best Track Archive for Climate Stewardship (IBTrACS version 4, Knapp et al. 2018); this database combines best-track records from different meteorological authorities on a global basis. Considering that some relevant parameters might present differences between reporting agencies, we privileged the information from the US agencies, particularly from the Joint Typhoon Warning Center (JTWC) for the TCs occurring in the Pacific Ocean Basins. Only storms in which the 3B42 extent covers the entire TC size area are considered. To meet this criterion, those best-track data points with TC centers located beyond 44°N and 44°S (about 660 km before the edge of the 3B42 border) are removed.

Table 2-2: Number of best track records (3B42 observations) for TCs during 1998-2016 in different years and different TC-prone basins.

Year/Basin	ATL	ECPA	NWP	NIO	SIO	SPA	Total
1998	850	956	1,050	310	1,271	745	5,182
1999	829	645	1,468	240	1,031	436	4,649
2000	709	922	1,623	175	1,285	340	5,054
2001	712	714	1,764	192	897	346	4,625
2002	615	869	1,803	153	989	249	4,678
2003	830	679	1,708	227	1,395	476	5,315
2004	908	539	1,820	247	1,059	192	4,765
2005	1,290	691	1,227	256	734	370	4,568
2006	537	880	1,274	129	729	375	3,924
2007	398	544	952	192	940	314	3,340
2008	812	678	992	229	1,154	201	4,066
2009	296	755	1,289	114	857	284	3,595
2010	842	352	701	202	558	516	3,171
2011	781	533	1,181	179	633	393	3,700
2012	916	642	1,354	112	899	268	4,191
2013	389	664	1,240	342	943	315	3,893
2014	316	1,161	1,080	209	617	384	3,767
2015	459	1,370	1,735	188	632	526	4,910
2016	784	939	1,114	212	357	443	3,849
Total	13,273	14,533	25,375	3,908	16,980	7,173	81,242

Sea surface temperature and total precipitable water estimations used to characterize the environmental conditions around the storms are extracted from the Statistical Hurricane Intensity Prediction Scheme (SHIPS, version available in July 2018). This developmental database includes estimations of a wide variety of environmental parameters over various annular regions calculated from the TC center (DeMaria and Kaplan 1994, 1999; DeMaria et al. 2005; Schumacher et al. 2013). For the current study, only the values for t = 0 are employed in our analyses. Reynolds sea surface temperature (RSST) and total precipitable water (TPW) are averaged between 0 and 500 km from the storm center.

2.3.2 TC rainfall determination.

The algorithm begins selecting the rain cells within the searching range from the 3B42 precipitation data with a spatiotemporal match to every 3-h position of the best-track data. Storms in the vicinity 50°N or 50°S are only included when they fully comply with the areal coverage criteria established by the searching range. As mentioned previously, in this study, we use storm-dependent definitions to define the total TC raining area and the inner-core raining area. In the TCPF framework (Jiang et al. 2011), to define the total TC raining area, a minimum value of precipitation rate must be used to group each PF or rain cell. Ideally, this threshold should be rain rate = 0 mm h^{-1}. However, the infrared or microwave rainfall retrievals in TRMM/GPM 3B42 are often contaminated by non-raining signals, especially for light rains in the retrievals. This contamination could cause problems in our TCPF identification. Therefore, we tested a few minimum values as the threshold to

define rain cells, including 0.01, 0.1, and 0.25 mm h^{-1}. The sensitivity test confirms that the rising global trend still presents in all scenarios. The intermediate value of 0.1 mm h^{-1} is chosen in this study. The average rainfall rates are calculated by considering the rain cells showing a precipitation rate over 0.1 mm h^{-1}. Zero values and non-data values are excluded from the calculations. Once each average is obtained for the corresponding TC region, a yearly average is calculated, and a set of time series is created for different intensity and different basin comparisons.

Additionally, an axisymmetric decomposition is performed to determine the radius of the maximum azimuthal rain rate (RMR) for each TRMM 3B42 TC observation. We find the RMRs by locating the rainfall rate maximum from the azimuthal mean values derived from the wavenumber zero of the Fourier transformation, as suggested in previous investigations (e.g., Lin et al. 2015; Lonfat et al. 2004). This RMR definition is the same as in Shimada et al. (2018) and Guzman and Jiang (2020). Then, a global time series with the yearly-averaged RMR values is created and processed using the same approach used for the total TC rainfall, inner-core, and outer rainband regions

2.3.3 Time series

The time series processing consists of simple linear regression analyses and statistical trend estimations using the Mann–Kendall test. For the linear regressions, time is used as the single predictor variable, and the corresponding regression equations and determination coefficients are calculated, including a verification of the normal distribution of the errors around zero. In the case of the Kendall test, the values of Kendall's tau and the p-values for the rejection or acceptance of the null hypothesis for different confidence

levels are reported. Sen's slope with their corresponding bounds at 95% of confidence is also part of the calculations for alternative interpretation concerning the linear regression with the presence of potential outliers.

The 5-year moving average was calculated in two steps: (1) Values from 2000 to 2014 result from the traditional method. For instance, the first averaged value is obtained by taking the average of a 5-values subset (2 before, current, and 2 after) shifting forward until the end of the time series. (2) In the case of 1998, 1999, 2015, and 2016, we use the moving average model (MA Smoothing Model) to estimate the most suitable values. In the process, we tested several q-values and determined that q = 2 is the best choice in all the cases. This value was selected by running the model over the entire series and then looking for the nearest series to the 5-year moving averages for 2000–2014. Finally, we included the modeled tails into the 5-year moving average to fully cover the period.

2.3 Global trends within the total TC rainfall area

Conventionally, the total TC rainfall area is defined by the 500 km radius threshold. This approach was used by several researchers in the previous studies (Larson et al. 2005; Jiang et al. 2011; Matyas 2013, 2014). The rationale behind this distance threshold is explained by the findings of Englehart and Douglas (2001), which indicates that in 90% of the TC cases, the distance between the storm center and the outer edge of its cloud shield is <550–600 km. However, we realize that the size of TCs can vary substantially across different basins, individual storms, and even within the lifetime of the same storm (Chavas and Emanuel, 2010). As suggested by Stansfield et al. (2020), a hard-coded radius of 500 km could overestimate TC-related overland precipitation. Therefore, in this study, we

define TC total raining area using a framework based on the concept of tropical cyclone precipitation features (TCPF, Jiang et al. 2011). In this TCPF framework, a precipitation feature (PF, or a rain cell) is defined by grouping contiguous pixels based on certain criteria. In this case, the criterion is a 3B42 rain rate >0.1 mm/h (see section "TC rainfall determination" for more details). To be qualified as a TCPF, the distance between the TC center and the geometric center of the PF must be <500 km. We compared the traditional simple truncation of 500 km radius from the TC center (Figure. 2.1a) and the TCPF-based TC total rain area definition (Figure. 2.1b). Although both methods exhibit similar and consistent results, our findings focus on the TCPF approach since this provides a better estimation of the TC size (Jiang et al 2011).

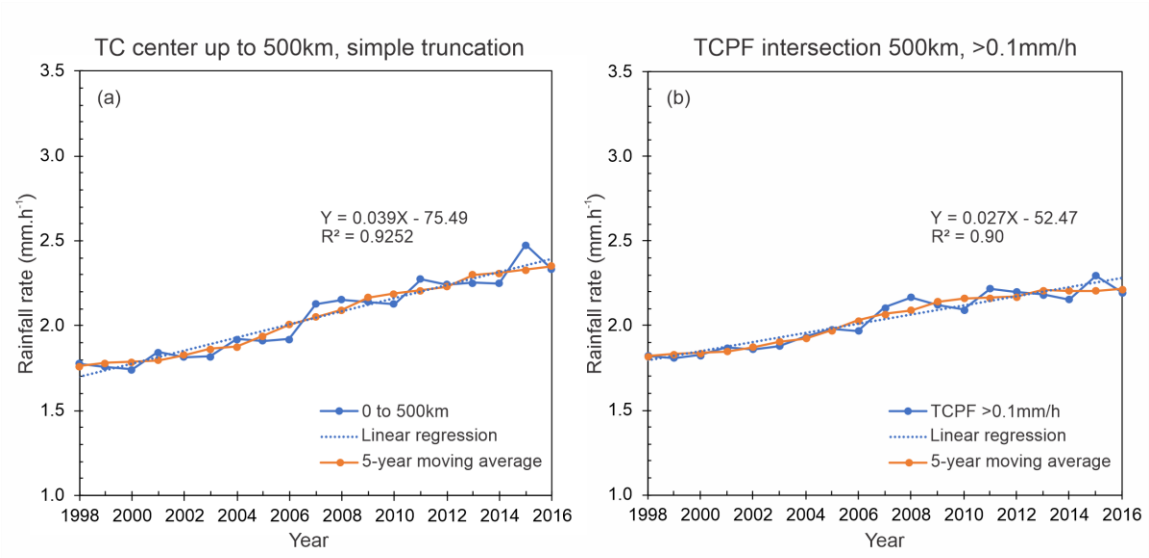

Figure 2-1: Time series and the linear regression fit of TC rain averaged within 0-500km around the storm center for TCs in all global TC-prone basins. (a) Simple truncation method, and (b) Tropical Cyclone Precipitating Feature Method. The linear fitting function and square of the correlation are indicated. The 5-year moving average is also shown.

Global TC rainfall trends are determined using two statistical methods, linear regression fittings, and Mann–Kendall trend tests (see "Data and Methods" section).

Overall, results exhibit an increasing trend in the hourly precipitation rate of 0.027 mm h^{-1} $year^{-1}$, with a coefficient of determination R^2 of 0.90 (Figure 2.1b). This trend can be interpreted as an average percentage of change near +1.3% from one year to the next during the study period (Table 2.3). The result of Kendall's test demonstrates the presence of a trend with 99.9% confidence, with a strong relationship of the TC rainfall rate with respect to ordinal variations of time (Kendall's tau = 0.80). Additional validation of the trend is performed with calculations of Sen's slopes, which ratifies the result of the linear regression and suggests 0.022 and 0.031 mm h^{-1} $year^{-1}$ as the maximum upper and lower bounds of the slope with 95% confidence, respectively (Table 2.4).

Inter-basin comparisons show that this increasing trend is more substantial in the Northwestern Pacific and Northern Atlantic than in other basins, as represented by increased hourly precipitation rates of as much as 0.04 mm h^{-1} $year^{-1}$. Their determination coefficients, Kendall's tau, and statistical significance are also more robust (Figures. 2.2a, 2.2c). Rising trends across the Northern Indian Ocean are centered around 0.03 mm h−1 year−1 (Fig. 2.2d), and trends in the East and Central Pacific are near 0.018 mm h−1 year−1 (Fig. 2.2b). In contrast with the northern hemisphere basins (excepting ECPA), the Southern Pacific and Southern Indian Ocean exhibit a minor trend, as demonstrated by their shallow slopes (Fig. 2.2e, 2.2f) and slightly lower statistical significances. A summary of the main inter-basin statistics is presented in Table 2.5.

Table 2-3: Percentage of change in yearly trends for mean TC rainfall (0-500km TCPF method), TC inner-core rain, and rainband rain in all TC basins. Values in mm.h-1 and percentage

	Total				Inner-core (All categories)				Inner-core (CAT1 to CAT5)				Outer rainband			
Year	Raw	% of change	Regression	% of change	Raw	% of change	Regression	% of change	Raw	% of change	Regression	% of change	Raw	% of change	Regression	% of change
1998	1.82		1.876		4.06		4.426		6.87		7.242		1.55		1.491	
1999	1.81	-0.8%	1.903	1.4%	4.20	3.1%	4.415	-0.2%	7.26	5.4%	7.146	-1.3%	1.54	-0.4%	1.516	1.6%
2000	1.82	0.9%	1.930	1.4%	4.25	1.3%	4.404	-0.2%	6.19	-17.3%	7.050	-1.4%	1.53	-0.8%	1.540	1.6%
2001	1.87	2.5%	1.957	1.4%	4.47	4.9%	4.393	-0.2%	6.27	1.2%	6.954	-1.4%	1.57	3.1%	1.564	1.6%
2002	1.86	-0.6%	1.984	1.4%	4.40	-1.5%	4.382	-0.2%	6.88	9.0%	6.858	-1.4%	1.55	-1.4%	1.589	1.5%
2003	1.88	1.1%	2.012	1.4%	4.56	3.4%	4.372	-0.2%	7.65	10.0%	6.761	-1.4%	1.58	1.5%	1.613	1.5%
2004	1.93	2.8%	2.039	1.3%	4.95	8.1%	4.361	-0.2%	7.25	-5.5%	6.665	-1.4%	1.61	2.0%	1.638	1.5%
2005	1.98	2.3%	2.066	1.3%	4.54	-9.2%	4.350	-0.2%	6.68	-8.5%	6.569	-1.5%	1.64	2.0%	1.662	1.5%
2006	1.97	-0.5%	2.093	1.3%	4.68	3.0%	4.339	-0.2%	6.77	1.2%	6.473	-1.5%	1.68	2.1%	1.686	1.4%
2007	2.11	6.5%	2.120	1.3%	4.60	-1.6%	4.328	-0.2%	6.62	-2.2%	6.377	-1.5%	1.79	6.5%	1.711	1.4%
2008	2.17	2.8%	2.148	1.3%	4.22	-9.1%	4.318	-0.3%	6.12	-8.2%	6.280	-1.5%	1.79	-0.3%	1.735	1.4%
2009	2.12	-2.1%	2.175	1.3%	4.34	2.9%	4.307	-0.3%	6.31	3.0%	6.184	-1.6%	1.77	-1.1%	1.760	1.4%
2010	2.09	-1.5%	2.202	1.2%	4.08	-6.5%	4.296	-0.3%	5.71	-10.5%	6.088	-1.6%	1.81	2.2%	1.784	1.4%
2011	2.22	5.6%	2.229	1.2%	4.08	0.0%	4.285	-0.3%	5.66	-0.9%	5.992	-1.6%	1.86	2.9%	1.808	1.3%
2012	2.20	-0.9%	2.256	1.2%	4.21	3.1%	4.274	-0.3%	5.47	-3.5%	5.896	-1.6%	1.87	0.6%	1.833	1.3%
2013	2.18	-0.7%	2.284	1.2%	4.17	-0.9%	4.264	-0.3%	5.67	3.6%	5.799	-1.7%	1.84	-1.9%	1.857	1.3%
2014	2.15	-1.3%	2.311	1.2%	4.27	2.3%	4.253	-0.3%	5.74	1.2%	5.703	-1.7%	1.84	0.1%	1.882	1.3%
2015	2.29	6.1%	2.338	1.2%	4.30	0.7%	4.242	-0.3%	5.45	-5.4%	5.607	-1.7%	1.95	5.4%	1.906	1.3%
2016	2.20	-4.5%	2.365	1.2%	4.18	-2.9%	4.231	-0.3%	5.47	0.3%	5.511	-1.7%	1.89	-2.9%	1.930	1.3%
Yearly % of change (mean)		1.0%	-	1.3%	-	0.1%	-	-0.2%		-1.5%		-1.5%	-	1.1%	-	1.4%
Total % of change(mean)		20.6%	-	26.1%	-	2.8%	-	-4.4%		-20.4%		-23.9%	-	22.5%	-	29.5%

Table 2-4: Summary of statistics of trends for mean TC inner-core rain, rainband rain, and radius of maximum rainfall in all TC basins.

	Linear regression		Mann-Kendall trend test			Sen's slope		
	Equation	R-squared	Kendall's tau	p-value alpha =0.05	Test interpretation	Sen's slope	Lower bound for 95% confidence	Upper bound for 95% confidence
From 0 to 500 km truncation	y = 0.0386x - 75.459	R^2 = 0.925	0.81	< 0.0001	There is a trend in the series	0.037	0.031	0.043
From 0 to 500 km TCPF method	y = 0.0272x - 52.470	R^2 = 0.903	0.80	< 0.0001	There is a trend in the series	0.027	0.022	0.031
Inner-core global all categories	y = -0.0108x + 26.004	R^2 = 0.066	-0.111	0.534	There is no trend in the series	-0.008	-0.035	0.013
Inner-core global categories 1-5	y = -0.0962x + 199.45	R^2 = 0.629	-0.626	< 0.0001	There is a trend in the series	-0.101	-0.145	-0.058
Rainband region all categories	y = 0.0244x - 47.26	R^2 = 0.9272	0.86	< 0.0001	There is a trend in the series	0.024	0.021	0.029
Rainband region all categories 1-5	y = 0.0250x - 48.268	R^2 = 0.8098	0.673	< 0.0001	There is a trend in the series	0.026	0.018	0.033
RMR global all categories	y = -0.051x + 197.32	R^2 = 0.0041	-0.029	0.890	There is no trend in the series	-0.049	-0.496	0.394
RMR global categories 1-5	y = 0.3756x - 691.09	R^2 = 0.255	0.345	0.041	There is a trend in the series	0.368	0.022	0.805

Table 2-5: Summary of statistics of trends for mean TC rain (0-500 km using TCPF method) in different 6 different TC basins.

	Linear regression		Mann-Kendall trend test			Sen's slope		
	Equation	R-squared	Kendall's tau	p-value alpha =0.05	Test interpretation	Sen's slope	Lower bound for 95% confidence	Upper bound for 95% confidence
North Atlantic	y = 0.0405x - 79.045	R^2 = 0.748	0.67	< 0.0001	There is a trend in the series	0.042	0.027	0.050
E&C Pacific	y = 0.0169x – 32.228	R^2 = 0.454	0.52	0.00011	There is a trend in the series	0.015	0.007	0.029
North West Pacific	y = 0.0370x - 72.072	R^2 = 0.842	0.79	< 0.0001	There is a trend in the series	0.036	0.030	0.042
North Indian Ocean	y = 0.0317x - 61.344	R^2 = 0.513	0.51	0.00186	There is a trend in the series	0.030	0.016	0.051
South Indian Ocean	y = 0.0190x - 36.177	R^2 = 0.592	0.61	0.00011	There is a trend in the series	0.021	0.014	0.027
South Pacific Ocean	y = 0.0177x - 33.615	R^2 = 0.443	0.47	0.00405	There is a trend in the series	0.017	0.006	0.026

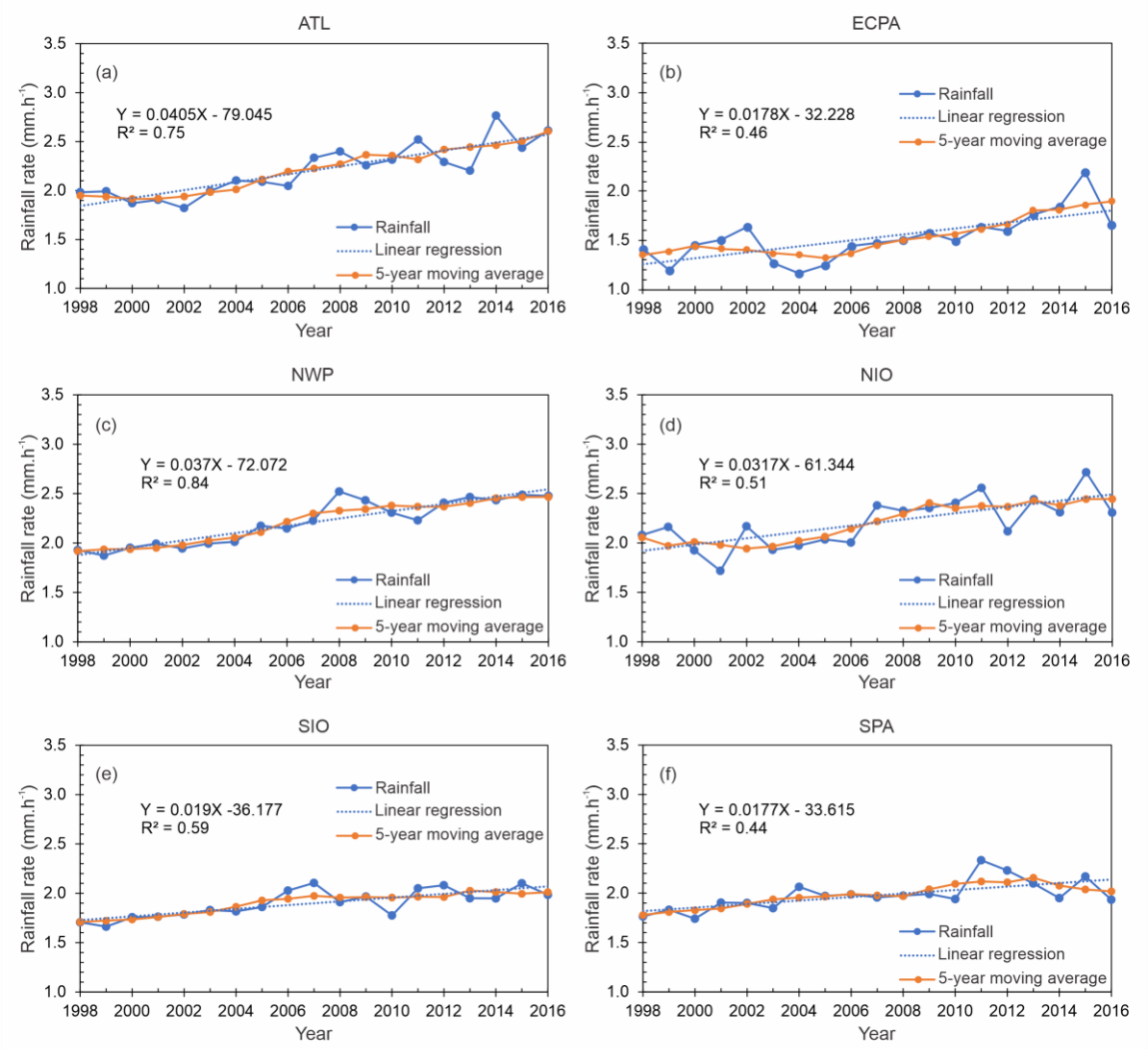

Figure 2-2: Time series and the linear regression fit of TC rain averaged within 0-500km around the storm center for TCs in 6 different basins: (a) Northern Atlantic, (b) East-Central Pacific, (c) Northwestern Pacific, (d) Northern Indian Ocean, (e) Southern Indian Ocean, and (f) southern Pacific. The linear fitting function and square of the correlation are indicated. The 5-year moving average is also shown.

With reference to the TC intensities, Figure 2.3 and Table 2.6 summarize the trends and their significance level at a global scale. Since the denomination of intensity categories varies depending on the regional ocean basins where TCs form, in this study, we define tropical depression (TD) as a system with wind speed from 5 to 33 knots, tropical storms (TS) as systems with wind between 34 and 63 knots, and the hurricane categories 1–5 (CAT1, CAT2, CAT3, CAT4, and CAT5) are adopted from the Saffir-Simpson scale. In all the categories, there is a consistent increase in the range of 0.015–0.043 mm h^{-1} $year^{-1}$. The most pronounced increases occur in the extremes of the storm category scale (TD, TS, CAT4, and CAT5) with a slightly more pronounced effect in the CAT4 and CAT5 hurricanes with slopes of 0.03 and 0.04 mm h^{-1} $year^{-1}$, respectively (Figure 2.3a, b, f, g). Intermediate storm categories show smaller increases (Figure 2.3c, 2.3d, 2.3e), specially CAT2 hurricanes with a slope of only 0.015 mm h^{-1} $year^{-1}$.

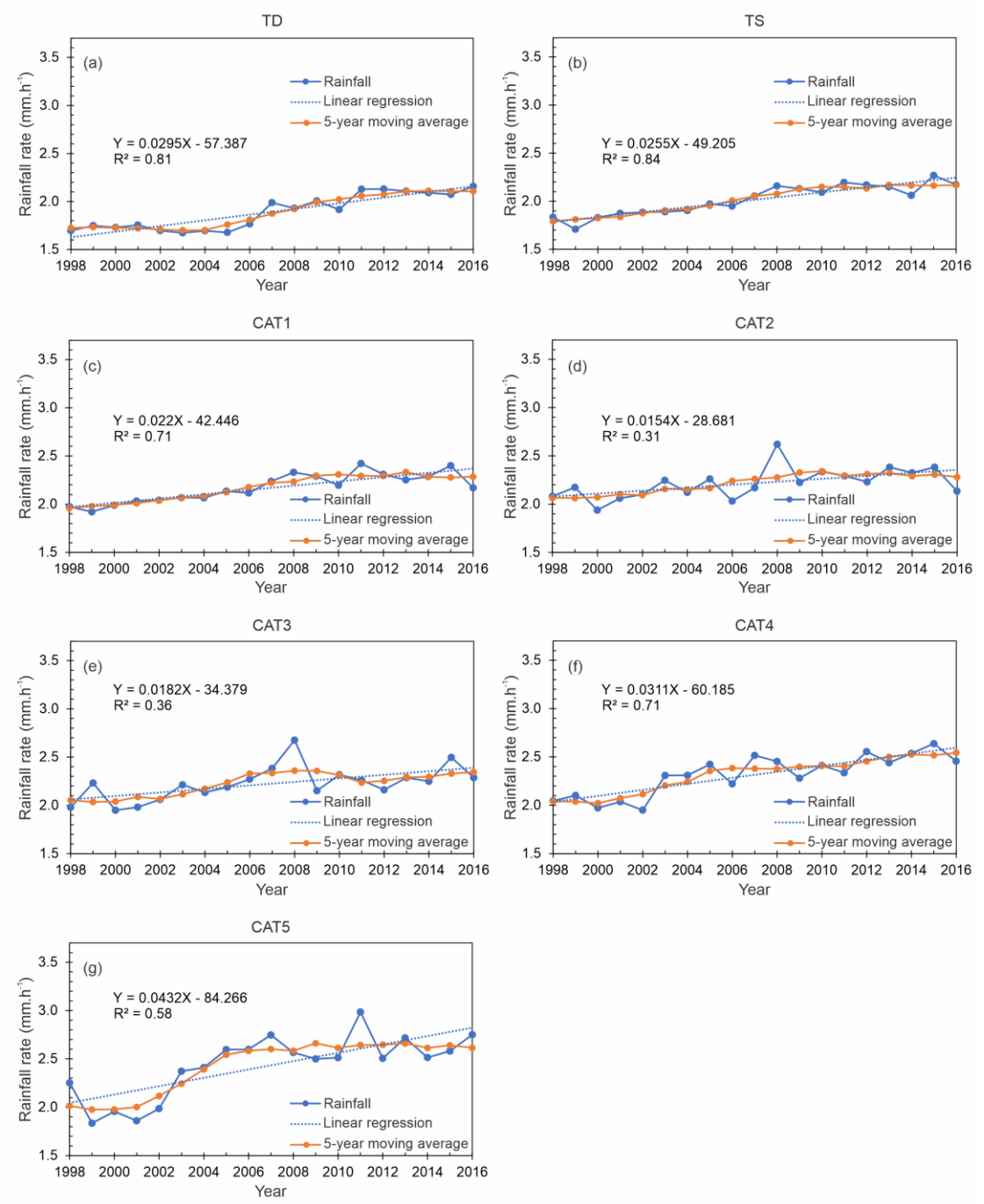

Figure 2-3: Time series and the linear regression fit of TC rain averaged within 0-500km around the storm center for different TC intensity categories: (a)TD, (b)TS, (c) CAT1, (d) CAT2, (e) CAT3, (f)CAT4, and (g) CAT5.

Table 2-6: Summary of statistics of trends for mean TC rain (0-500 km using TCPF method) in different 7 different TC intensity categories.

	Linear regression		Mann-Kendall trend test			Sen's slope		
	Equation	R-squared	Kendall's tau	p-value alpha =0.05	Test interpretation	Sen's slope	Lower bound for 95% confidence	Upper bound for 95% confidence
Tropical depression	y = 0.0295x - 57.387	R^2 = 0.808	0.60	0.00016	There is a trend in the series	0.028	0.020	0.036
Tropical storm	y = 0.0255x - 49.205	R^2 = 0.845	0.79	< 0.0001	There is a trend in the series	0.026	0.019	0.032
Category 1	y = 0.0222x - 42.446	R^2 = 0.712	0.68	< 0.0001	There is a trend in the series	0.024	0.018	0.030
Category 2	y = 0.0154x - 28.681	R^2 = 0.307	0.47	0.00405	There is a trend in the series	0.015	0.007	0.026
Category 3	y = 0.0182x - 34.379	R^2 = 0.336	0.48	0.00315	There is a trend in the series	0.019	0.006	0.031
Category 4	y = 0.0311x - 60.185	R^2 = 0.705	0.63	< 0.0001	There is a trend in the series	0.031	0.020	0.043
Category 5	y = 0.0432x - 84.266	R^2 = 0.575	0.58	0.00031	There is a trend in the series	0.040	0.016	0.062

2.3 Differentiated trends: inner-core vs. rainbands

In the case of the inner-core region, we used a storm-dependent method that uses the radius of maximum azimuthal rain rate (RMR) as the size determining factor. A sensitive test comparing a simple truncation of 100 km, RMR, 1.5×RMR, and 2×RMR was performed to describe the effects of varying the selection distances in estimating averaged inner-core rainfall rates (Figure. 2.4).

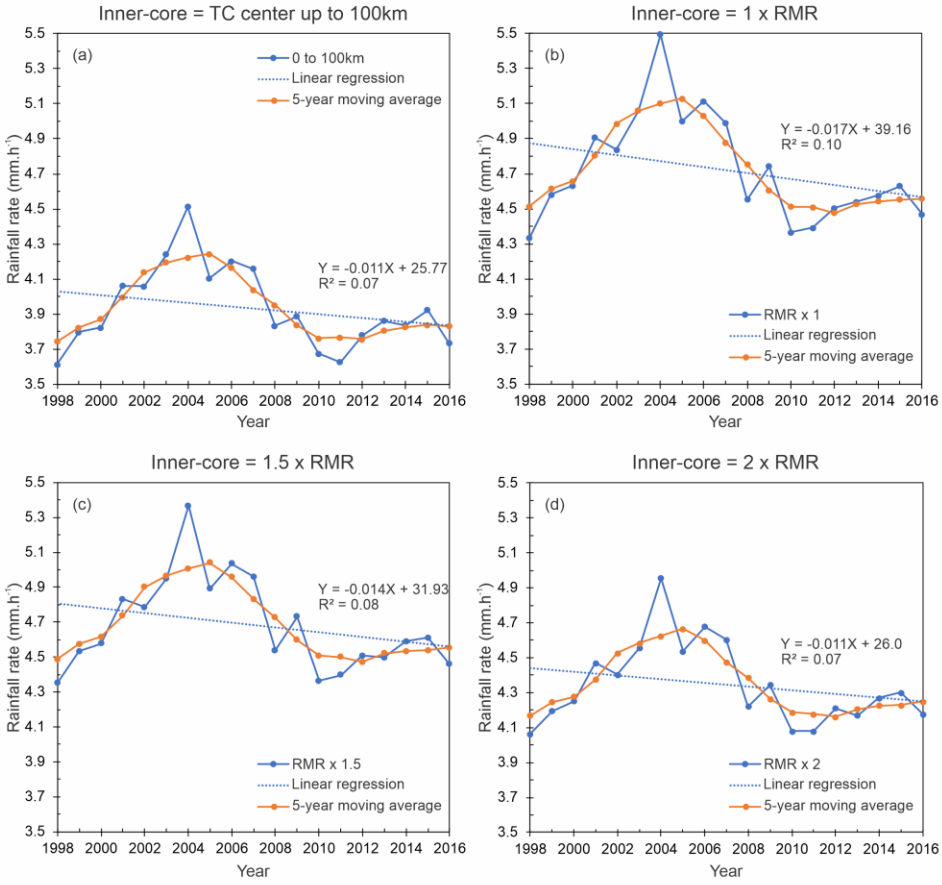

Figure 2-4: Time series and the linear regression fit of TC rain averaged within the inner-core for TCs in all global TC-prone basins. Figure shows a sensitivity test between different methods to define the inner-core extent from the TC center as a function of the radius of maximum rainfall. (a) From 0 to 100 km, (b) within 1x RMR, (c) within 1.5 x RMR, and (d) within 2 x RMR. The linear fitting function and square of the correlation R are indicated. The 5-year moving average is also shown.

Results indicate that the slopes of averaged rainfall rates slightly decrease as a longer radius is used to define the inner core region. However, in all the inner-core definitions, the nearly same result is obtained. Therefore, we adopted a distance threshold of 2*RMR to ensure the full inclusion of the most developed cumulus nimbus, area of high winds, intense vertical motions, and the eye, as suggested by Shea and Gray (1973). Finally, for the rainband region, we used the area from 2×RMR until the external borders defined by the TCPF method that includes precipitation features with centroids within 500 km from the TC center; this selection was made as an approximation to allow the inclusion of rainfall rates in the area beyond two times the radius of maximum wind and the outermost part of the storm.

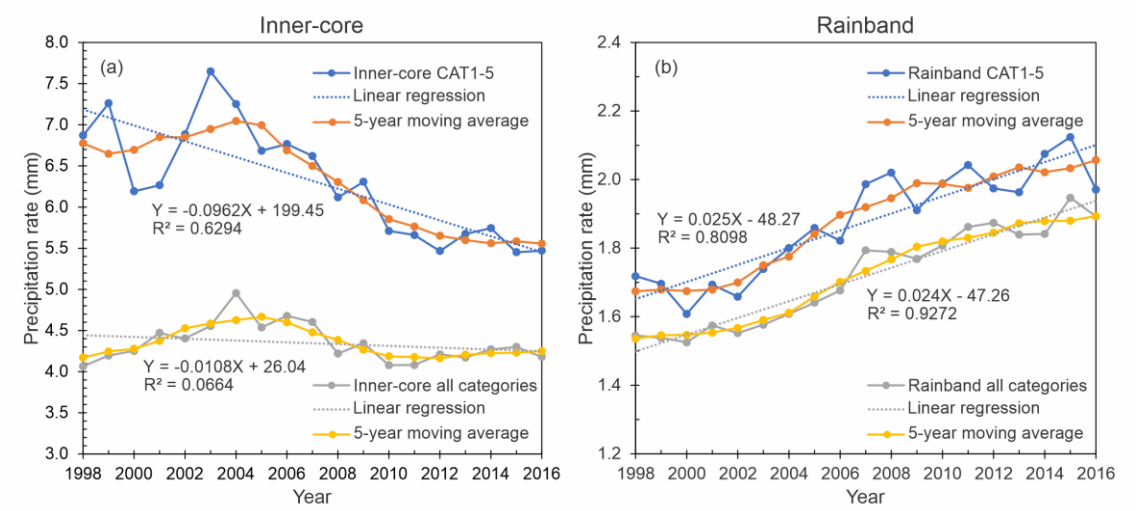

Figure 2-5: Time series and the linear regression fit of averaged rain for different TC regions: (a) mean TC inner-core rain, and (b) mean TC rainband rain in all global TC-prone basins. Plots are showing averages for all intensity categories and for hurricanes from CAT1-CAT5. The linear fitting function and square of the correlation are indicated. The 5-year moving average is also shown.

In the inner-core and rainband regions, results indicate that, while the rainfall rate in the inner-core decreases, the rainfall rate in the rainband region increases (Figure 2.5a,

2.5b). This inverse relationship is present in all intensity categories; however, in the inner-core region, the Kendall test shows that it is only statistically significant for storms from CAT1 to CAT5 (Table 2.4). In both storm regions, linear regressions reach high R-squared values, particularly for the rainband where the trend is more homogenous. In a more detailed analysis, both time series seem to follow differentiated slopes for the periods before and after 2003–2004, suggesting a potential inflection point (or peak in the inner core) that could be associated with decadal or multi-decadal cycles.

2.4 Discussion and conclusions

In this study, an increasing trend in the TC rainfall rate during the period 1998– 016 has been identified on a global scale. On average, an increase of 0.027 mm h^{-1} $year^{-1}$ is observed in the time series. This trend is nearly equivalent to a percentage of change of +1.3% from one year to the next. The increase is controlled by the reduction of the averaged inner-core rainfall in a range between −0.011 and −0.096 mm h^{-1} $year^{-1}$ (percentage of change near to −1.5%/year, for CAT1 to CAT5) along with an increase in the averaged rainband rainfall rate of 0.035 mm h^{-1} $year^{-1}$ (percentage of change near to +1.4%/year). Despite the fact that the inner-core region produces the most intense rainfall rates (Figure 2.6a, 2.6b), the extent of the rainband region is much larger than the inner-core, which leads to a more significant contribution from the rainbands to the total TC rain (Figure 2.6c, 2.6d). These differences in the proportional contribution and the rising trend in the rainbands suggest that the global increase must be mainly a consequence of special conditions favoring rainfall production in the rainband environment.

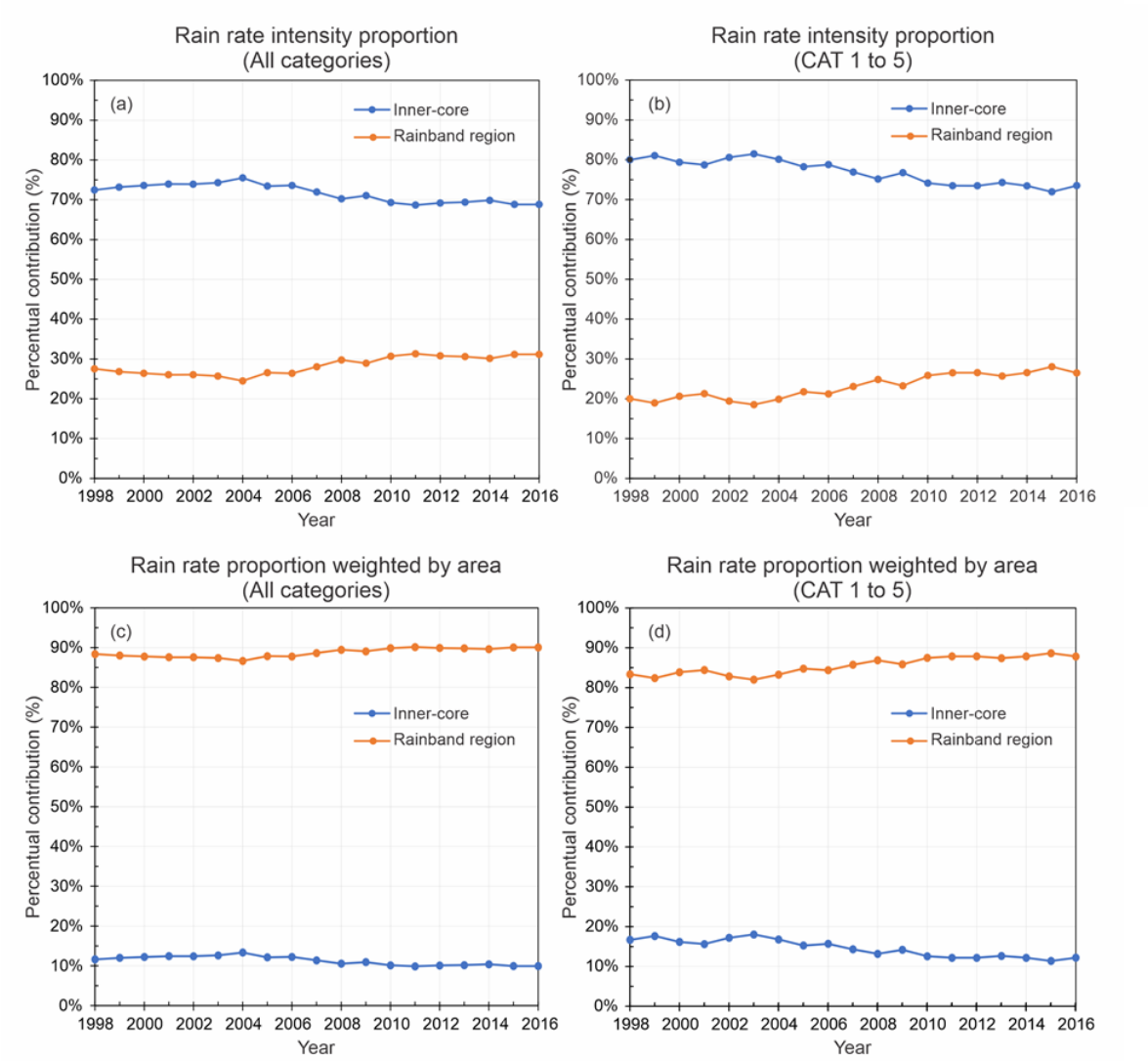

Figure 2-6: Time series showing the approximated global rainfall contributions of the inner-core and the rainband region. (a) rain rate intensity proportion for all storm categories, (b) rain rate intensity proportion for only storms from category 1 to 5, c) rain rate proportion weighted by area for storm categories, and d) rain rate proportion weighted by area for storm from category 1 to 5. Values presented as percentage.

We hypothesize that the increasing global trend is associated with higher availability of water vapor triggered by warmer sea surface temperatures under constant relative humidity conditions, as suggested by the calculations of Knutson et al. (2020) using the Clausius–Clapeyron equation, as well as the projections of tropospheric water vapor in

the IPCC report (2013). To check this hypothesis, we analyzed the Reynolds Sea surface temperature (SST) (Reynolds et al. 2007) and the total precipitable water (TPW) at t = 0 from the Global Forecasting System (GFS) analysis in the region from 0 to 500 kilometers, both variables as reported in the Statistical Hurricane Intensity Prediction Scheme (SHIPS) developmental database (DeMaria and Kaplan 1994, 1999; DeMaria et al. 2005; Schumacher 2013). Results confirm that at least in the northern hemisphere (NH), the environment has been warming and moistening during the study period (Fig. 2.7a, 2.7c), which seems to favor the precipitation rates in the rainband region. Besides, linear regressions of both SST and TPW exhibit robust statistical significance and confirmation of a rising trend from the results of the Kendall test (Table 2.7). We also found positive correlations between precipitation rate and SST with a correlation coefficient of 0.22, and between precipitation rate and TPW with a correlation coefficient of 0.50.

In contrast to the northern hemisphere findings, our results over the southern hemisphere basins show no significant trend in the SST and TPW values (Supplementary Table 5). This situation is explained by the smaller slope of the sea surface temperature when compared to the northern hemisphere average (Fig. 2.7a, 2.7b). Here, although the linear regression of sea surface temperature shows a slight decreasing slope, the Kendall test indicates this trend approaches zero (Table 2.7). A similar situation occurs with the availability of total precipitable water (Fig. 2.7c, 2.7d); while the northern hemisphere is increasing, the trend in SPA remains stable (Table 2.7). Figure 2.7d exhibits a slightly negative slope, but the Kendall test indicates it is still approaching zero from the statistical perspective. The combined results of the sea surface temperature and total precipitable water are consistent with our observational findings on the occurrence of differential

rainfall rate increases between both hemispheres, which suggest slightly less pronounced effects of the warming projections in the increase in rainfall rates along the southern hemisphere. This is consistent with the climate modeling results summarized by Knutson et al. (2020).

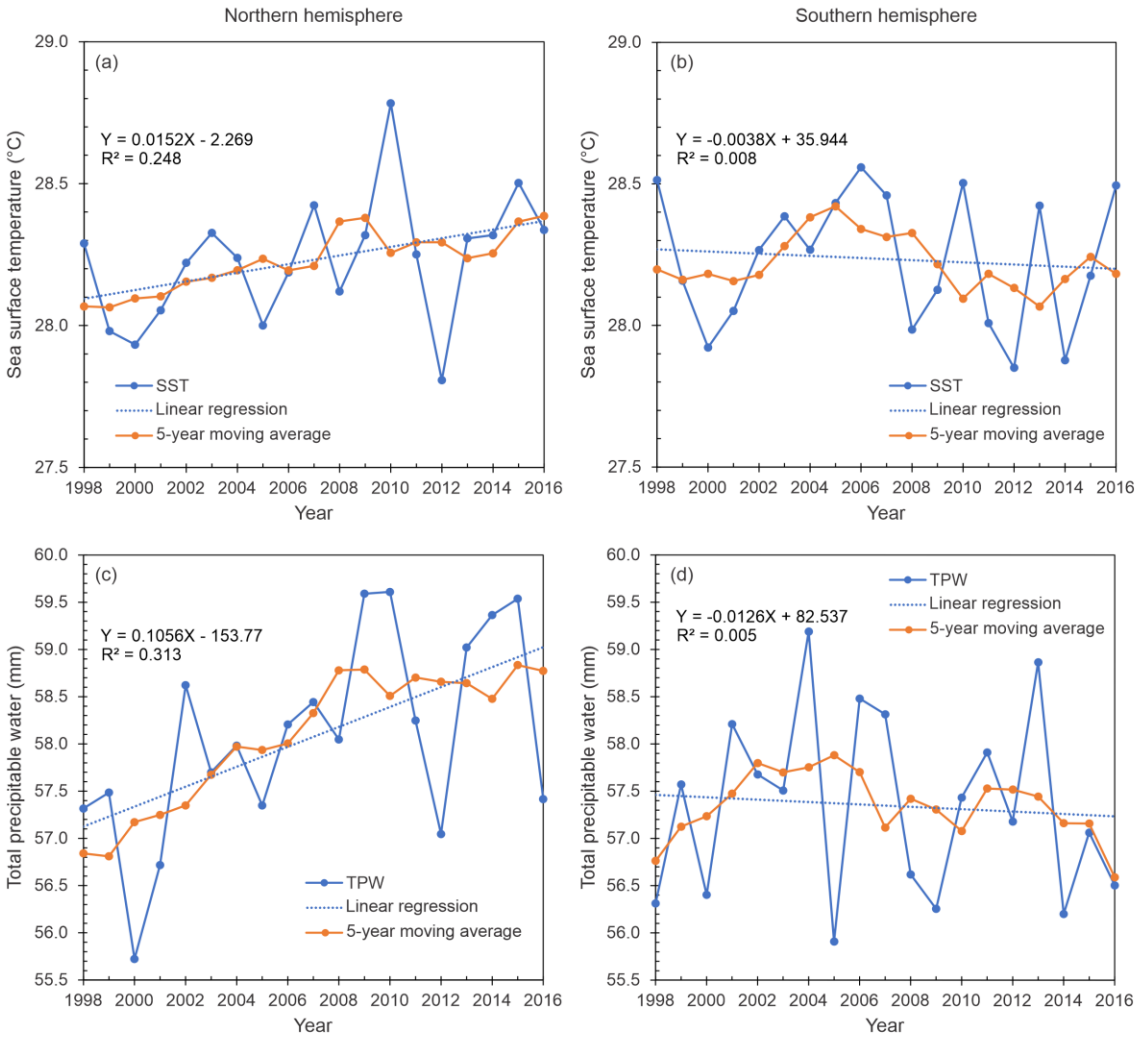

Figure 2-7: Time series and the linear regression fit of TC environmental parameters from 0 to 500km: (a) Sea surface temperature in the northern hemisphere, (b) Sea surface temperature in the southern hemisphere, (c) Total precipitable water in the northern hemisphere, and (d) Total precipitable water from in the southern hemisphere. The linear fitting function and square of the correlation are indicated. The 5-year moving average is also shown.

Table 2-7: Summary of trend analyses of seas surface temperature, total precipitable water, and radius of maximum wind speed. Values comparing northern and southern hemispheres.

	Linear regression		Mann-Kendall trend test			Sen's slope		
	Equation	R-squared	Kendall's tau	p-value alpha =0.05	Test interpretation	Sen's slope	Lower bound for 95% confidence	Upper bound for 95% confidence
SST (NH)	y = 0.0152x - 2.2692	R^2 = 0.2487	0.258	0.029	There is a trend in the series	0.016	0.002	0.032
SST (SH)	y = -0.0038x + 35.944	R^2 = 0.0083	-0.029	0.890	There is no trend in the series	-0.001	-0.027	0.019
TPW (NH)	y = 0.1056x - 153.77	R^2 = 0.3129	0.415	0.013	There is a trend in the series	0.124	0.036	0.193
TPW (SH)	y = -0.0126x + 82.537	R^2 = 0.0053	-0.076	0.679	There is no trend in the series	-0.014	-0.119	0.065
VMAX (NH)	y = -0.1202x + 290.04	R^2 = 0.0736	-0.111	0.534	There is no trend in the series	-0.077	-0.370	0.146
VMAX (SH)	y = 0.1755x - 304.70	R^2 = 0.0448	0.006	0.990	There is no trend in the series	0.006	-0.232	0.439

As a potential and desired alternative explanation, we also explored the change of maximum sustained wind speed during the analysis period (Table 2.7). However, statistical results show that storm intensities remain unchanged; therefore, we concluded that the increasing global trend must be the result of higher SST and TPW only. In other words, the scheme that assumes that the magnitude of rainfall is totally dependent on storm intensity is less than perfect because of the influence of environmental conditions.

We found that the results of Kim et al. (2021) may partially support our findings. Their study suggests that the strength of inner-core rainfall strength is strongly correlated with TC intensity, but weakly correlated with large-scale environmental conditions, while the TC total rainfall area showed a stronger correlation with environmental conditions than with TC intensity. The total TC raining area is closely related to the rainband environment. In other words, TC rainfall outside the core is more sensitive to environmental conditions than that inside the core, which may explain the finding that only rainfall in the rainband increased with increasing SST and TPW.

This study uses a method that employs the radius of maximum azimuthal rain rate (RMR) to define the inner-core region. Traditionally, the radius of maximum wind (RMW) has been a more conventional parameter to do so. However, RMW data is not available for all global TCs analyzed in this research, driving us to adopt the RMR as a proxy of RMW. Considering that one of our observational results indicates that the inner-core rainfall rate is decreasing, further analysis of the RMR was performed. We found that globally and when considering all the TC categories, the RMR does not observe any particular trend (Figure. 2.8a–2.8c). However, in CAT1 to CAT5 storms, results show that the RMR

slightly expands outwards (Figure 2.8d–2.8f) with lower R^2 and confidence levels than other reported trends (Table 2.4).

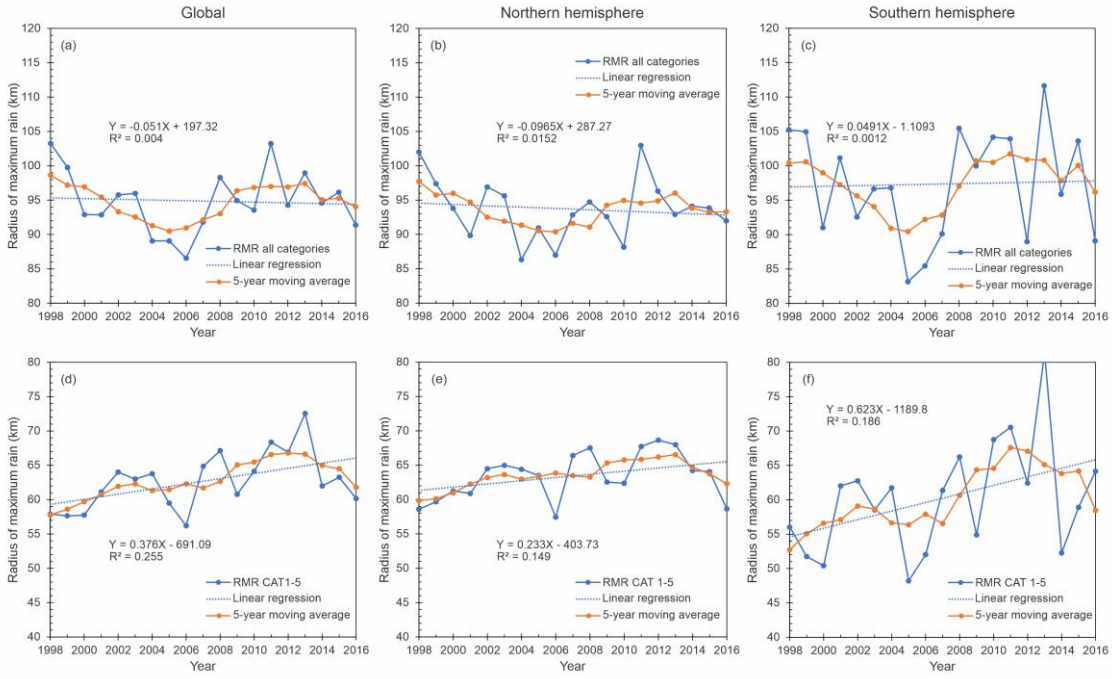

Figure 2-8: Time series and the linear regression fit of TC rain averaged within 0-500km around the storm center for (a) radius of maximum rain globally, (b) radius of maximum rain in the northern hemisphere, and (c) radius of maximum rain in the southern hemisphere, (d) radius of maximum rain globally for categories 1-5, (e) radius of maximum rain in the northern hemisphere for categories 1-5, and (f) radius of maximum rain in the southern hemisphere for categories 1-5.

Overall, our observational results coincide with the modeling approaches that suggest increasing trends in TCs rainfall rates with warmer sea surface temperatures (Lin et al. 2015; Knutson et al 2013; Villarini et al. 2014; Scocciomarro et al. 20147). However, the differences in the order of magnitude between the expected (modeled) vs. observed rainfall rates in our period of study are substantial; while modeling averages projects a +14% for a 2 °C warming increase (Knutson 2020), our result for the 19-year time series is close to +21% for a variation of 0.21 °C only (with more presence in the northern hemisphere). We consider this difference is explained by the domaining influence of the

increasing rainfall rates in the rainband region, which is mainly attributed to the more availability of precipitable water in the atmosphere.

In addition to the difference mentioned above, we found that rainfall rates at the inner-core level decrease for CAT1 to CAT5 hurricanes, which contradicts the results of modeling projections that suggest potential increases within 100 km of the TC center (Knutson 2020). However, this finding is actually similar to the results of a recent observational study by Kim (2020), which suggested that the inner core rainfall rate decreases by 0.081 mm h−1 per year (his Fig. 3.1.6). Kim (2020) used the same TRMM 3B42 data, but the analysis period was different and tropical depressions were excluded. The definition of inner-core rainfall was also different from this study. He used a fixed 100 km radius from the TC center to define inner-core rainfall. So far, we do not have a good explanation why the rain rate in the inner-core has a decreasing trend. This would be a direction for future studies.

An additional potential contradiction with our results is the findings of Lau and Zhou (2012). They reported differences in the sign and magnitude of total TC lifetime accumulate rain trends between ATL (+23% per decade), ECPA (−25.1% per decade), and NWP (−20.9% per decade), which seemingly agrees with our findings in ATL but amply differed for ECPA and NWP. However, as mentioned in the introduction, Lau and Zhou (2012) used the GPCP data, which is a 5-day mean rainfall dataset from satellite and rain gauge measurements with a spatial resolution of 2.5° latitude X 2.5° longitude. With such a low temporal resolution, it was impossible to estimate realistic rain rate intensity in TCs. They recognized that the total TC lifetime accumulate rain measure they used was rather

an integral measure of total rain energy associated with a TC. Therefore, their results are not comparable with our study here.

The above analyses lead us to conclude that the increasing rainfall rate induced by warmer and moister environments has the potential to generate more severe impacts associated with TC rainfall events across TC-prone areas, particularly in the Northwestern Pacific and Northern Atlantic basins where the increasing trends are more pronounced.

3. CLIMATOLOGY OF TROPICAL CYCLONE RAINFALL MAGNITUDE AT DIFFERENT LANDFALLING STAGES.

3.1 Abstract

Estimating the magnitude of tropical cyclone (TC) rainfall at different landfalling states is an important aspect of the TC forecast that directly affects the level of response from emergency managers. In this study, a climatology of the TC rainfall magnitude prior, during, and after landfall is presented at a global scale. A total of 1850 TCs in the period from 2000 until 2019 are analyzed using satellite information to characterize the magnitude and axial-symmetric properties of TCs as they approach and interact with the land surface. We found that during the travel over open waters up to nearly 400 km away from the coast, TCs experience a precipitation enhancement as it gets closer to the coast. Then, in the geographic region from 0 to 400 km from the coast, TCs initially experience a slight enhancement in the precipitation production, followed by a decay in the rainfall rate proportional to the gradual increases of the TC rainfall area over the land. Finally, once the TCs make landfall, we found a nearly perfect inversely proportional relation between rainfall intensity reduction and the increase in TC rainfall area. Volumetric rainfalls are also analyzed over the entire TC extent and the portion over land during the post-landfall stages. We found that when a TC with life maximum intensity of a major hurricane makes landfall as tropical depression or tropical storm, it usually produces the largest spatial extent and volumetric rain. However, this result only applies when quantified the TC rainfall over land, isolated from the ocean.

3.2 Introduction

When tropical cyclones (TCs) approach the coastline and make landfall, severe weather conditions can cause serious damage to coastal communities. The torrential precipitation produced by the storms poses one of the most dangerous threats to human life and infrastructure due to its potential to trigger inland freshwater flooding and mudslides (Willoughby, 2012; Rapport, 2014). Therefore, a better understanding of the precipitation patterns at different landfalling stages is an extremely important input for emergency responders in catastrophes mitigation. A fundamental step in this effort is predicting specific areas within the TC structure that will develop the heaviest rainfall rates and their magnitude variations before, during, and after landfall events.

Several studies have examined the climatological features of tropical cyclone precipitation (TCP) and the factors that shape its intensity and geographic distribution over oceans and continents. For example, Jiang and Zipser (2010) calculated the contribution of TCP to the total precipitation balance over all the TC-prone basins, finding that TCs accounts for 4-11% of the precipitation over the tropics but can account for as much as 50% in large regions over the open ocean. In a similar way, but focused on the continental part only, Prat and Nelson (2016) evaluated the TCP contribution over the land from 1998-2012, showing that an average of 3.5% of the total numbers of rainy days are caused by cyclonic activity, and TCP-related days represent over 13% and 31% of extreme events, but can account for more than 70% of extreme rainfall over higher-latitude areas, usually occurring after the peak of the cyclonic activity on each global basin.

Some other specific basin-focused studies have reported the influence of TCP at local scales. For example, Bregy et al. (2020) characterized the total contribution over the

eastern United States during the TC season, finding maxima on the Lousiana, North Carolina, and Texas coast, decreasing farther inland at rates of approximately 6.2–6.7 mm km−1; in their findings, they also report TCP is more closely linked to variations in the position of North Atlantic Subtropical High than to the ENSO index. In the northwest Pacific, especially for those TCs making landfall over China (including Taiwan and Hainan islands), Ren et al. (2006) found that TCs significantly contribute to annual rainfall in the southern east coastal region, accounting for 20-40% of the total annual balance. Similarly, Zhan et al. (2017) showed an increasing trend of TCP based on the assessment of flooding and extreme precipitation events, with a more substantial influence on the Guandong province, where more than 60% of the largest ten hazardous floods in the northern and eastern parts have been attributed to TCP. In the Philippines, TC contribution to annual rainfall ranges from 6% in the southern regions to 54% over the northern regions (Bagtasa 2017). Over the South Pacific basin, continental Australia receives a contribution of between 30 and 70%, making it one of the regions of the globe where this fraction reaches the highest values (Dare et al., 2012). Finally, over the Indian ocean, Uddin et al. (2019) found that TCP contributes for about 8% of the total overland rainfall during 1998-2016 with a maximum occurrence during October-December (16-18%) with more frequent occurrence in the Bay of Bengal.

In terms of the internal distribution of TCP, previous studies found that TCs over the ocean have a precipitation maximum in the front quadrants, either the left or the right forward half depending on the moving speed (Burpee and Black, 1989; Rodgers et al., 1994). More recently, modeling results obtained by Kimbal (2008) found that maximum rainfall occurring on the right side of the storm before landfall shifts to the left of the storm

track during landfall (as the TC interacts with the coast); the author explains this variation in terms of the differential intrusion of dry air between the left and right sides of the storm using idealized landfalling modeling hurricanes. As TC makes landfall, interaction with land surface causes the wind and precipitation fields to decrease (Kapplan and DeMaria, 1995), but the extent of the rainfall does not necessarily follow the same trend nor the same decreasing pace because of the complexity of the forcing factors that might drive rainfall distribution at landfall (Matyas 2010).

Internal TC rainfall distribution has also been analyzed under the influence of vertical wind shear (e.g., Corbosiero & Molinari, 2002; Lonfat et al., 2004; Cecil, 2007; Wingo & Cecil, 2010). In most of these investigations, the rainfall variations are quantified as low wavenumber asymmetries using the Fourier decompositions over shear-relative rainfall distributions. The larger the asymmetry, the more variability in the internal spatial distribution may be explained (Yu et al., 2015). These studies coincide with the same conclusion: TCs over the ocean show downshear to downshear-left maximum in the wavenumber-1 asymmetry field. Besides, over the land, Xu et al. (2014) and Yu et al. (2015, 2017) confirmed that this wind shear effect is still dominant even at different landfalling stages. Xu et al. (2014) also suggest that the magnitude of the rainfall asymmetry increases with the wind shear magnitude but decreases with the increasing TC rainfall intensity, and the wind shear effect is less efficient for TCs in environments of relatively low values of sea surface temperature (SST) and total precipitable water (TPW).

With reference to the TCP size, Kimbal (2008) found that after landfall, the increasing friction results in broadened areas of accumulated precipitation with decreasing rain rates. This finding is consistent with observational studies analyzing TCP overland

(Ren et al. 2006; Zhan et al. 2017, Bregy et al. 2020). In particular, Touma et al. (2019) refined previous investigations using the concept of life maximum intensity (LMI), stating that the highest median intensity and the largest median spatial extent over land occur when major hurricanes have weakened to tropical storms, resulting in greater flood risk despite the weaker wind speeds. However, Touma's findings partially contradict previous investigations on the rainfall intensity assessment. For instance, using satellite precipitation retrievals, Jiang et al. (2008) found that the total volumetric rain decreases after landfall. So further research about the characteristics of the precipitation intensity and the volumetric rainfall for TCs is a must to clarify the reason for this contradiction.

Although the studies mentioned above characterize key features of TCP, there are few observational studies about its variation before, during, and after landfall on a global scale. In this paper, we explore the axial variations, distribution, and evolution of rainfall during the landfalling process of TC through a statistical approach that uses a homogeneous long-term time series of TRMM satellite data. In addition, an emphasis on the post-landfall stage is presented by analyzing the TC life maximum intensity (LMI) and the total volumetric rain, with the aim to investigate further the contradictions of previous studies about the behavior of the precipitation intensity on landfalling TCs, by taking advantage of the benefits of the spatial and temporal characteristics of the satellite data.

3.3 Data and Methods

3.3.1 Data

The analysis period spans from June 2000 to December 2019, covering all the TC-prone global basins. A total of 1850 TCs are analyzed with a sample distribution of 315 in

the North Atlantic basin (ATL), 363 in Central and East Pacific (ECPA), 572 in Northwest Pacific, 114 in North Indian Ocean (NIO), and 167 in Southern Pacific (SPA), respectively (Table 3.1). Rainfall information is obtained from NASA Integrated Multi-satellitE Retrievals for the Global Precipitation Measurement (GPM) mission (IMERG) product version 6 (Huffman et al. 2019, 2020). IMERG combines multi-satellite passive microwave (PMW) precipitation estimates, microwave-calibrated IR rain estimates, and rain gauge measurements into a homogeneous, high-quality retrieval. This study uses the final run version of IMERG with a spatial resolution of 0.1° x 0.1° (nearly 10km x 10 km) with a 3-hourly resolution to match the best track information. Table 3.1 shows the number of IMERG files grouped by TC intensities and basin; each file was converted to a GIS-readable format and cataloged using a relational geodatabase for easier interaction with other geographics datasets. TC attributes such as center coordinates, time, and maximum wind speed are obtained from the International Best Track Archive for Climate Stewardship (IBTrACS version 4, Knapp et al. 2018) in both point and line vector topologies. Considering the differences in the reported values from the independent national services, particularly over the Pacific basins, a meticulous verification is performed to favor the information from the US National Hurricane Center (NHC) and the Navy's Joint Typhoon Warning Center (JTWC). TC events beyond 35°N or 35°S were removed and only records with high-quality attributes in columns 8, 14, and 17 of the IBTrACS are utilized in the final geographic database.

Table 3-1: Number of best track records with IMERG retrieved rainfall for TCs during 2000-2019 in different TC intensity categories and different TC-prone basins.

Category/Basin	ATL	ECPA	NWP	NIO	SIO	SPA	Total
Tropical Depression	2,694	4,365	7,135	1,742	5,614	2,255	23,805
Tropical Storm	6,050	7,169	9,357	1,862	6,388	2,791	33,617
Category 1	1,624	1,846	3,613	331	1651	791	9,856
Category 2	673	837	2,033	104	822	399	4,868
Category 3	611	768	1611	113	853	361	4,317
Category 4	515	531	1796	103	581	276	3,802
Category 5	126	53	542	21	68	66	876
Total	12,293	15,569	26,087	4,276	15,977	6,939	81,141

Environmental conditions around the storms are obtained from the Statistical Hurricane Intensity Prediction Scheme (SHIPS, Last updated: April 2020) developmental dataset, which includes 6-hour retrievals of observational and derived data over various annular regions calculated from the TC center (DeMaria and Kaplan 1994, 1999; DeMaria et al. 2005; Schumacher et al. 2013). In this study, we selected four SHIPS environmental parameters to be examined at each landfall stage: Reynolds Sea surface temperature (RSST), wind shear with vortex removed and averaged from 0-500km (SHDC), wind shear heading averaged from 0-500km (SHDD), and total precipitable water between 0 to 500 km. Only the values at the initial time (t=0) are employed in our analyses.

3.3.2 Definitions of stages relative to landfall

Previous studies of rainfall distributions in landfalling TCs classified stages relative to landfall in different ways. Jiang et al. (2008) grouped Tropical Rainfall Measuring Mission (TRMM) 3B42 overpasses into ocean, mixed, and land groups using the percent coverage of raining area over land or ocean. For each 3B42 snapshot within a 5° radius of the TC center, if greater than 60% of the raining area was over the ocean (land), this overpass was

attributed to ocean (land) group. If 40-60% of the raining area is over land/ocean, this overpass was grouped as mixed. Xu et al. (2014) defined three landfalling stages of TRMM 3B42 overpasses based on the TC center's proximity to the coast. If the TC center was 400 to 700km, 0 to 300/400km, and -200 to 0 km from the coast, this overpass was defined as off-shore, pre-land, and aft-land, respectively. Yu et al. (2017) described three stages associated with before, during, and after landfall based on the observation time of 3B42 relative to the TC center's landfall time, with stage I, II, and III defined as 24 h prior to, at the time of, and after the TC center's landfall. Table 3.2 summarizes the classifications in these three studies.

Table 3-2: Classifications of various stages before, during, and after TC landfall in Jiang et al. (2008), Xu et al. (2014), Yu et al. (2017), and this study.

	Jiang et al. (2008)	Xu et al. (2014)	Yu et al. (2017)	This Study	
Before Landfall	**Ocean:** TC raining area >60% over ocean	**Off-shore:** TC center 400~700km away from coast	**Stage I**: 24 h prior to landfall	**Before Landfall:**	**Ocean:** TC center >700km away from coast
					Off-shore: TC center 400~700km away from coast
During Landfall	**Mixed:** TC raining area 40~60% over land	**Pre-land:** TC center 0~300/400km away from coast	**Stage II**: at the time of landfall	**During Landfall (Pre-land):** TC center 0~400km away from the coast	**Pre-land I:** TC raining area <50% over land
					Pre-land II: TC raining area ≥50% over land
After Landfall	**Land:** TC raining area >60% over land	**After-land:** TC center -200~0km away from coast	**Stage III**: 24 h after landfall	**After Landfall (After-land):** TC center is over land	**After-land I:** TC raining area <50% over land
					After-land II: TC raining area ≥50% & <100% over land
					After-land III: TC raining area 100% over land

Note that the classifications in the last two studies only considered the TC center's landfall, while the first study only considered the raining area's landfall. A good classification method should consider both. Yu et al. (2017)'s definition is based on the period before or after the TC center's landfall, which depends not only on how far the observation is close to the coast or inland but also on the storm translation speed. Therefore, in this research, we adopted both Jiang et al. (2008) and Xu et al. (2014)'s approaches. As shown in Table 3.2, we classified into three main categories, including before, during, and after landfall, respectively. The Before-landfall category is further divided into two subcategories: Ocean is for TCs with centers greater than 700 km away from the coast, and Off-shore is for TCs with their centers 400 to 700 km away from the coast. The During-landfall (Pre-land) category is defined as TCs with their centers 0 to 400 km away from the coast. This category is further divided into two subcategories: Pre-land I and Pre-land II, based on how many percentages of the TC raining area are over land. The After-landfall (Aft-land) category is defined as TCs with their centers over land. This category is further divided into three subcategories: After-land I, After-land II, and After-land III, based on how many percentages of the TC raining area are over land.

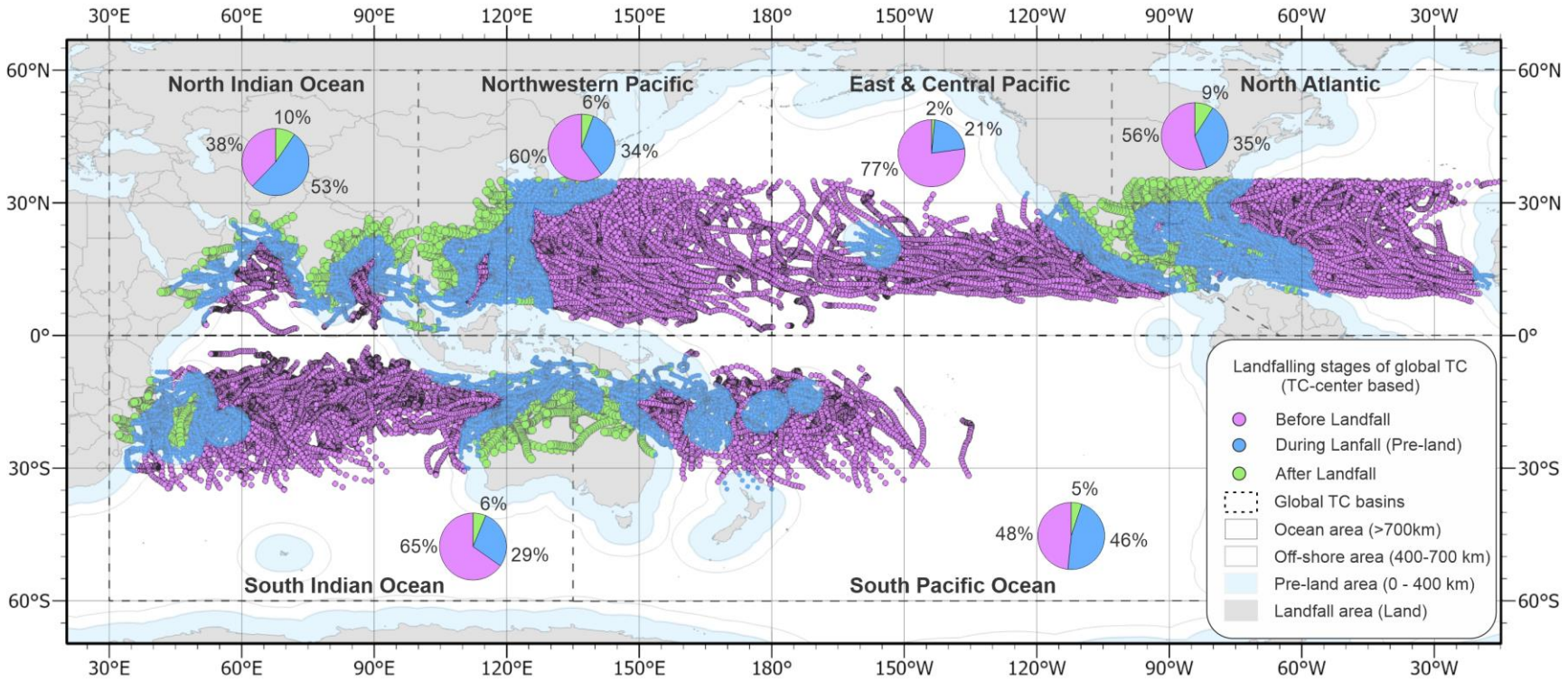

Figure 3-1: Locations of TC centers for all best track records as a function of the three main landfalling stages. Magenta color represents TC centers before landfall, blue color during landfall, and green color after landfall. Pie charts show the percentual contribution of each landfall stage per global basin. Regions corresponding to each category as the distance from the shoreline are also shown. Land surfaces with areas less than 1,400 km2 are not considered

With these definitions, a geospatial classification of the best track record was performed to obtain the TC samples for each landfall stage. As a first step, each TC center is assigned to a geographic region representing before, during, and after, as shown in Figure 3.1. Several minimum island sizes were tested during the buffer operation to obtain consistent areas for each category across all the TC-prone global basins. This procedure was particularly sensitive for the North Atlantic and South Pacific basins due to the presence of large chains of islands. A final threshold of 1.400 square kilometers was employed to remove minor islands. Figure 3.1 shows a map with the classification of best track records and the percentual distribution of each basin. It can be noticed that globally the majority of the TC positions fall into the Before Landfall category (48% – 77%), followed by During Landfall (21% - 53%), and ending with After Landfall records (2% - 10%). In addition, each basin exhibits unique features. For instance, ECPA is less prone to landfalling events; in contrast, ATL, NWP, and NIO exhibit the highest susceptibility. Table 3.3 shows the same best track records as Figure 3.1 but normalizing by named storms. Under the above considerations, global TCs have a fraction of landfall near 38%. As the second step, each Tropical Cyclone Precipitation Feature (TCPF, please see the details below in Section 2c) is determined. Its areal portion over both land and ocean is calculated to refine at the subcategory level within each landfall stage. Table 3.4 summarizes the final sample size obtained for each category across global basins.

Table 3-3: Number of TCs and landfalling TCs (in parentheses) categorized by season and basin during the period 2000 - 2019.

Season/Basin	ATL	ECPA	NWP	NIO	SIO	SPA	Total
2000	18(5)	19(2)	31(12)	4(3)	N/A	N/A	72(22)
2001	16(7)	17(1)	33(17)	5(2)	16(5)	8(2)	95(34)
2002	14(8)	16(2)	31(12)	5(3)	17(5)	9(4)	92(34)
2003	21(8)	16(5)	27(14)	4(3)	19(7)	11(2)	98(39)
2004	15(7)	16(2)	32(14)	6(2)	18(8)	7(3)	94(36)

2005	29(15)	16()	25(15)	7(3)	19(3)	8(2)	104(38)
2006	9(2)	21(2)	26(16)	7(5)	16(5)	8(2)	87(32)
2007	14(9)	15(2)	27(12)	6(5)	14(7)	10(1)	86(36)
2008	16(10)	18(4)	27(13)	7(7)	20(6)	9(2)	97(42)
2009	9(2)	20(3)	28(13)	5(4)	18(5)	10(2)	90(29)
2010	21(8)	12(3)	19(11)	5(4)	15(5)	10(4)	82(35)
2011	18(5)	13(3)	27(12)	6(3)	13(6)	9(3)	86(32)
2012	18(6)	17(1)	27(12)	4(3)	17(6)	4(0)	87(28)
2013	14(5)	18(4)	33(18)	7(7)	16(3)	8(1)	96(38)
2014	9(2)	21(2)	23(13)	5(2)	15(5)	11(6)	84(30)
2015	11(3)	22(4)	28(13)	4(2)	18(6)	9(2)	92(30)
2016	16(9)	21(3)	30(14)	5(2)	9(1)	11(3)	92(32)
2017	18(10)	20(5)	33(23)	5(3)	11(4)	8(3)	95(48)
2018	14(4)	25(5)	35(21)	9(9)	13(6)	8(2)	104(47)
2019	15(4)	20(3)	30(15)	8(4)	19(4)	9(4)	101(34)
Total	315(129)	363(56)	572(290)	114(76)	303(97)	167(48)	1834(696)
TC landfall fraction	41%	15%	51%	67%	32%	29%	38%

Note: Fraction of landfall TCs calculated as TC center over land. Only land surfaces greater than 1,400 km^2 are considered. Values for southern hemisphere basins during 2000 are not available.

.

Table 3-4: Number of selected satellite overpasses of IMERG records over TC centers in different landfall stages.

Landfall Stage	Subcategory	ATL	ECPA	NWP	NIO	SIO	SPA	Total
Before Landfall (TC center over open ocean)	Ocean (>700km)	5,659	8,814	121,30	287	8,237	1,519	36,646
	Off-shore (400-700km)	1,189	3,196	3,544	1,329	2,184	1,841	13,283
During Landfall* (0-400km)	Pre-Land I <50% over land	4,129	3,229	8,608	2,125	4,460	3,060	25,611
	Pre-Land II ≥50% over land	204	89	309	126	99	165	992
After Landfall* (center over land)	After Land I <50% over land	356	174	666	86	332	109	1723
	After Land II ≥50% & <95% over land	661	67	780	302	574	216	2600
	After Land III >95% over land	95	0	50	21	91	29	286
Total		12,293	15,569	26,087	4,276	15,977	6,939	81,141

3.3.3 Precipitation features and axisymmetric decompositions

As a prerequisite to calculating TC rain-associated parameters, a definition of the TC rainfall area must be adopted. Therefore, we define the TC raining area using the concept of Tropical Cyclone Precipitation Feature (TCPF) suggested by Jiang et al. (2010). Under the TCPF framework, a precipitation cell (precipitation feature) is delineated by contiguous grouping pixels that comply with a selection criterion. In this study, only IMERG pixels with a rain rate greater than 0.1 mm/hour are chosen to be part of each precipitation cell, zero values and non-data values are excluded from the calculations. Furthermore, to be qualified as TCPF, the distance between the TC center and the geometric center of each valid cell must be less than 500 km. A geodatabase with raster and vector versions of the TCPF at each IMERG observation time was created to subsequently allow the match with the best track and SHIPS databases through predesigned foreign keys within a relational database model.

The axisymmetric decomposition is performed by determining the azimuthal mean rainfall rate in 100 steps of 10-km wide annuli from the storm center outward to the 1,000 km. Only pixels belonging to TCPF are considered in calculating the averages to avoid contamination from neighboring non-TC precipitation features. Since 10-km is about the IMERG spatial resolution, the algorithm only includes pixels when more than half of its size is within the annulus. Finally, the 2D composites of rainfall rate distribution rotated relative vertical wind shear (the SHDD parameter from SHIPS) are calculated for different TC landfall stages as a function of the storm translation speed and environmental variables. The shear directions of Southern Hemisphere overpasses are flipped around the motion direction to be consistent with the Northern Hemisphere frame of reference and to account for the Coriolis effect, as explained in Chen et al. (2006). We stratified the motion seed into two categories as suggested by Pei and Jiang (2008): Low motions

speed (0 <5 m/s) and fast motion speed (≥5 m/s). In the case of the wind shear magnitude, it was stratified into two categories: low shear (0–5 m/s) and high shear (>5 m/s). TPW was also divided into two categories: low TPW (0–60 mm) and high TPW (>60 mm), and finally, the sea surface temperature was also stratified into two categories (by following Cecil, 2007): Low SST(<28°C) and high SST (≥28°C). Results of this classification for before, during, and after the landfall stages are presented in discussion section.

3.3.4 Area and volumetric rain analysis over landfalling TCs

For those TCs with tracks that at some point during their lifetime fall in the post-landfall categories (i.e., After Land I, After Land II, and After Land III), we identified the individual lifetime maximum intensity (LMI) by looking at the maximum sustained wind speed and categorizing this value into an abbreviated intensity scale that consists of 4 categories: TD for tropical depression, TS for tropical storms, CAT12 for minor hurricanes, and CAT35 for major hurricanes. In this way, each TC track snapshot can be categorized by combining its point intensity(current) and the LMI. For instance, TD/CAT35 indicates that the storm intensity at the current satellite observation position is a tropical depression (TD) and that storm at some moment during its lifetime reached major hurricane intensity (CAT35). Thus, there are ten possible point intensity-LMI combinations TD/TD, TD/TS, TD/CAT12, TD/CAT35, TS/TS, TS/CAT12, TS/CAT35, CAT12/CAT12, CAT12/CAT35, and CAT35/CAT35.

As a second step, the central tendency of each satellite overpass containing the TC rain was investigated to find the most robust typical value. Arithmetic mean and median were calculated and compared at the overpass level (mean/median of rain pixels) and the point intensity-LMI level (Mean/Median of typical values at the category of interest). However, because of the homogeneity

of the gridded rain field provided by satellite retrievals, in a vast majority of the cases, median and mean values are very close, indicating little skewness of the rain samples used in the calculations. In the current research, typical values correspond to the averages from the raining pixels obtained from the TCPF method, i.e., values greater than 0.1mm/hour in the IMERG file.

The last step calculates the volumetric rain over the total TC area and over the effective land portion (rain pixels over land only). Although both averages are reported, this procedure was performed to facilitate an objective comparison with studies working with rainfall over land and provide a more realistic estimation of the rainfall magnitude that affects human activities inland. In calculating rain over land, a raster map of 0.1° x 0.1° containing the continental and island polygons was employed to distinguish between land and ocean pixels by looking for a perfect match with the spatial resolution of the satellite IMERG rain data. Finally, the total volumetric rain of each overpass is calculated by multiplying the average TC rain by the TC area.

3.4 Results and discussion

3.4.1 Tropical cyclone precipitation before landfall

During the TC travel over the open ocean, TCP experience a homogeneous growth mainly controlled by TC wind intensity and environmental conditions. As shown in figure 3.2, for the two before landfall categories (Ocean and Off-shore), there is a steady increase in the averaged TCP as the storm approaches the land, this behavior is consistent with the traditional strengthening trend of TC characteristics when TCs move freely over the ocean with full access to surface fluxes of latent heat that favor its intensification. From the axisymmetric standpoint, figure 3.3 shows that globally, TC radial distribution is well defined and nearly follows the classic wind patterns reported in the TC literature (e.g., Holland, 1980; Holland et al., 2010). About the inter-basin

differences, Figure 3.4 shows the axisymmetric patterns for each global basin. It can be noticed that, in general, the TCP intensity decreases as the TC approaches the land, except in the NWP and ECPA basins where Ocean profiles are slightly higher than Off-shore, particularly at the inner core level.

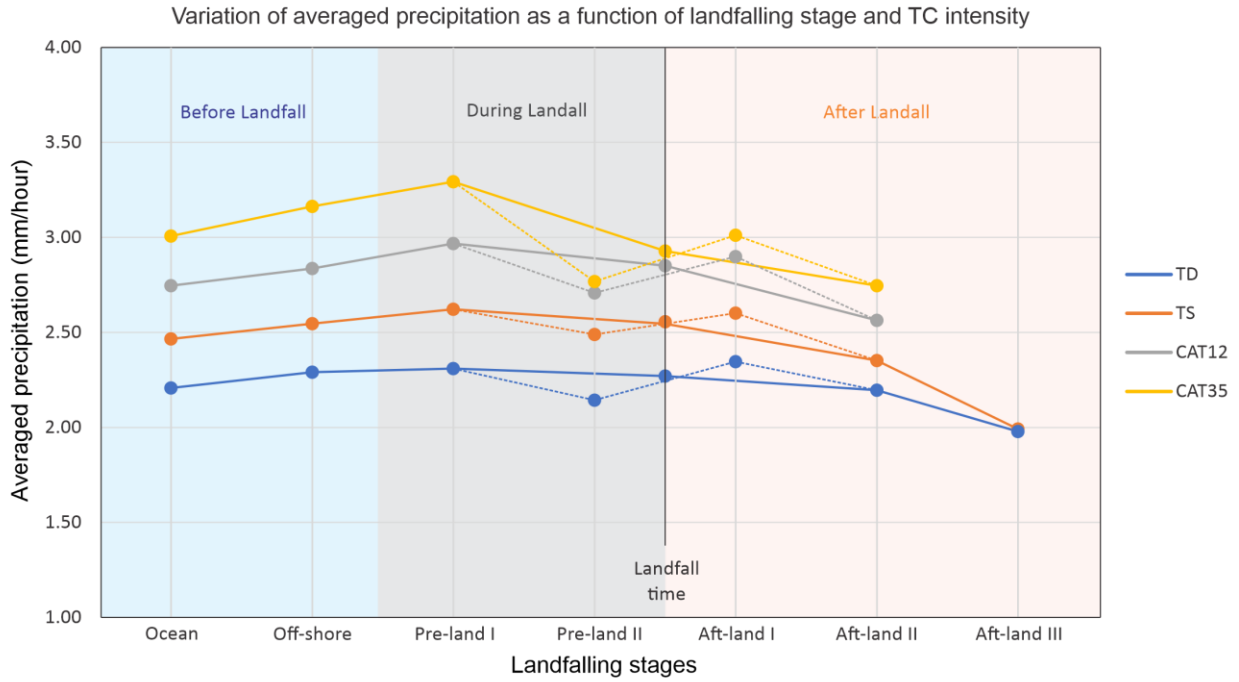

Figure 3-2: Lifecycle of the mean tropical cyclone precipitation intensity (rain rate) as a function of the landfall stage for different storm intensities. Continuous lines represent the approximated chronological order. Dotted lines in the landfall region show the averages for Pre-land-II and After-land-I as influenced by the percentage of TCP area over land and the ocean in each category.

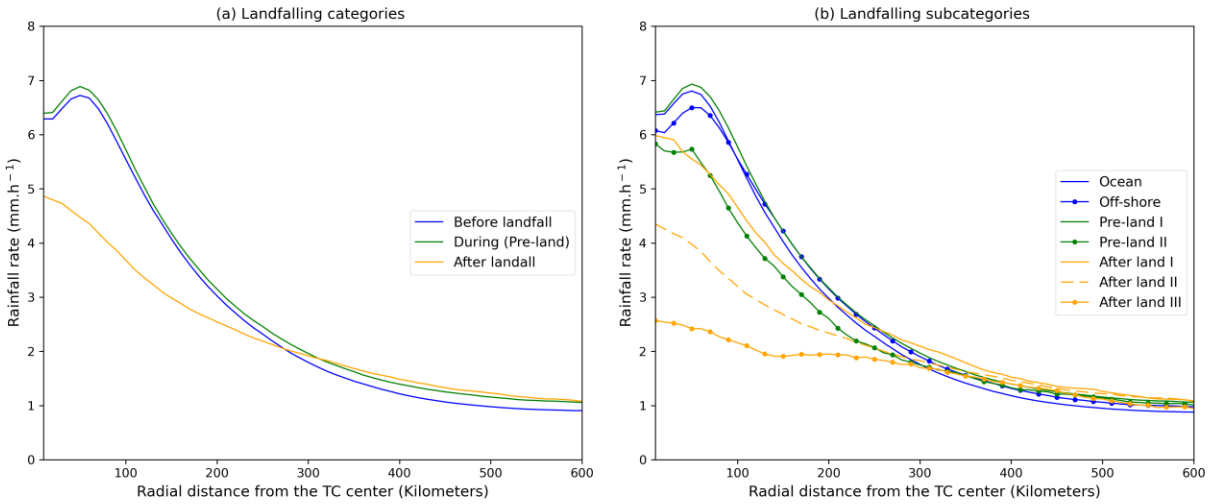

Figure 3-3: Radial distribution on azimuthally averaged rainfall rate categorized by landfalling stages (a) Division as the distance from the land before, during, and after; (b) Subdivision of landfalling stages combining distance from the land and percentage of the raining area over land/ocean.

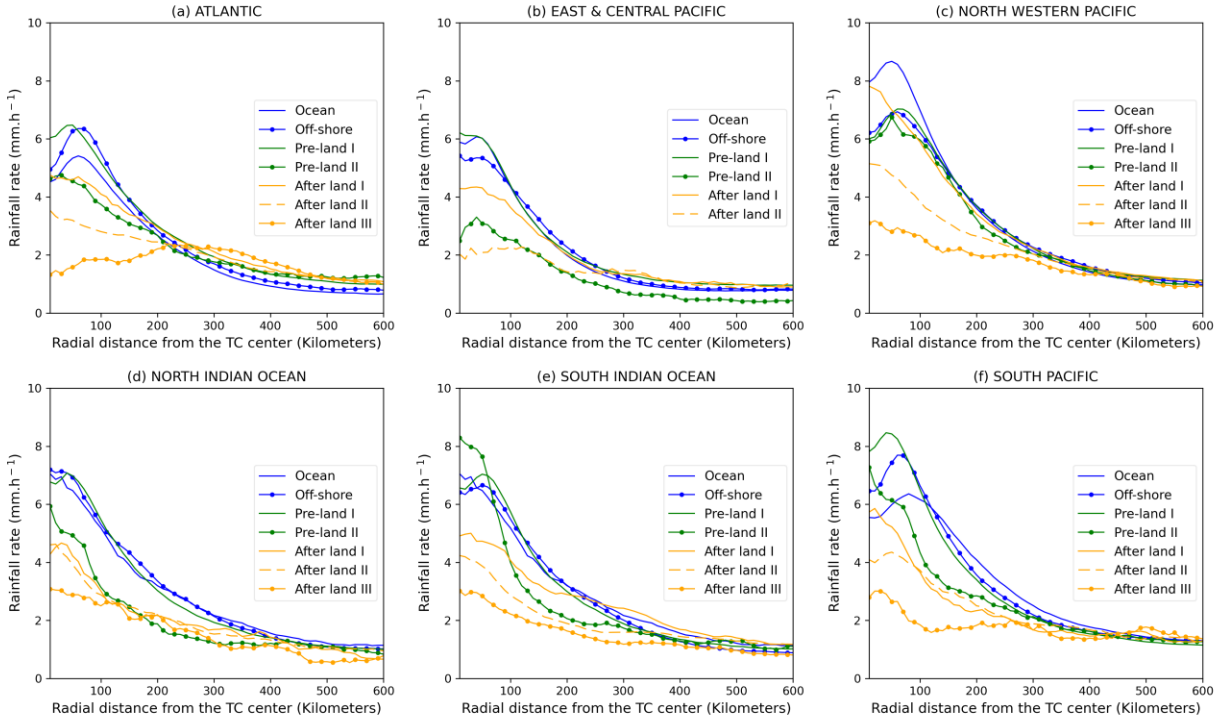

Figure 3-4: Radial distribution of azimuthally averaged rainfall rate for different landfall stages in (a) ATL, (b) ECPA, (c)NWP, (d). NIO, (e) SIO, and (f) SPA basins.

3.4.2 Tropical cyclone precipitation before landfall

In the case of the two during landfall categories, we found opposite trends (figure 3.2). For the first part, when at least half of the TCP area remains over the ocean (Pre-land-I), the average precipitation continues its increasing trend at a nearly similar pace than in the Before landfall stages. In contrast, once the TCP area exceeds 50% over land (Pre-land-II), there is a notable decrease in the precipitation production caused by the abrupt change in the surface predominance from water to land. Across the during-landfall stages, the azimuthally averaged profiles of figure 3.3 still show an axisymmetric structure. However, in the Pre-land-II stage, eye patterns in TCs begin to disappear at the inner-core level.

Concerning the inter-basin differences, each basin exhibits a different level of separation between the axisymmetric profiles of both During-landfalling stages (figure 3.4), perhaps because of specific geographic conditions. Interestingly, TCs in NWP observe little differences between both curves, which suggest a higher resilience to TCP weakening as they evolve across Pre-land-I and Pre-land II landfall stages. We hypothesize that this difference might be caused by more prominent topographic features along the coastal regions than other basins with flatter lands.

3.4.3 Tropical cyclone precipitation after landfall

After landfall stages show an initial increment in the averaged TCP for those storms with up to 50% of their TCP area over the ocean, followed by a rapid decrease as the TCP area moves inland. Interestingly, TC in the Pre-land-II and After-land-I categories exhibit similar profiles in most of the panels in figures 3.3 and 3.4 with minor variations. This situation is explained by the irregular shape of TCP areas, resulting in similarities between storms with TC centers overland

with most of their TCP area over the ocean and storms with TC centers over the ocean with their TCP area mostly over the land. In other words, Pre-land-II and After-land-I are not necessarily in strict chronological order because the TC center as reported in the Best Track does not coincide with the geometric center of each TCPF due to the complex coexisting factors that affect the shape of the precipitating area at landfall. About After-landfall-II and After-landfall-III, there is a noticeable decrease in the average rainfall intensity as the storm moves into the land (figure 3.2).

Regarding the radial distribution by basins, NWP shows the maximum rate o reduction in the After-landfall categories, though its final After-landfall intensity reaches a similar level to other global basins. An interesting feature in the global comparison is that ATL storms exhibit an enhancement in the region near 300km, combined with a more drastic reduction in the inner-core area.

3.4.4 TC Volumetric rain for after landfall stages

Considering after-landfall stages are the most influential to human activities, a more detailed look at rainfall production is presented for such portion of the TCP lifecycle. Figure 3.5 shows the variation of the TC average rainfall rates, rain area, and volumetric rain as a function of intensity. Fig. 3.5a and 3.5b describe the variation for the full extent of the average TCPF over both land and ocean. It can be noticed that in all the cases, the mean rate, rain area, and volumetric rain decrease systematically with the weakening of the TC intensity after landfall. However, when the portion over the ocean is removed (as shown in the procedure of figure 3.6), the observed trend of the TCP area increases as the storm moves inland and the TC intensity weakens. Regarding the volumetric rain, figure 3.5d shows the global average as a function of the TC intensity. Interestingly, it can be noticed that despite the reduction in the rain rate, the net amount of rain remains slightly increasing,

having its maximum values for CAT1 and TS events, and then decreasing until the storm disappears.

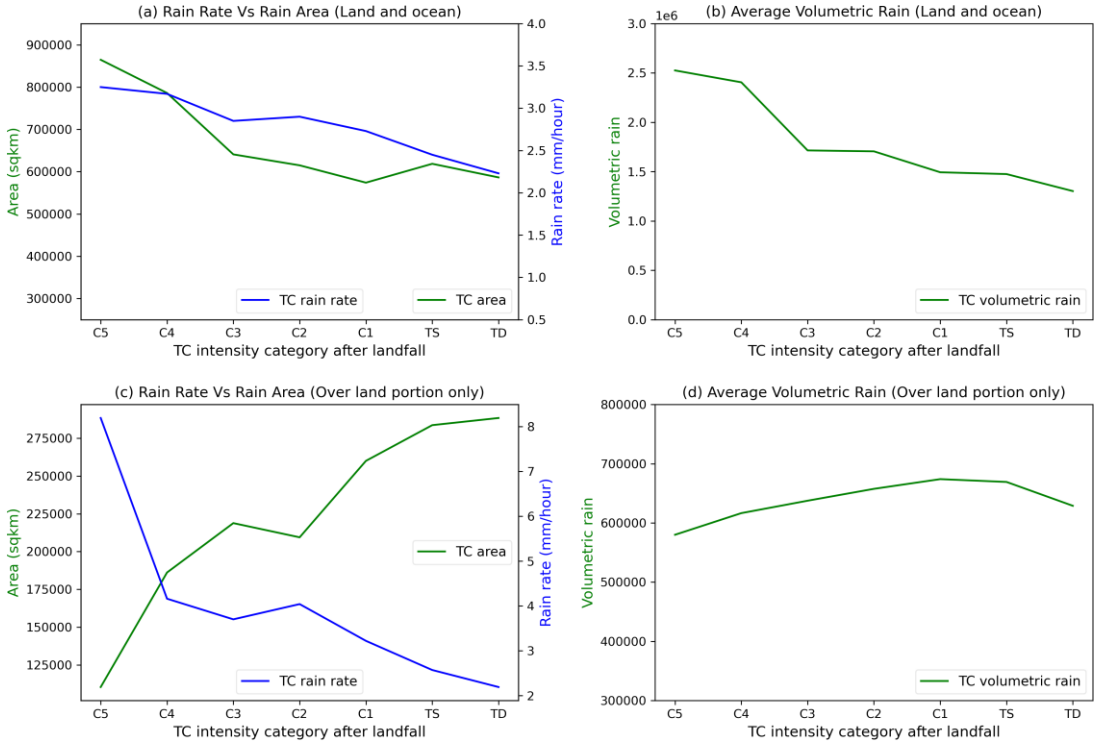

Figure 3-5: Global variations of tropical cyclone rain rates, area, and volumetric rain for after-landfall stages. Panels (a) and (b) represent the variation considering the total TC extent in the calculations. Panels (c) and (d) represent the calculations by only considering the TC extent over the land portion.

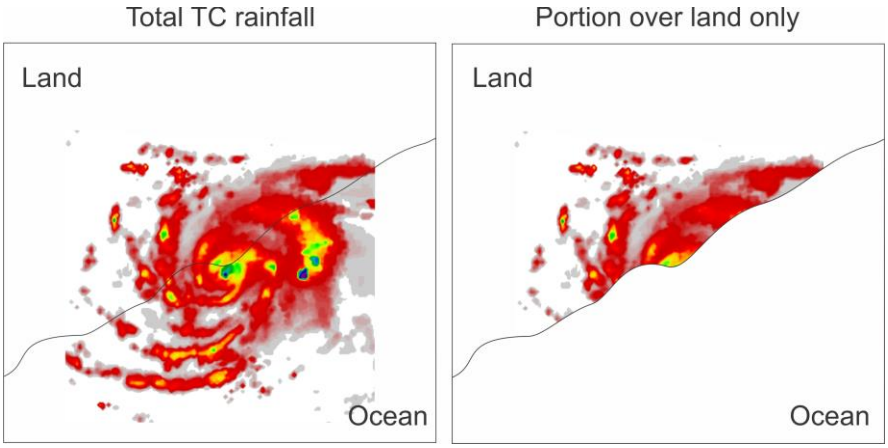

Figure 3-6: Differentiation between tropical cyclone precipitation for After-landfall stages: (a) calculation over the total storm area, and (b) calculation over the land portion only.

Based on the above results, calculations of combinations of the point (current) intensity vs. maximum lifetime intensity (LMI) were performed for the volumetric rain calculations over three different areas of influence: 1) Total TCP area, 2) the portion of the TCP that lies over the land, and 3) the portion of the TCP area that affects the continental United States (CONUS). Concerning the volumetric rain over the entire TCP area, Table 3.5 shows that when combining the contributions between both sections (ocean and land), it is difficult to establish a well-defined pattern in the global averages or the inter-basin differences. This situation is explained by the trade-off effect between TCP area and TCP intensity in calculating volumetric rain. The lower the categories, the higher the areas, and the higher the intensities, the higher the averaged TCP (Figure 3.5c).

Table 3-5: Averaged tropical cyclone volumetric rain and number of samples (in parentheses) for each point-LMI category in global basins. Values are calculated over the entire TC area (including over ocean and land) when the storm best tract center was over land (after-landfall stages).

Point Intensity/ LMI	ATL	ECPA	NWP	SIO	SPA	Global
TD/TD	1,046,000(27)	1,491,261(15)	1,412,329(66)	2,127,014(15)	821,065(21)	1,328,139(146)
TD/TS	864,406(326)	789,884(37)	1,609,431(268)	1,651,243(217)	2,103,962(122)	1,369,986(1105)
TD/CAT12	999,898(80)	748,857(25)	1,381,097(122)	1,225,231(126)	876,811(10)	1,108,977(399)
TD/CAT35	1,167,482(101)	944,791(25)	1,202,443(82)	1,564,630(117)	1,581,782(41)	1,301,944(387)
TS/TS	1,241,013(154)	1,381,722(43)	1,998,655(181)	1,434,913(105)	2,098,705(51)	1,616,947(602)
TS/CAT12	1,481,513(166)	1,014,059(24)	1,658,824(248)	1,534,048(126)	1,553,428(16)	1,499,137(632)
TS/CAT35	1,322,464(132)	956,345(33)	1,521,117(250)	1,286,289(148)	1,176,496(45)	1,321,840(653)
CAT12/ CAT12	1,560,377(22)	1,174,448(14)	1,596,021(65)	1,570,391(15)	1,942,321(4)	1,535,503(129)
CAT12/ CAT35	1,565,828(76)	1,112,906(21)	1,968,196(156)	1,273,766(104)	1,346,950(38)	1,557,651(426)
CAT35/ CAT35	1,463,555(28)	1,159,346(4)	2,484,408(58)	1,653,022(24)	2,870,798(6)	1,990,400(130)

Interestingly, when the same analysis is performed over the portion of land only, global averages show that at least in ATL, ECPA, NWP, and SPA storms with an LMI of a major

hurricane that makes landfall as either a TS or a TD they usually produce the most volumetric rain (Table 3.6). This result is opposite to Jiang et al. (2008), which showed that the TC volumetric rain decreases with TC current intensity as the storm makes landfall. Jiang et al. (2008)'s results were contaminated by the over-ocean portion of TC rain. After separating the over-land portion only, our findings partially agree with Touma et al. (2019), which suggested that the highest rainfall intensity and the largest rainfall area over land occur when major hurricanes have weakened and made landfall as tropical storms. Touma et al. (2019)'s results implied that the most volumetric rain would be from the TS/CAT35 category in the point-LMI category framework. However, our results in Table 3.7 and Figure 3.5c indicate that TC rainfall rate/intensity over land still increases with TC current/point intensity, which is the opposite of what Touma et al. (2019) concluded. On the other hand, Table 3.7 and Figure 3.5c suggest that TC rainfall area over land decreases with TC current/point intensity, which is the same as what Touma et al. (2019) reported. An important difference to consider between both studies is that Touma et al. (2019) used the TC rainfall data from meteorological rain-gauge stations over the United States. In their study, precipitation intensity was quantified as daily accumulations that match TC tracks at 1200 UTC. In contrast, in this study using satellite observations, intensity is obtained as the nearly instantaneous retrieval at the observation time (in mm/hour) over the pixels contained in each TCPF every three hours. With much higher temporal resolution and more robust sample sizes from the IMERG satellite, we conclude that the combination of decreasing precipitation intensity and increasing precipitating area as the TC intensity decreases when making landfall explains the maxima of point-LMI events with TD/CAT35 or TS/CAT35.

Table 3-6: Averaged tropical cyclone volumetric rain and number of samples (in parentheses) for each point-LMI category in global basins. Values are calculated over the portion of TC rain over land only.

Point Intensity/ LMI	ATL	ECPA	NWP	SIO	SPA	Global
TD/TD	490,557(27)	512,688(15)	516,225(66)	1,772,718(15)	233,166(21)	595,715(146)
TD/TS	495,133(326)	333,424(37)	686,394(268)	704,588(217)	613,145(122)	599,036(1105)
TD/CAT12	572,565(80)	269,224(25)	674,075(122)	489,416(126)	377,814(10)	524,224(399)
TD/CAT35	769,996(101)	788,967(25)	722,204(82)	618,615(117)	1,030,729(41)	729,524(387)
TS/TS	463,775(154)	462,458(43)	741,719(181)	549,765(105)	718,267(51)	621,434(602)
TS/CAT12	595,920(166)	410,451(24)	701,905(248)	615,257(126)	362,568(16)	634,463(632)
TS/CAT35	881,308(132)	522,611(33)	777,410(250)	583,934(148)	561,551(45)	718,013(653)
CAT12/CAT12	852,043(22)	439,814(14)	590,088(65)	810,545(15)	417,838(4)	651,937(129)
CAT12/CAT35	631,791(76)	554,324(21)	746,759(156)	754,742(104)	574,580(38)	702,966(426)
CAT35/CAT35	441,069(28)	617,749(4)	635,870(58)	728,387(24)	841,561(6)	629,466(130)

Table 3-7: Averaged tropical cyclone volumetric rain and samples size for each point-LMI category in the Atlantic basin. Values are calculated over the portion of TC rain over land and within the continental United States.

Point Intensity/ LMI	Sample size	Average rain rate	Average TC area	Volumetric rain
TD/TD	12	1.73	94,023	166,750.21
TD/TS	253	2.08	250,737	518,344.65
TD/CAT12	29	2.29	286,066	646,980.80
TD/CAT35	67	2.52	409,298	1,003,133.65
TS/TS	90	2.14	215,916	473,651.21
TS/CAT12	68	2.63	273,460	689,985.93
TS/CAT35	83	2.98	409,534	1,170,270.45
CAT12/CAT12	11	2.90	298,109	621,895.43
CAT12/CAT35	37	3.54	245,279	832,431.71
CAT35/CAT35	5	3.12	300,240	919,258.69

3.4.4 Environmental effects during landfalling stages

Variations of rainfall magnitude for each landfalling stage are analyzed for different TC translation speeds and environmental conditions. Figure 3.7 shows a set of 2D shear-relative TC rainfall composites describing the average influence of each variable differentiating between high/low values at different landfall stages. In terms of rainfall magnitude, previous investigations suggested that higher values in the storm motion speed (Burpee & Black, 1989; Lonfat et al., 2004), sea surface temperature (Lin et al., 2015), total precipitable water (Jiang et al., 2008, Hill et al., 2009), and low vertical wind shear (Cecile, 2007; Corbosiero & Molinari, 2002; Wingo & Cecil, 2010) boost the precipitation production. Our results shown in figure 3.7, for each of the above variables, confirm that these conclusions remain valid for all the landfalling stages (that accounts for the TCP area and distance from the coast) suggested in this paper.

In terms of the location of the most prominent rainfall rates, figure 3.7 shows that in landfalling TCs, the maximum values are concentrated downshear to downshear-left relative to the vertical wind shear direction. This result is consistent with previous researchers that found the same pattern for TC precipitation over the ocean (Chen et al. 2006, Cecil 2007, Jiang et al. 2008, Xu et al. 2014, and Pei and Jiang 2018) and over the land in localized regions (i.e., Xu et al. 2014 over China). In this study, we ratify that a downshear to downshear-left pattern remains valid for the before, during, and after-landfall stages on a global scale.

In general, it can be observed that the maximum intensity values occur in the During-landfall categories when exposed to high TC speed, TPW, and SST. Likewise, the minimum intensity values occur across the After-landfall categories when exposed to low values of the same variables. However, it is also noticed that the reduction of the intensity at After-landfall is accompanied by a general spread of the TCP from the areas of high concentration in the During-landfall and Before-

landfall stages, i.e., plots showing after-landfall rainfall exhibit more disorganized patterns but preserving clusters of rain near their original position before landfall. This result is consistent with the findings of Yu et al. (2015), in which the author indicates that the axisymmetric component (observed in the wavenumber 0) is preserved but rapidly decreases after landfall.

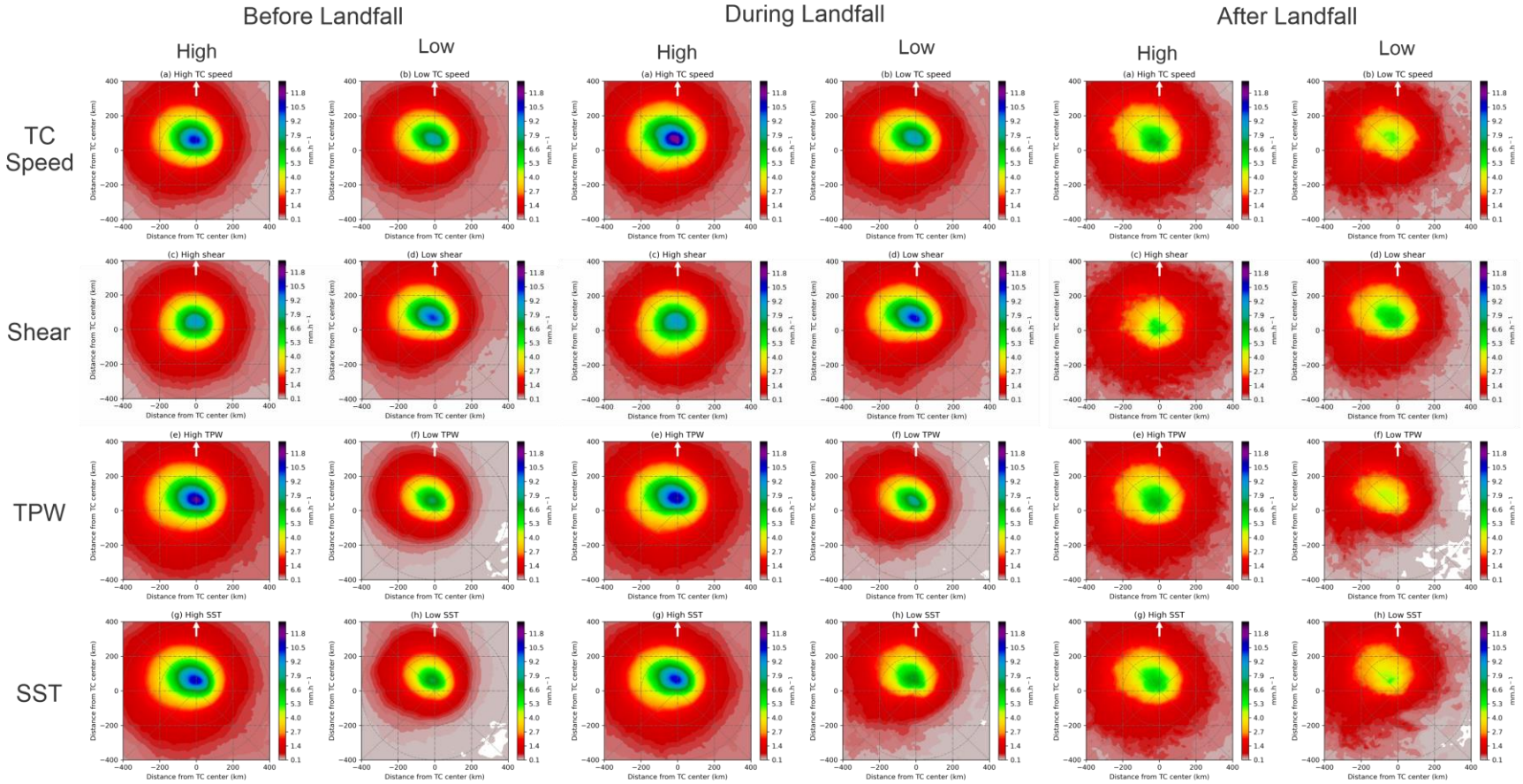

Figure 3-7: 2D composites of shear-relative rainfall rate produced by TCs in the different landfalling stages for low/high storm motion speeds, low/high shear magnitudes, low/high TPWs, and low/high SSTs. In all the panels, the direction of environmental vertical wind shear points upward as indicated by the white arrow.

3.5. Conclusions

The climatological averages of TCP rainfall before, during, and after landfall on a global basis are investigated using rainfall estimations from IMERG TRMM/GPM satellite data during 2000-2019. A new approach that combines the TCP area and the distance from the coast is proposed to characterize the TC rain magnitude at different landfall stages. Our observational results show that across the Ocean, Off-shore, and Pre-land categories, TCP experience a homogeneous enhancement controlled by the portion of the TC that remains over the ocean. Once the TCP area has reached at least 50% over the land, the overall precipitations rates begin to decay and the precipitation areas over land begin to expand, following a nearly perfect inversely proportional relation. This pattern is constant for all the landfalling stages until the TC totally disappears.

Our findings demonstrate that when the combined contribution of the rainfall occurs over the land and the ocean (as a total), there is a regular decrease in rainfall rates and volumetric rain. However, once the rainfall occurring over the land is analyzed independently, the volumetric rainfall slightly increases as the storm's intensity decreases while making landfall, finding maxima for CAT1 and TS. Further observational analysis using the concept of point-LMI categories demonstrates that TCs that at some point of their life cycle reached major hurricane strength and make landfall as TS or TD produced the highest volumetric rain over the land surface. This finding refines the previous investigation by Touma et al. (2019) that suggested that this effect was due to intensity and areal variations, but clarifying that the rainfall intensity over land still decreases as the storm's intensity decreases while making landfall while the volumetric rain increases due to the increase of raining area over land.

Finally, regarding the influence of environmental conditions, this research reaffirms that higher SST, TPM, and translation speed, combined with low VWS boost the precipitation production

regardless of the landfalling stage. In addition, the precipitation maximum is located downshear to downshear-left of the TC center regardless of the distance from the shore or the percentage of TCP area over the land, over all global basins. These findings are consistent with investigations focused on TCs over the ocean and some basin-localized landfall studies. Results of this study are useful for a better understanding of TCP at different landfall stages.

4. HEAVIER INNER-CORE RAINFALL OF MAJOR HURRICANES IN THE NORTH ATLANTIC BASIN THAN IN OTHER GLOBAL BASINS.

4.1 Abstract

Based on 19 years of precipitation data collected by the Tropical Rainfall Measuring Mission (TRMM) and the Global Precipitation Measurement (GPM) mission, a comparison of the rainfall produced by tropical cyclones (TCs) in different global basins is presented. A total of 1789 TCs were examined in the period from 1998 to 2016 by taking advantage of more than 47,737 observations of TRMM/GPM 3B42 multi-satellite derived rainfall amounts. The axisymmetric component of the TC rainfall is analyzed in all TC-prone basins. The resulting radial profiles show that major hurricanes in the Atlantic basin exhibit significantly heavier inner-core rainfall rates than those in any other basins. To explain the possible causes of this difference, rainfall distributions for major hurricanes are stratified according to different TC intensity and environmental variables. Based on the examination of these parameters, we found that the stronger rainfall rates in the Atlantic major hurricanes are associated with higher values of convective available potential energy, drier relative humidity in the low to middle troposphere, colder air temperature at 250hPa, and stronger vertical wind shear than other basins. These results have important implications in the refining of our understanding of the mechanisms of TC rainfall.

4.2 Introduction

The rainfall associated with tropical cyclones (TCs) is one of the most severe events affecting infrastructure and human activities in tropical and subtropical regions. The

severity of damage caused by TC rainfall has been highlighted in many recent studies (e.g., Willoughby 2012; Rapport 2014; Park et al. 2016), which has led to more attention to this topic in the priorities of the research and forecast communities. Nowadays, significant progress in the prediction of TC rainfall has been achieved through the use of extrapolation approaches from previous satellite observations (Kidder et al. 20005; Ferraro et al. 2005), climatology and persistent methods (Lonfat et al., 2007), and modern numerical models (Biswas et al. 2017). However, compared to the outstanding advancements in the prediction of TC tracks, the quantitative precipitation forecast of TC still shows modest skill (Lonfat 2004, Tuleya et al. 2007).

In the case of the forecast techniques that use the persistence and climatological information as a starting point to predict rainfall rates, a permanent refinement of climatological features of TC rainfall is a critical step in producing more accurate results, especially for the most active areas within the TC structure like the inner-core region. One key element in this forecasting approach is the mean radial distribution of rainfall, as Lonfat et al. (2004) described. In that study, based on three years of rainfall estimates produced by the Tropical Rainfall Measuring Mission (TRMM) microwave imager (TMI), the authors examined the radial distribution of azimuthally rainfall rates from the storm center to a 500-km radius. Their results suggested a close relationship between TC intensity and the precipitation rate, showing a peak in the inner-core region that ranges from 3 mm.h-1 for tropical storms to about 12 mm.h-1 for major hurricanes. These axisymmetric profiles have served as the foundation to construct instantaneous footprints of TC rainfall as a function of the storm intensity in forecasting models like R-CLIPER and its successor, the

Parametric Hurricane Rainfall Model (PHRaM, Lonfat, et al. 2007). However, adding the effect of environmental conditions in the TC rainfall forecast is still under development.

Numerous studies have also shown that the distribution of TC rainfall is affected by environmental conditions, including but not limited to factors such as humidity, wind shear, and sea surface temperature. In terms of humidity, Jiang et al. (2008), using TRMM 3B42 observational data, found empirical relationships that explain the total volumetric rain as a function of total precipitable water, horizontal moisture convergence, and ocean surface flux for the Atlantic basin with higher correlations coefficients than previous works based on TC intensity only. In the case of wind shear, Cecil (2007), using the Special Sensor Microwave Imager (SSM/I) and TMI data, found that when TCs interact with environmental wind shear, they acquire an asymmetric structure depicted by rainfall enhancement in down-shear directions and to the left of the shear vector. The magnitude of this shear-related enhancement oscillates in a factor of two to four when comparing the inner 100 km with the unfavored quadrants, depending on the wind shear magnitude and distance from the TC center. Finally, in the case of the sea surface temperature, Lin et al. (2015) examined the relation between TC rainfall area and the relative sea surface temperature, the latter is defined as the sea surface temperature (SST) in the TC environment minus the average tropical SST (30°N-30°S). They found strong dependencies of TC rainfall area on the relative SST in all the TC intensity categories. Their study reported a weak relationship between TC size and intensity and showed that the rainfall rate increases with increasing the absolute SST, especially towards the TC center.

Previous climatological studies provided valuable insight into better understanding the quantitative prediction of TC rainfall and their global variation. Jiang and Zipser (2010), using 8-year of TRMM data, described the contribution of TCs to total rainfall in each of the TC-prone global basins. Their study reported inter-basin differences that result in an overall differential contribution of 8%–9%, 7%, 11%, 5%, 7%–8%, and 3%–4% for the north Atlantic, northeastern Pacific, northwestern Pacific, north Indian Ocean, southern Indian Ocean, and southern Pacific basins, respectively. Lonfat et al. (2004) examined the azimuthal mean rain rate in TCs in terms of different TC intensity categories and different TC-prone basins. However, they only used three years of TRMM data, and no significant tests were performed in their study, probably due to the small sample size. Therefore, the present study is motivated to refine the global TC rainfall climatology by using a much longer time series that consists of 19 years of multi-satellite derived rainfall amounts collected from the NASA TRMM and its successor the Global Precipitation Mission (GPM). Here, we mainly focus on characterizing the radial distribution of the azimuthal mean rainfall rates within the different global basins and different TC intensity categories. The resulting climatological differences are then linked to various potential environmental factors whose effects are examined individually to provide inter-basin comparisons focused on the inner core region of major hurricanes.

4.3 Data and Methodology

4.3.1 Data

The analysis period spans from 1998 to 2016, covering all the TC-prone global basins grouped into four geographic zones: Northern Atlantic (ATL), East-Central Pacific

(ECPA), Northwestern Pacific & Northern Indian Ocean (NWP+NIO), and Southern Hemisphere (SH). Note that the NIO basin is combined with the NWP basin due to the small sample size of NIO TCs. TCs in southern Indian Ocean and southern Pacific basins behave similarly in term of the properties studied here, therefore are combined as well. A total of 1789 TCs are analyzed with a sample distribution that consists of 315 in ATL, 363 in ECPA, 637 in NWP&NIO, and 474 in SPA, respectively (Table 4.1). Rainfall information is obtained from the multi-sensor precipitation estimate TRMM/GPM 3B42 (Version 7). The 3B42 data provide gridded rainfall information on a 3-hour temporal resolution and a 0.25-degree by 0.25-degree spatial resolution, covering the latitude band from 50°N to 50°S. Each microwave precipitation estimate is best interpreted as the precipitation rate effective at the nominal observation time (Huffman et al. 2007).

Table 4-1: Number of TCs, major hurricanes, and corresponding 3B42 observations during 1998-2016 in different basins.

Variable	ATL	ECPA	NWP&NIO	SH	Total
Number of TCs	315	363	637	474	1789
3B42 observations	8,567	9,176	16,581	13,413	47,737
Number of major hurricanes	63	75	188	137	463
3B42 observations for major hurricanes	581	527	1798	1090	3996
Number of CAT5 hurricanes	10	8	56	23	97
3B42 observations for CAT5 hurricanes	45	22	216	76	359

The TC positions, time, and maximum sustained wind speed are obtained from the International Best Track Archive for Climate Stewardship (IBTrACS version 4), which is

a global collection of best-track data from multiple meteorological agencies to provide a complete global climatology of TCs (Knapp et al. 2018). Only storms in which the 3B42 extent covers the entire inner-core area are considered. To satisfy this condition, we removed those best track positions beyond 46°N and 46°S (approximated 440km before the edge of the 3B42 border). TCs identified as extratropical were removed using the flags available in columns 23 and 26 of the IBTrACS database. The final dataset includes TCs over both ocean and land. Considering the differences in the reported values from the independent national services working in the Pacific basins, a meticulous cross-check is performed to favor the information from the US Navy's Joint Typhoon Warning Center (JTWC). Regarding intensity categories, based on the definitions in the IBTrACS data, a tropical depression (TD) refers to a system with wind speed from 10 to 33 knots and a tropical storm (TS) is a system with wind between 34 and 63 knots. The hurricane categories 1 to 5 (CAT1, CAT2, CAT3, CAT4, and CAT5) are adopted from the Saffir-Simpson wind scale.

Variables that characterize the environmental conditions around the storms are obtained from the most recent version of the Statistical Hurricane Intensity Prediction Scheme (SHIPS, Last updated: July 2018) developmental dataset, which includes 6-hour retrievals of observational and derived data of more than 80 TC parameters, including predictions up to 120 hours over various annular regions calculated from the TC center (DeMaria and Kaplan 1994, 1999; DeMaria et al. 2005; Schumacher et al. 2013). In the current study, we made an initial selection of twelve SHIPS environmental parameters to be examined: Reynolds sea surface temperature (RSST), wind shear with vortex removed and averaged from 0-500km (SHDC), wind shear heading averaged from 0-500km

(SHDD), climatological ocean heat content (COHC), average potential temperature θ_e difference between a parcel lifted from the surface and its environment with only positive differences considered in the averages (EPOS), which is parameter similar to the convective available potential energy (CAPE), total precipitable water between 0 to 200 and 0 to 500 (MTPW), relative humidity at three different levels including surface (R000), the 850-700 hPa layer from 200-800km (RHLO), and the 700-500 hPa layer from 200-800 km (RHMD), and lastly, the temperature at both the surface (T000) and the 250 hPa level from 200-800km (T250). Only the values at the initial time (t=0) are employed in our analyses.

4.3.2 Axisymmetric precipitation and 2D plots

In this study, the radial variation of precipitation is determined by the azimuthal mean rainfall rate in 40 steps of 25-km wide annuli from the TC center outward to the 600 km, in storm-relative coordinates. This procedure is based on calculating the wavenumber zero of the Fourier transformation (azimuthal average) as reported in previous investigations (e.g., Lonfat et al. 2004; Chen et al. 2006; Kim et al. 2018). Considering 25-km is nearly the pixel size resolution, a scheme in which the map coordinates are assigned to the pixel's center was adopted. Thus, the algorithm only includes pixels when more than half of its size is within the annulus. During the selection of values to consider in the calculations, a threshold of rainfall rates greater than 0.01 $mm.h^{-1}$ is used to obtain the averages. The calculation of axisymmetric precipitation is applied to each available record in the combined best-track and SHIPS database to examine the radial dependence of TC precipitation as a function of the storm intensity and geographic location (Figures 4.1 and

4.2). As part of the axisymmetric analysis, the radius of maximum azimuthal rain rate (RMR) of each storm is also calculated to allow geometric inter-basin comparisons (Figure 4.3). The RMR is defined as the radius of the azimuthal mean maximum rainfall within a 400 km radius from the TC center (Shimada et al. 2018); this parameter is extracted as a proxy for the radius of maximum wind. Finally, and to further examine each rainfall rate contribution to the mean values with radial distance, the probability density function (PDF) of rain occurrence in each annulus is determined by classifying the 3B42 rain estimates in equally-distributed classes within a logarithm scale. Using the annular PDFs series, contoured frequency by radial distance (CFRD) diagrams are constructed for each basin (Figures 4.3 and 4.4). This procedure is implemented in the same way as Lonfat (2004) and Jiang et al.(2008) described.

In addition to the axisymmetric profiles, bidimensional plots showing the spatial distribution of the composite TC rainfall are created in storm-centered coordinates (Figure 4.5). The composite procedure starts from each of the best track positions by selecting the pixels contained in the envelope of a radial buffer from the TC center to 500km in the 3B42 files. Once obtained, the hurricane-centered grid is rotated along the vertical wind shear vector using the heading values reported in the SHIPS database (variable SDDC). Then, the average rainfall rate is calculated for each cell position in the storm-centered array and categorized by basin.

4.3.3 Mean values, statistical tests, and spatial distribution maps

The average inner-core rainfall rates are calculated in the region from the TC center to 150km. In this procedure, we used the same pixel selection rules employed in the

algorithm for the azimuthal rainfall rate estimations. To allow comparison through paired observations with the environmental variables, averaged values are calculated only for those best track records that match with the SHIPS database. Then, the averaged values of the rain and SHIPs variables are categorized by basin. As a second step, a statistical test is used to determine if there is a significant difference for the means of the inner-core rainfall rate values and environmental variables among different basins. The normal distribution of each sample is verified using Shapiro-Wilk normality tests to subsequently apply either a T-Test or a Mann-Whitney U-test, as required by the statistical normality of the data.

To examine the spatial distribution of inner-core rainfall rates and environmental variables, two types of maps are created: In the first category (Figures 4.6, 4.8-4.12), point-based maps representing major hurricane centers of each observation are color-coded by intervals of inner-core rainfall rates and environmental variables. Class intervals are initially created using four Jenks' natural breaks in which at least one class is below the global average, and the remaining three are created in the direction of the maximum variation. Once obtained, break limits are rounded to facilitate the map interpretation. In the second category (Figure 4.7), a continuous map showing normalized accumulation of inner-core rainfall is created from the 3B42 data. The normalized values result from the ratio between the total accumulated rain and the number of samples at each geographic location. Finally, the resulting map is resampled to a 2-degree by 2-degree grid and then color-coded using the same approach of the point-based maps, but for a higher number of intervals.

4.4 Results

4.4.1 Axisymmetric findings

Figure 4.1 shows the radial distribution of azimuthally average rainfall rates stratified by geographic location and intensity categories. In all the cases, there is a positive relationship between TC intensity and the precipitation rate, being more evident in the region within the first 300 km from the TC center. In the region from 300 to 550km, rainfall rates uniformly decrease outward to 1 mm.h-1, and in the case of the area beyond 550km, the rainfall rate tends to be nearly the same for all the TC intensity categories. In general, mean rainfall rates increase with the storm intensity at all radii. The shorter the distance from the TC center, the higher rainfall rates, except for the annuli associated with the storm's eye.

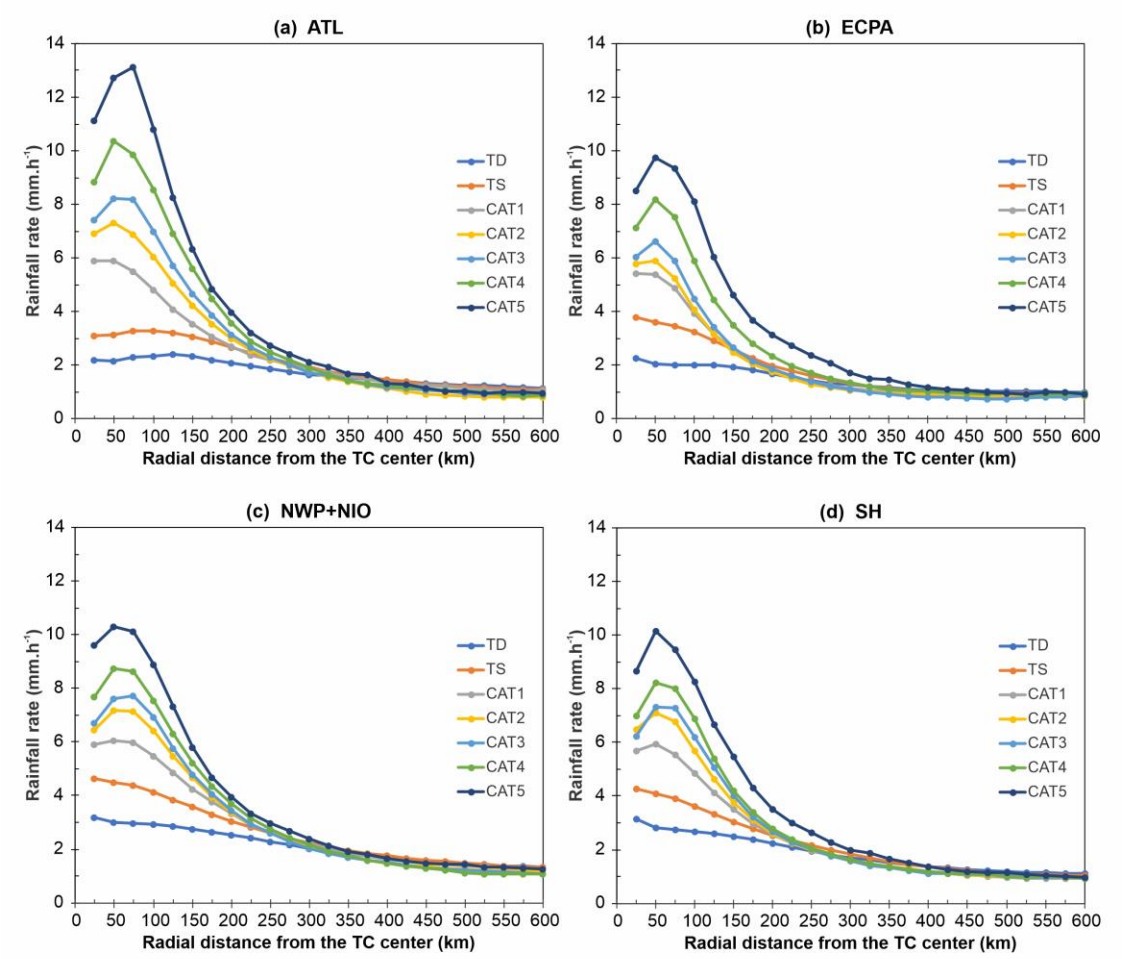

Figure 4-1: Radial distribution of azimuthally averaged rainfall rate of TCs during 1998-2016 in different intensity categories in (a) ATL, (b) ECPA, (c)NWP+NIO, and (d) SH basins

Globally, TDs and TSs exhibit their maximum rainfall rate in the vicinity of their geometric center, in an intensity interval between 3 and 4 mm.h-1. In contrast, CAT1 to CAT5 storms show their peaks between 6 and 10.7 mm.h-1, ranging from 50 to 70 km from the TC center. However, the Atlantic basin exhibits more pronounced rainfall rates in the inner-core region (Figure 4.1a), mainly within major hurricane categories (CAT3-5).

At their peak, Atlantic rates differ from the global average rates by +6.4%, +13.9%, and +18.8% for CAT3, CAT4, and CAT5, respectively.

The same pattern appears in the mean inner-core rainfall rates summarized in Table 4.2. It can be seen that for major hurricanes, the Atlantic basin produces heavier inner-core rainfall than other basins, and its rainfall rate surpasses the global averages. Results of the T-test and Mann-Whitney U-test indicate that there is a significant difference between the mean values of the Atlantic with respect to the other basins. In all the major hurricane cases, the statistical significance difference exceeds 90%, and for CAT4 and CAT5, significance values range from 99% to 99.9% in all the inter-basin comparisons.

Table 4-2: Comparison of average inner core rainfall rate (mm.h-1) within 150 km from the TC center for different TC intensity categories and different TC-prone basins in the period 1998-2016. a, b, c, and d denote that the statistical significance of the difference between each basin versus the ATL basin is at the 90%, 95%, 99%, and 99.9% confidence level. Significance is calculated with respect to Atlantic averages

Category	ATL	ECPA	NWP&NIO	SH	Global mean	Global mean excl. ATL
Tropical depression	2.30	1.95 *d*	2.86 *d*	2.61 *d*	2.51 *d*	2.55 *d*
Tropical storm	3.18	3.07 *b*	4.00 *d*	3.46 *d*	3.49 *d*	3.58 *d*
Category 1	4.62	3.72 *d*	5.18 *d*	4.52	4.64	4.64
Category 2	5.69	3.79 *d*	5.93	5.22 *d*	5.33 *d*	5.27 *d*
Category 3	6.42	4.17 *d*	6.29 *a*	5.58 *d*	5.76 *d*	5.64 *d*
Category 4	7.77	5.32 *d*	6.91 *d*	6.08 *d*	6.61 *d*	6.42 *d*
Category 5	9.54	6.77 *d*	7.98 *c*	7.33 *d*	7.93 *c*	7.72 *c*

Figure 4.2 shows the differences in the mean radial profiles between major hurricanes and the rest of the intensity categories; these axisymmetric profiles confirm the presence of geographical variations of rainfall rates from basin to basin. On the one hand,

major hurricanes exhibit an ascending sequence of rainfall intensity that begins with ECPA, followed by SH and NWP+NIO, and finishing with ATL as the basin with the heaviest rainfall rate. This intensity order is preserved across the inner-core region but changes beyond 150-175 km from the TC center, where NWP+NIO starts to exhibit the highest rainfall rates (Figure 4.2a). On the other hand, TD, TS, and minor hurricanes show a different ascending order in the basin intensities. In their case, the sequence begins with ECPA, followed by SH and ATL, and finishing with NWP+NIO. However, Atlantic TCs reduce their rainfall rates below the SH averages in the inner-core region (Figure 4.2b).

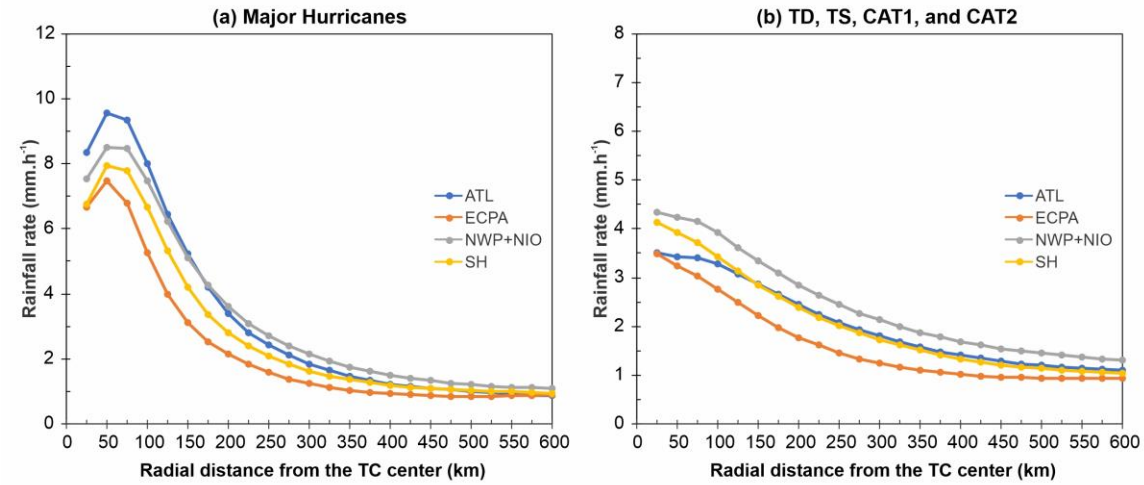

Figure 4-2: Radial distribution of azimuthally averaged rainfall rate of (a) major hurricanes and (b) TCs with intensity less than major hurricanes during 1998-2016 in different basins.

Figures 4.3 and 4.4 show the rain-rate frequency distributions with radial distance computed outward to the 600-km radius from the TC center. Figure 4.3 focuses on the frequencies for major hurricanes across different basins. Within the 50 to 200-km radius, distributions are relatively narrow, with values more concentrated around the mode and short symmetrical tails (i.e., little to no skewness and a modest leptokurtic pattern). Beyond

200-km the distribution broadens, becoming left-tailed with the mean and mode in direction to the highest rainfall rates.

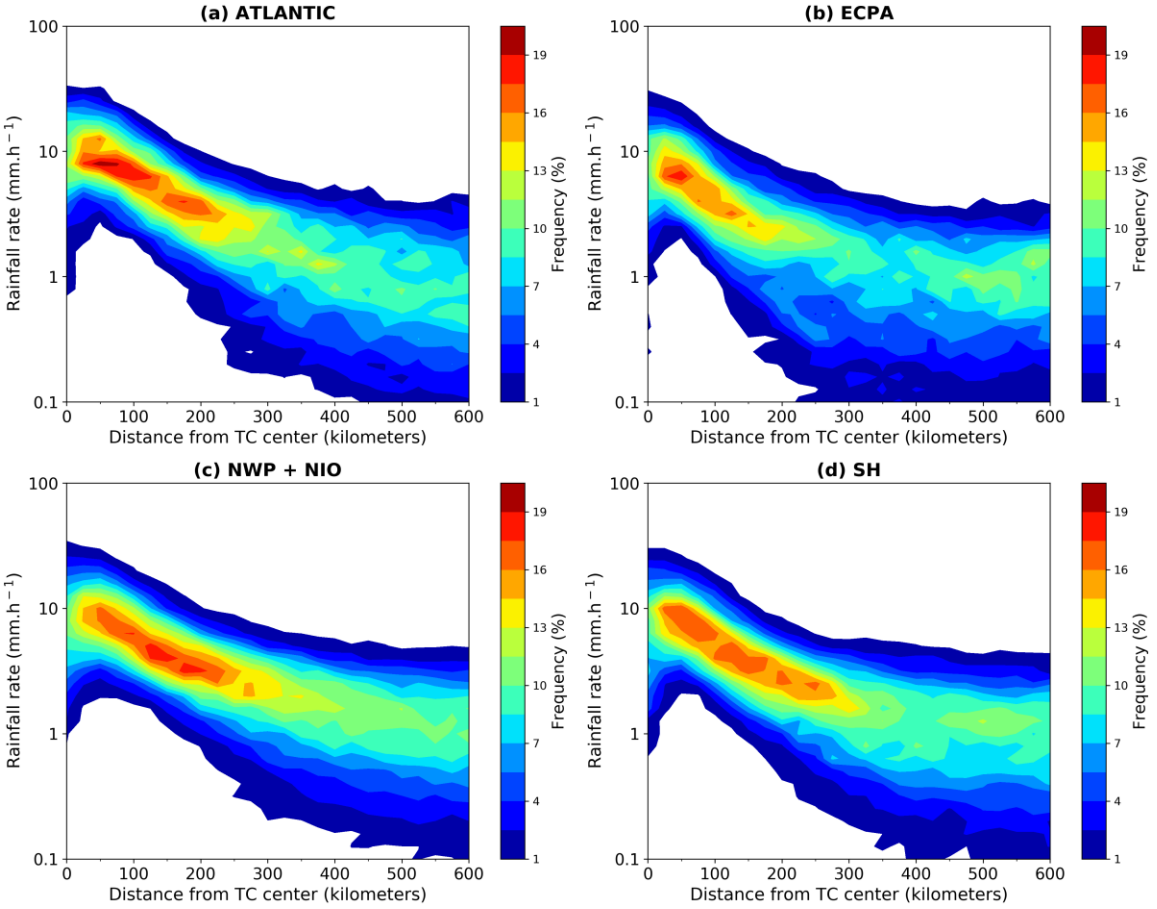

Figure 4-3: Radial distribution of rainfall PDFs computed for major hurricanes in (a) ATL, (b) ECPA, (c)NWP+NIO, and (d) SH basins

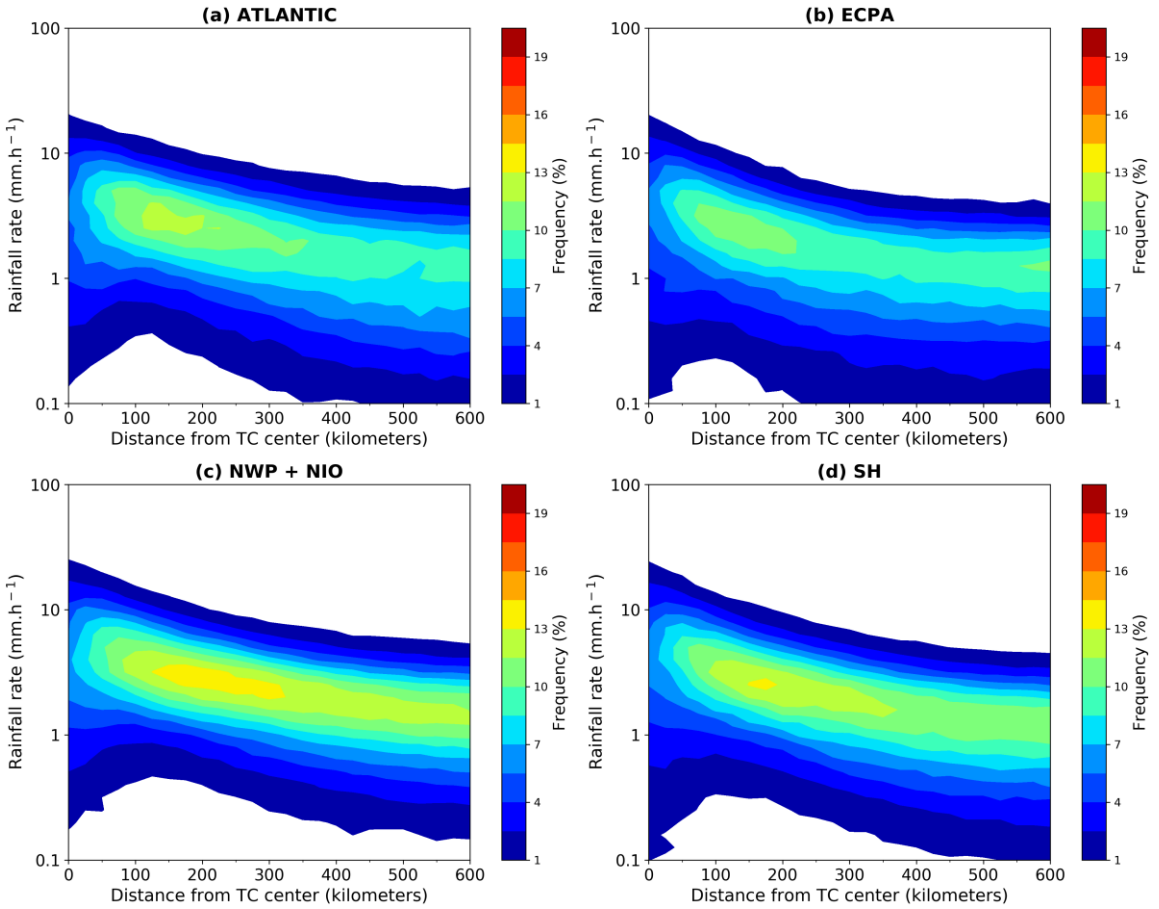

Figure 4-4: Radial distribution of rainfall PDFs computed for TCs with intensity less than major hurricanes in (a) ATL, (b) ECPA, (c)NWP+NIO, and (d) SH basins.

Inter-basin comparison shows that Atlantic storms have more occurrences of high inner-core rainfall rate values within the first 150-km than other global basins (Figure 4.3a), reaching precipitations near 8-11 mm.h-1 with frequencies above 17%. This basin also exhibits more frequent events surpassing 10 mm.h-1. NWP+NIO and ECPA reveal relatively similar PDFs in the region between 50 and 300-km, except for a more pronounced mode around 150km. ECPA storms show high frequency in the first 150-km but a broader expansion of rainfall rates beyond this range. In contrast with the notable variations observed in major hurricanes, Figure 4.4 shows that TD, TS, and minor

hurricanes have more homogeneous PDFs in the inner-core, though exhibiting slightly higher frequencies in the region from 150 to 300-km, especially in NWP+NIO and SH basins.

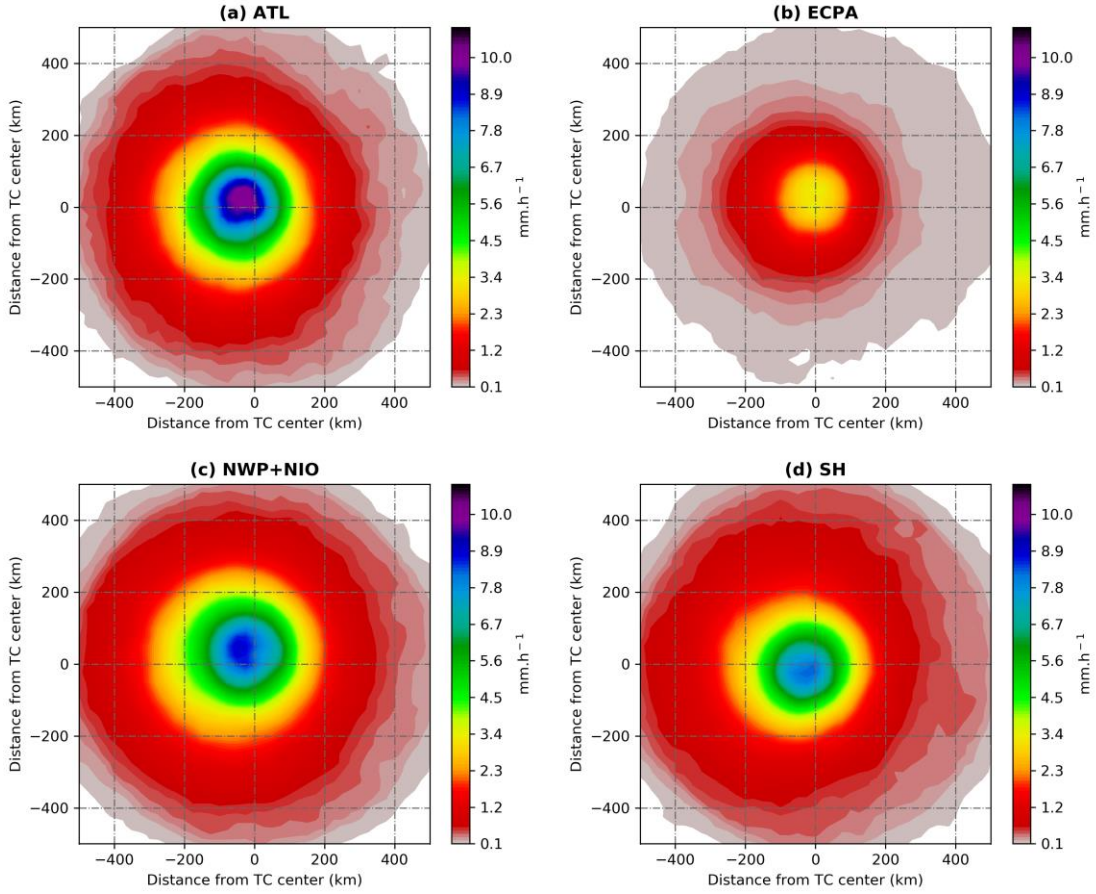

Figure 4-5: 2D Composite shear-relative rainfall rate produced by major hurricanes during 1998-2016 in (a) ATL, (b) ECPA, (c)NWP+NIO, and (d) SH basins. The shear direction is pointing upward.

Two-dimensional plots shown in Figure 4.5 describe the distribution of rainfall rates for major hurricanes across different basins in storm-centered coordinates, with the shear direction pointing upwards. In concordance with observational and modeling studies (e.g., Cecil, 2007; Wingo, 2010), this plot shows that rainfall is favored in the down shear

direction and also to the left to the shear vector in the northern hemisphere, and up-shear-right for those storms occurring in the southern hemisphere. These plots confirm the presence of geographical variations of rainfall rates on a basin basis, in which major hurricanes exhibit an ascending sequence of rainfall intensity that begins with ECPA as the weakest (Figure 4.5b), followed by SH (Figure 4.5d), NWP+NIO (Figure 4.5c), and finishing with ATL as the basin with the heaviest rainfall rate (Figure 4.5a).

4.4.2 Geographic distribution of major hurricane precipitation

Figure 4.6 shows the spatial distribution of major hurricane centers along global basins. In this map, the frequency and TC center positions are color-coded for 4 different mean inner-core rain categories. It can be observed that rainfall rates below 6 mm.h-1 are dominant in all basins except for the Atlantic, where the most frequent rates oscillate in the range from 6 to 12 mm.h-1. Similar patterns can be found along the 6-12, 12-18, and >18 mm.h-1 intervals, in which the pattern of heavier inner-core rains in the Atlantic basin appears systematically. Table 4.3 summarizes the number and percentage of observations that match with Figure 4.6. Here, the percentage of the number of events with more intense precipitation is higher in the Atlantic basin. Considering that the most representative percentual differences occur in the lower intervals (i.e., not in the most extreme events), we discard the hypothesis that unusual events are the cause that produces these differences.

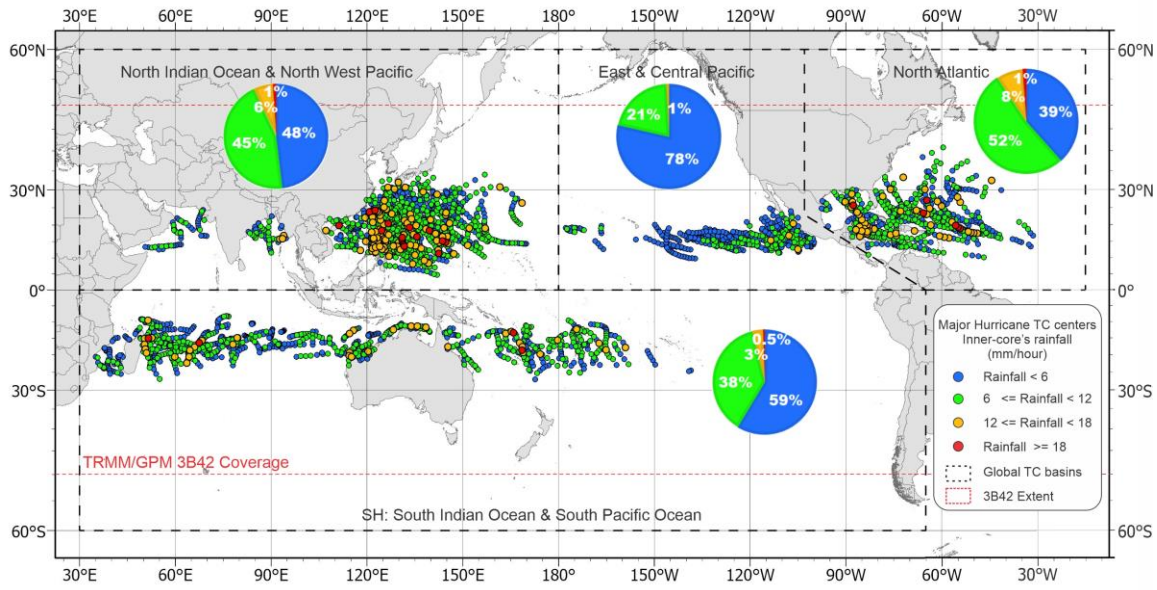

Figure 4-6: Global map showing the locations of the centers of major hurricanes for each 3B42 overpass categorized by different mean inner-core rain levels. Pie charts illustrate the percentage of observations for each rainfall rate category in each basin.

Table 4-3: Number and percentage of major hurricane observations in different inner-core mean rain rate categories.

Variable	ATL	ECPA	NWP&NIO	SH	Total
Inner-core rain < 6 mm.h^{-1}	223 38.4%	414 78.6%	865 48.1%	639 58.6%	2,141 53.6%
6-12 mm.h^{-1}	304 52.3%	109 20.7%	808 44.9%	410 37.6%	1,631 40.8%
12-18 mm.h^{-1}	48 8.3%	4 0.8%	108 6.0%	36 3.3%	196 4.9%
>18 mm.h^{-1}	6 1.0%	0 -	17 0.9%	5 0.5%	28 0.7%
Total of 3B42 observations for major hurricanes	581	527	1,798	1,090	3,996

Figure 4.7 illustrates the spatially-normalized TC rainfall produced by the inner-core in a 2-degree gridded representation at a global scale. In this map, the places with the heavier precipitation in the inner core are easily distinguishable (colors red and magenta). Although an important number of these locations follow random patterns, it can be

observed that some of the rainiest places are co-located over sectors of well-recognized oceanic warm currents. In the particular case of the Atlantic basin, rainiest events (greater than 14 mm.h-1) appear clustered across two branches, the first branch flows north and east of the West Indies, nearly along the 60W parallel, and the second flows into the Caribbean Sea following the Caribbean and the Gulf of Mexico currents. This map also shows the histograms that describe the distribution of pixel values in each basin. It can be seen that whereas the NWP+NIO basin has a normally-distributed histogram, SH, ECPA, and ATL follow skewed distributions. For instance, ECPA exhibits more frequency of lighter rainfall events, and ATL and SH observe histograms tailed to the right, in which the Atlantic storms reach heavier rainfall rates.

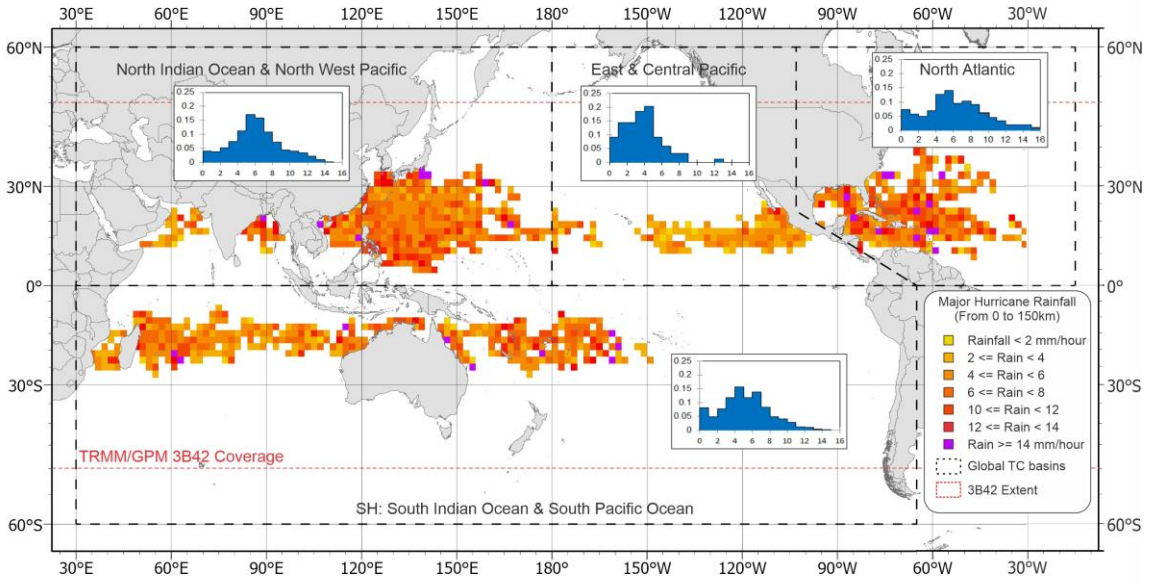

Figure 4-7: Map showing the spatial distribution of the normalized TC rainfall produced by major hurricanes in the period 1998-2016 (only the inner-core region is considered). Pixel size resampled to 2x2 degree for better representation. Histograms show the normalized frequency of inner-core rainfall rate values for each basin.

4.4.3 Environmental parameters around major hurricanes

As one of the potential causes to explain the heavier inner-core rainfall rates in the Atlantic basins, some environmental variables available in the SHIPS developmental database are examined (see discussion section). As the first step, an initial selection of twelve variables was considered. However, we discarded most of them after performing a significance test of the difference between each basin's mean values with reference to mean values in the ATL basin. Table 4.4 shows the final selection of environmental variables along with their corresponding levels of significance. It can be observed that ATL exhibits the lowest values of RHLO, RHMD, and T250. Likewise, ATL shows the highest EPOS globally and shear values in the northern hemisphere.

Table 4-4 Mean value of inner-core rain, VMAX, and environmental variables of major hurricanes during 1998-2016 in different basins. a , b, c, and d denote that the statistical significance of the difference between each basin versus the ATL basin is at the 90%, 95%, 99%, and 99.9% confidence level. Significance is calculated with respect to Atlantic averages using either a T-test or Mann-Whitney U-test.

Variable	ATL	ECPA	NWP &NIO	SH	Global mean	Global mean excluding ATL samples
Mean rainfall within 150 km (mm)	7.28	4.63 ^{d}	6.78 ^{d}	5.95 ^{d}	6.34 ^{d}	6.18 ^{d}
VMAX (knots)	115.66	112.98 ^{d}	118.06 ^{c}	114.4^{a}	116.05	116.12
SHDC ($m.s^{-1}$)	11.67	8.27 ^{d}	10.37 ^{d}	12.45	10.85 ^{c}	10.71 ^{d}
EPOS (deg C)	11.08	7.45 ^{d}	10.03 ^{d}	8.38 ^{d}	9.39 ^{d}	9.10 ^{d}
RHLO (%)	70.27	72.98 ^{d}	75.51 ^{d}	75.21 ^{d}	74.33 ^{d}	75.02 ^{d}
RHMD (%)	58.07	63.92 ^{d}	64.93 ^{d}	62.38 ^{d}	63.10 ^{d}	63.96 ^{d}
T250 (deg C)	-40.22	-39.93 ^{d}	-37.93 ^{d}	-38.81 ^{d}	-38.76 ^{d}	-38.52 ^{d}

Based on the above result, further analysis on the statistical and spatial distribution of the differences are investigated. Thus, Figure 4.8 and Table 4.5 show that EPOS greater

than 12°C presents higher occurrence in the Atlantic basin (37%), more than double than in other global basins. In terms of spatial distribution, the highest EPOS values in ATL are fairly co-located with the highest rainfall rates shown in Figures 4.6 and 4.7. Interestingly, EPOS in this interval shows little spatial correlation with the maximum rainfall rates in the other basins.

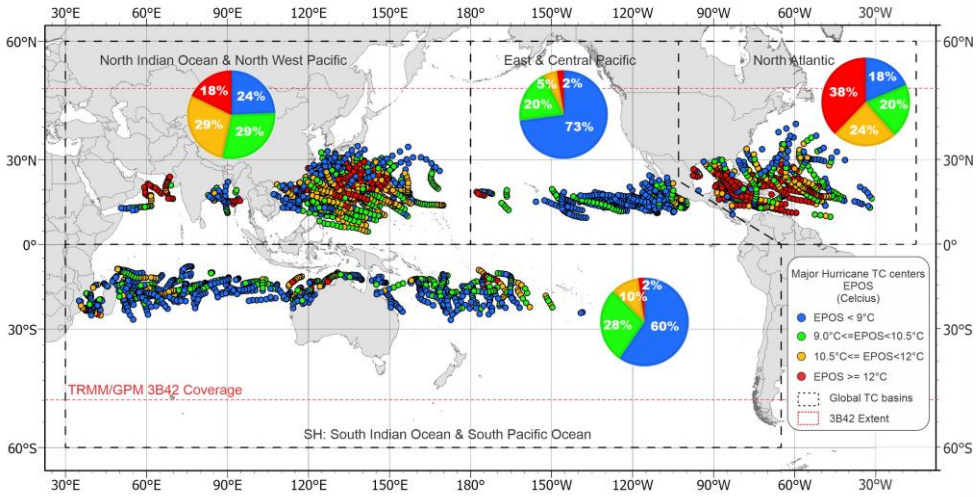

Figure 4-8: Global map showing the centers of major hurricanes for each SHIPS data point categorized by different EPOS levels. Pie charts illustrate the percentage of observations for each EPOS category in each basin.

Table 4-5: Number and percentage of major hurricane observations in different categories of EPOS

Variable	ATL	ECPA	NWP&NIO	SH	Total
EPOS < 9°C	108	384	439	650	1,581
	18.6%	72.9%	24.4%	59.6%	39.6%
9.0°C – 10.5°C	116	104	521	302	1,043
	20.0%	19.7%	29.0%	27.7%	26.1%
10.5°C – 12.0°C	138	26	517	113	794
	23.8%	4.9%	28.8%	10.4%	19.9%
EPOS >12°C	219	13	321	25	578
	37.7%	2.5%	17.9%	2.3%	14.5%
Total of 3B42 observations for major hurricanes	581	527	1,798	1,090	3,996

Regarding relative humidity differences, Figure 4.9 and Table 4.6 show that RHLO below 70% is the most dominant feature in the ATL. On the contrary, values above 75% are the most frequent in other basins. ATL also exhibits the most frequent intermediate intervals of RHLO in the range from 70-75%. Likewise, identical patterns occur with RHMD (Figures 4.10 and Table 4.7) in which dryer environments appear more commonly in the Atlantic basin, particularly in storms with RHMD below 60%. From the spatial perspective, it is difficult to establish well-defined patterns to link the highest precipitation rates with relative humidity differences. However, by contrasting Figure 4.7 with Figures 4.9 and 4.10, it can be seen that relative humidity contributes differently to the production of rainfall in the Atlantic basin. For instance, while ECPA storms seem to be favored by the moister environment, the Atlantic seems favored by slightly drier conditions below the global averages.

Table 4-6: Number and percentage of major hurricane observations in different categories of RHLO

Variable	ATL	ECPA	NWP&NIO	SH	Total
RHLO < 70%	251 43.2%	151 28.7%	261 14.5%	222 20.4%	885 22.1%
70.0% - 72.5%	118 20.3%	85 16.1%	206 11.5%	122 11.2%	531 13.3%
72.5% -75.0%	105 18.1%	91 17.3%	307 17.1%	158 14.5%	661 16.5%
RHLO >75.0%	107 18.4%	200 38.0%	1024 57.0%	588 53.9%	1919 48.0%
Total of 3B42 observations for major hurricanes	581	527	1,798	1,090	3,996

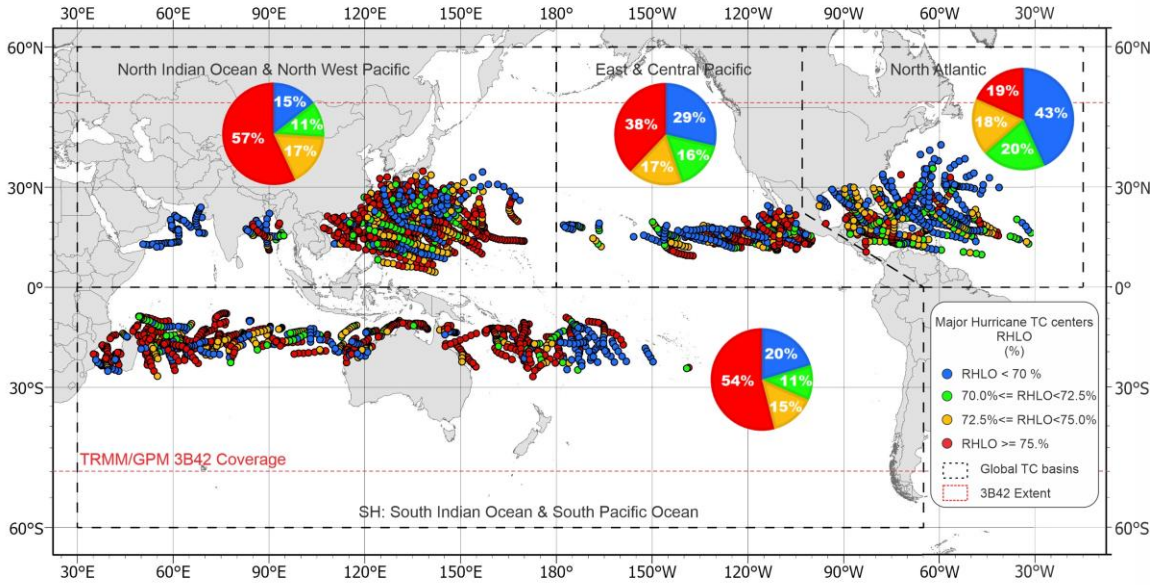

Figure 4-9: Global map showing the locations of the centers of major hurricanes for each SHIPS data point categorized by different RHLO levels. Pie charts illustrate the percentage of observations for each RHLO category in each basin.

Table 4-7: Number and percentage of major hurricane observations in different categories of RHMD

Variable	ATL	ECPA	NWP&NIO	SH	Total
RHMD < 60%	307 52.8%	182 34.5%	555 30.9%	400 36.7%	1444 36.1%
60.0% - 62.5%	76 13.1%	46 8.7%	134 7.5%	89 8.2%	345 8.6%
62.5% - 65.0%	47 8.1%	31 5.9%	106 5.9%	79 7.2%	263 6.6%
RHLO > 65.0%	151 26.0	268 50.9%	1003 55.8%	522 47.9%	1944 48.6%
Total of 3B42 observations for major hurricanes	581	527	1,798	1,090	3,996

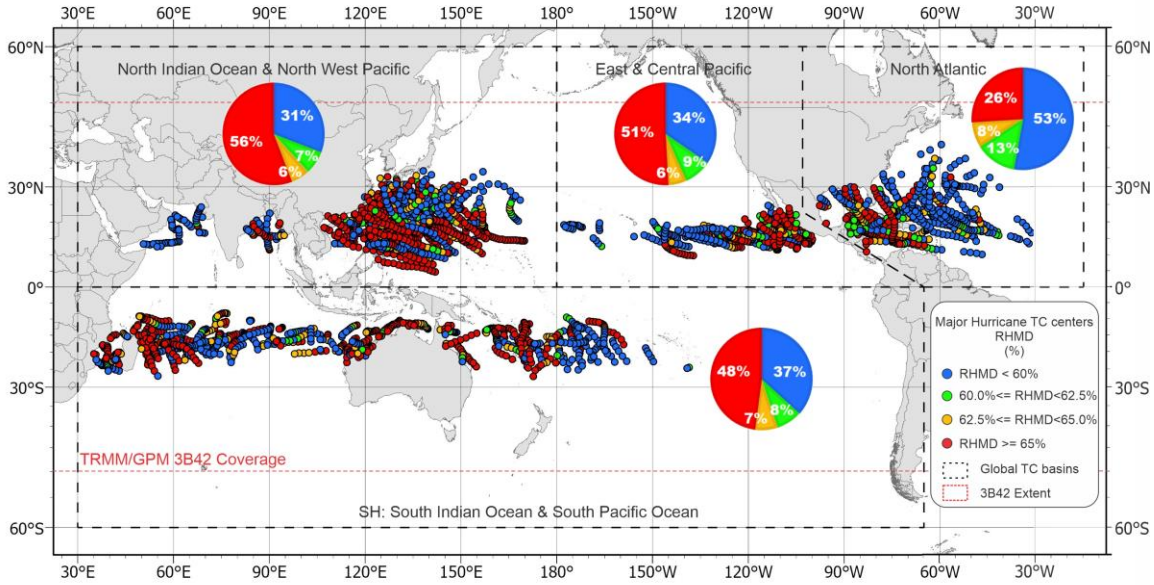

Figure 4-10 Global map showing the locations of the centers of major hurricanes for each SHIPS data point categorized by different RHMD levels. Pie charts illustrate the percentage of observations for each RHMD category in each basin.

About wind shear, Figures 4.11 and Table 4.8 show that the Atlantic has the highest frequency of storms above the 11 and 12 m.s-1, with a relatively similar distribution to the trend observed in the SH. In contrast, ECPA shows its highest frequency in environments with wind shear in the lowest interval below 10 m.s-1. NWP+NIO reveal a behavior in between. Spatially, wind shear values are slightly stronger poleward in all basins, following a random pattern with little co-location to the heaviest rainfall rates. Finally, Figures 4.12 and Table 4.9 show that the most predominant temperatures at 250 hPa in the Atlantic basin occur below -40°C. Interestingly, NWP+NIO has the opposite frequency distribution in each interval.

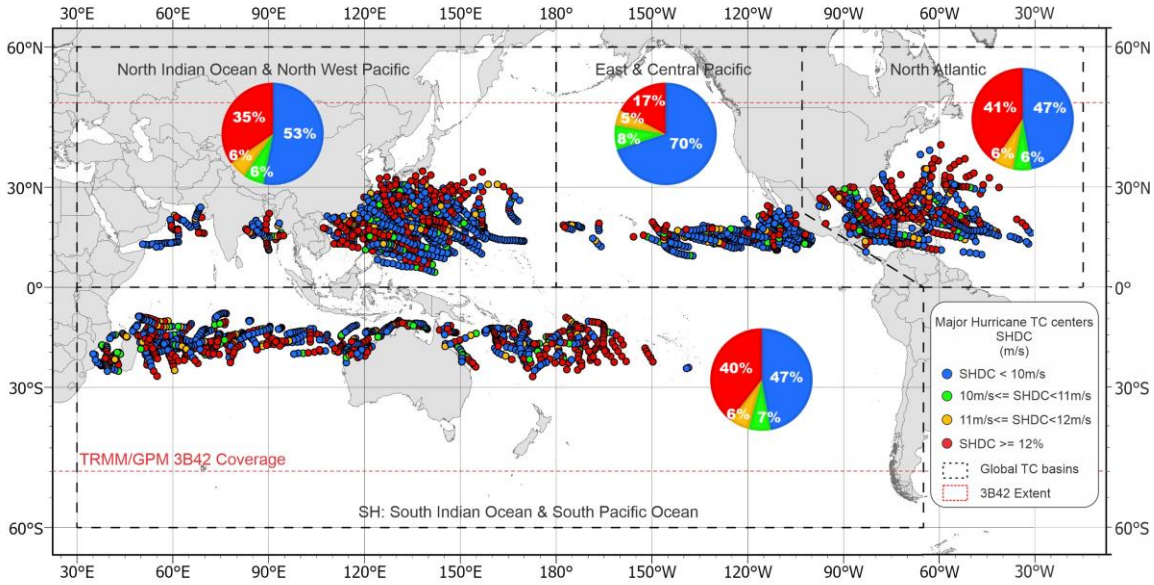

Figure 4-11 Global map showing the locations of the centers of major hurricanes for each SHIPS data point categorized by different SHDC levels. Pie charts illustrate the percentage of observations for each SHDC category in each basin.

Table 4-8: Number and percentage of major hurricane observations in different categories of SHDC

Variable	ATL	ECPA	NWP&NIO	SH	Total
SHDC < 10 $m.s^{-1}$	275 47.3%	369 70.0%	952 52.9%	514 47.2%	2,110 52.8%
10.0 $m.s^{-1}$ - 11.0 $m.s^{-1}$	33 5.7%	41 7.8%	118 6.6%	76 7.0%	268 6.7%
11.0 $m.s^{-1}$ - 12.0 $m.s^{-1}$	37 6.4%	26 4.9%	104 5.8%	70 6.4%	237 5.9%
SHDC > 12.0 $m.s^{-1}$	236 40.6%	91 17.3%	624 34.7%	430 39.4%	1,381 34.6%
Total of 3B42 observations for major hurricanes	581	527	1,798	1,090	3,996

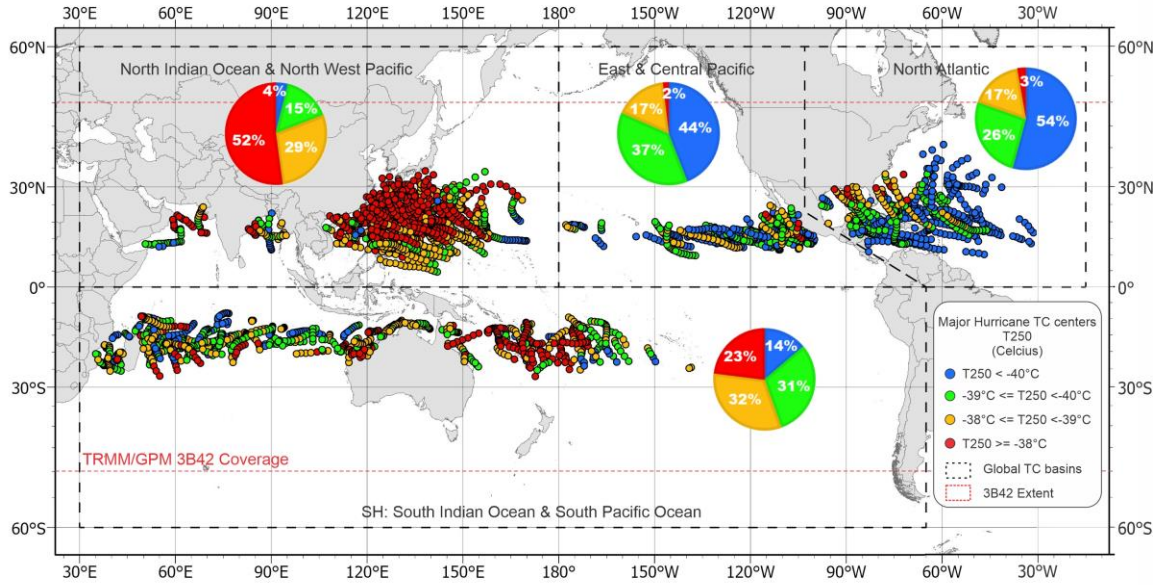

Figure 4-12 Global map showing the locations of the centers of major hurricanes for each SHIPS data point categorized by different T250 levels. Pie charts illustrate the percentage of observations for each T250 category in each basin.

Table 4-9: Number and percentage of major hurricane observations in different categories of T250

Variable	ATL	ECPA	NWP&NIO	SH	Total
T250 < -40°C	315 54.2%	232 44.0%	69 3.8%	150 13.8%	766 19.2%
From -39.0 to -40.0	152 26.2%	198 37.6%	275 15.3%	336 30.8%	961 24.0%
From -38.0 to -39.0	99 17.0%	88 16.7%	517 28.8%	353 32.4%	1,057 26.5%
T250 > -38°C	15 2.6%	9 1.7%	937 52.1%	251 23.0%	1,212 30.3%
Total of 3B42 observations for major hurricanes	581	527	1,798	1,090	3,996

4.5 Discussion

Previous inter-basin comparisons of azimuthal mean rain rates suggest that the main differences occur around the inner-core region. For instance, Lonfat et al. (2004) found that TCs in the NIO show larger rain rates than other basins within the inner 100-km radius, while ECPA TCs have less rain in the 250 to 350 km zone. In that study, the authors reported potential uncertainties due to the small number of samples and suggested that inter-basin differences could be associated with the interactions between the TC and its environment.

Our results, using 19-year satellite data, show that inter-basin differences can be found in the region up to 550-km from the TC center, with the most significant variations in the first 300 km and the inner-core region (0 -150km). However, for the first time in the literature, we found that in the inner-core, the Atlantic basin exhibits larger rainfall rates than other basins, particularly for the most intense TCs. This result contradicts previous inter-basin comparison results using shorter time series by Lonfat et al. (2004). Three main possible hypotheses may explain the Atlantic difference: (a) This variation could be explained by geometrical differences (e.g., size or area) between Atlantic hurricanes and those occurring in other basins; (b) Variation could be the result of differential TC intensities in this basin with respect to the others, and (c) Differences in the interactions between TCs and their environment may favor the increase of rainfall in this basin.

Concerning the first hypothesis, we computed the average RMR for the different global basins seeking size-related differences. Figure 4.13 shows the resulting RMRs categorized by basin and TC intensity. As expected, most of the samples in Central and East Pacific hurricanes show the shortest RMRs and Northwestern Pacific the largest. In

this analysis, Atlantic hurricanes exhibit an intermediate behavior, almost identical to the global average shown in Figure 4.13a. Therefore, a geometrical difference is an improbable reason to explain the wetter CAT3 to CAT5 hurricanes occurring in the Atlantic basin.

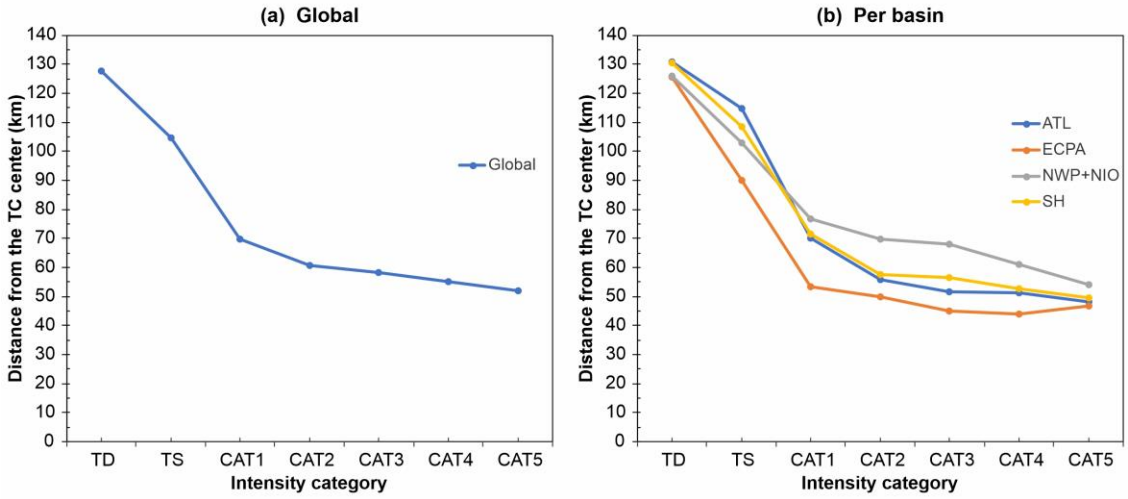

Figure 4-13 RMR as a function of TC intensity for (a) all global TCs; (b) for four different basins.

To test the second hypothesis, the average values of the maximum sustained wind speed are calculated and stratified by both TC intensity and geographic location. Table 4.3 shows that major hurricanes in NWP+NIO have the highest mean value of maximum sustained wind among all global basins. In these calculations, the Atlantic basin presents an intermediate behavior compared to the other basins. Therefore, the second hypothesis is also an improbable cause of the wetter major hurricanes occurring in the Atlantic basin.

The third hypothesis seeks an explanation based on the environmental interactions of TC occurring in the Atlantic basin relative to those present in other basins. Based on the results shown in Tables 4.3 to 4.9, we believe that the drier environment in the low to middle level troposphere (RHLO and RHMD) and colder air temperature at the upper level (T250) could induce a larger instability. Considering that under the presence of unstable

air, low relative humidity, and low T250, convection activity is highly promoted, our results indicate that ATL has more favorable environmental conditions associated with major hurricanes to produce convective rainfall in the inner core region. This interpretation is ratified by the higher value of EPOS, therefore higher value of CAPE, in ATL major hurricanes when compared to the other global basins. For this reason, we hypothesize that stronger convection is the main contributor to producing wetter inner-core conditions. This proposition is supported by the theory behind the classic hurricane models (e.g., Emanuel, 1986) that explain the release of energy through a moist adiabatic expansion that converts stored latent heat into sensible heat in an environment with higher potential buoyancy than its surrounding environment. In other words, in the presence of higher CAPE, hurricanes tend to produce more precipitation.

About the influence of environmental vertical wind shear (SHDC), Tables 4.3 and 5.8 show that the ATL basin has slightly higher shear magnitudes associated with major hurricanes than other basins in the northern hemisphere. It is well known that a weak vertical shear is a necessary condition for TC development. However, multiple studies also have demonstrated that when TCs interact with moderate amounts of wind shear, convection can be promoted, and TCs often take an asymmetric structure that leads to rainfall enhancement over favored sectors of the TC structure (Corbosiero and Molinary, 2002; Lonfat et al., 2004; Cecil, 2007; Pei and Jiang, 2018). Specifically, Molinari and Vollaro (2010 a, b) showed that highly sheared TCs produced 30% larger average CAPE versus relatively unsheared TCs through the asymmetric process. Therefore, the higher shear condition for ATL major hurricanes is favorable for stronger convection, thus heavier inner-core rain rates than major hurricanes in other northern hemisphere basins.

4.6 Conclusions

Using 19 years of TRMM/GPM 3B42 rainfall data for TCs, it is found that major (CAT3 to CAT5) hurricanes in the ATL basin have significantly larger mean rainfall rates in the inner core region than those in all other TC-prone basins. At the peak rainfall value in the inner core, the composite rainfall rate of major hurricanes in the ATL basin is higher than the global average by 6.4%, 13.9%, and 18.8% for CAT3, CAT4, and CAT5 hurricane, respectively.

To determine which atmospheric conditions were most likely responsible for the heavier rainfall rates in this basin, we tested three hypotheses: (a) geometrical differences, (b) differential TC wind speed intensity, and (c) special environmental conditions through the analysis of the SHIPS developmental database. Our results indicate that particular environmental conditions could explain this difference. We found that major hurricane in the ATL basin are associated with lower relative humidity in the low to middle level, lower upper level temperature, higher CAPE, and higher vertical wind shear magnitude in the environment. It is the general understanding that drier condition above the surface with lower upper-level temperature could promote convective instability, indicating by the higher CAPE values. Our results are consistent with previous studies showing that higher ambient shear could promote higher CAPE, therefore strong convection and heavier rain (Molinari and Vollaro 2010 a, b). Based on these results, it is suggested that the heavier inner-core rain in major hurricanes in the Atlantic basin is mainly associated with drier relative humidity in the low to middle troposphere, colder air temperature at upper-level, higher CAPE, and stronger vertical wind shear than major hurricanes in other basins.

It is clear that the above findings are merely from the observational perspective through the examination of composite satellite rainfall observations and SHIPS environmental parameter analyses. A detailed examination of the mechanisms that produce heavier inner-core rainfall rates in major hurricanes in the Atlantic basin must be addressed from the modeling perspective to establish detailed causal linkages and refine our understanding of the peculiarities observed in this basin. Future work will include analyzing additional environmental parameters from model re-analysis data to examine the influence of spatial distribution of these parameters on TC rain intensity. Another interesting point is that this study found that Atlantic TCs with intensity lower than major hurricane strength have weaker inner-core rain than those in other basins. Future study will be done to explore why the rainfall difference exists between weaker and stronger TCs in the Atlantic. The advent of new and more detailed information sources will contribute to the future improvement of this topic.

REFERENCES

Bagtasa, G. 2017: Contribution of Tropical Cyclones to Rainfall in the Philippines, *Journal of Climate*, 30(10), 3621-3633. https://doi.org/10.1175/JCLI-D-16-0150.1

Bregy, J. C., Maxwell, J. T., Robeson, S. M., Ortegren, J. T., Soulé, P. T., & Knapp, P. A., 2020: Spatiotemporal Variability of Tropical Cyclone Precipitation Using a High-Resolution, Gridded (0.25° × 0.25°) Dataset for the Eastern United States, 1948–2015, *Journal of Climate*, 33(5), 1803-1819. https://doi.org/10.1175/JCLI-D-18-0885.1

Burpee, R. W., and M. L. Black, 1989: Temporal and spatial variations of rainfall near the centers of two tropical cyclones. *Monthly Weather Review*, 117, 2204–2218.

Cecil, D. J., 2007: Satellite-derived rain rates in vertically sheared tropical cyclones. *Geophys. Res. Lett.*, 34, L02811, https://doi.org/10.1029/2006GL027942.

Chavas, D. R., and Emanuel, K. A., 2010: A QuikSCAT climatology of tropical cyclonesize, *Geophys. Res. Lett*., 37, L18816, https://doi.org/10.1029/2010GL044558.

Chen, S. S., J. A. Knaff, and F. D. Marks, 2006: Effects of vertical wind shear and storm motion on tropical cyclone rainfall asymmetries deduced from TRMM. *Monthly Weather Review*, 134, 3190–3208. https://doi.org/10.1175/MWR3245.1

Corbosiero, K. L., and J. Molinari, 2002: The effects of vertical wind shear on the distribution of convection in tropical cyclones. *Mon. Wea. Rev.*, 130, 2110–2123. https://doi.org/10.1175/1520-0493(2002)130%3C2110:TEOVWS%3E2.0.CO;2

Corbosiero, K. L., and J. Molinari, 2003: The relationship between storm motion, vertical wind shear, and convective asymmetries in tropical cyclones. *J. Atmos. Sci.*, 60, 366–376.

Christensen, J.H., K. Krishna Kumar, E. Aldrian, S.-I. An, I.F.A. Cavalcanti, M. de Castro, W. Dong, P. Goswami, A. Hall, J.K. Kanyanga, A. Kitoh, J. Kossin, N.-C. Lau, J. Renwick, D.B. Stephenson, S.-P. Xie and T. Zhou., Climate Phenomena and their Relevance for Future Regional Climate Change. In: Climate Change 2013, 2013: The Physical Science Basis. Contribution of Working Group I to the Fifth Assessment Report of the Intergovernmental Panel on Climate Change [Stocker, T.F., D. Qin, G.-K. Plattner, M. Tignor, S.K. Allen, J. Boschung, A. Nauels, Y. Xia, V. Bex, and P.M. Midgley (eds.)]. Cambridge University Press, Cambridge, United Kingdom and New York, NY, USA.

Dare, Richard & Davidson, Noel & Mcbride, John, 2012: Tropical Cyclone Contribution to Rainfall over Australia. *Monthly Weather Review*. 140. 3606-3619. https://doi.org/10.1175/MWR-D-11-00340.1..

DeMaria, M. and J. Kaplan, 1994: A Statistical Hurricane Intensity Prediction Scheme (SHIPS) for the Atlantic Basin. *Weather Forecasting*, 9, 209–220. https://doi.org/10.1175/1520-0434(1994)009<0209:ASHIPS>2.0.CO;2

DeMaria, M. and J. Kaplan, 1999: An Updated Statistical Hurricane Intensity Prediction Scheme (SHIPS) for the Atlantic and Eastern North Pacific Basins. *Weather Forecasting*, 14, 326–337. https://doi.org/10.1175/1520-0434(1999)014<0326:AUSHIP>2.0.CO;2

DeMaria, M., M. Mainelli, L.K. Shay, J.A. Knaff, and J. Kaplan, 2005: Further Improvements to the Statistical Hurricane Intensity Prediction Scheme (SHIPS). *Weather Forecasting*, 20, 531–543. https://doi.org/10.1175/WAF862.1

Emanuel, K.A., 1986: An air-sea interaction theory for tropical cyclones. Part I: Steady-state maintenance. *J. Atmos. Sci.*, 43, 585-604, https://doi.org/10.1175/1520-0469(1986)043 <0585:AASITF>2.0.CO;2

Emanuel, K. A., 1987: The dependence of hurricane intensity on climate. *Nature* 326, 483–-485, https://doi.org/10.1038/326483a0.

Emanuel, K., 2005: Increasing destructiveness of tropical cyclones over the past 30 years. *Nature* 436, 686–688, https://doi.org/10.1038/nature03906.

Englehart, P.J. and Douglas, A.V., 2001: The role of eastern North Pacific tropical storms in the rainfall climatology of western Mexico. *International Journal of Climatology*., 21, 1357-1370. https://doi.org/10.1002/joc.637.

Guzman, O. & Jiang, H., 2021: Heavier Inner-Core Rainfall of Major Hurricanes in the North Atlantic Basin Than in Other Global Basins, *Journal of Climate*, 34(14), 5707-5721. https://doi.org/10.1175/JCLI-D-20-0668.1.

Hill, K. A., and G. M. Lackmann, 2009: Influence of environmental humidity on tropical cyclone size. *Monthly Weather Review*, 137, 3294– 3315. https://doi.org/10.1175 /2009MWR2679.1.

Holland, G. J., 1980: An Analytic Model of the Wind and Pressure Profiles in Hurricanes, *Monthly Weather Review*, 108(8), 1212-1218. https://doi.org/10.1175/1520-0493(1980)108<1212:AAMOTW>2.0.CO;2

Holland, G. J.,1997: The Maximum Potential Intensity of Tropical Cyclones. *Jour. Atmos. Sci.*, 54, 2519–2541, https://doi.org/10.1175/15200469(1997)054<2519:TMPIOT >2.0.CO;2.

Holland, G. J., Belanger, J. I., & Fritz, A., 2010: A Revised Model for Radial Profiles of Hurricane Winds, *Monthly Weather Review*, 138(12), 4393-4401. https://doi.org/10.1175/ 2010MWR3317.1

Huffman, G. J., D.T. Bolvin, E.J. Nelkin, D.B. Wolff, R.F. Adler, G. Gu, Y. Hong, K.P. Bowman, and E.F. Stocker, 2007: The TRMM Multi-satellite Precipitation Analysis (TMPA): Quasi-Global, Multiyear, Combined-Sensor Precipitation Estimates at Fine Scales, J. Hydrometeor., 8, 38–55, https://doi.org/10.1175/JHM560.1.

Huffman, G. J., E.F. Stocker, D.T. Bolvin, E.J. Nelkin, Jackson Tan, 2019: GPM IMERG Final Precipitation L3 Half Hourly 0.1-degree x 0.1-degree V06, Greenbelt, MD, Goddard Earth Sciences Data and Information Services Center (GES DISC), Accessed: June 2021. https://doi.org/10.5067/GPM/IMERG/3B-HH/06

Huffman, G. J., D.T. Bolvin, D. Braithwaite, KL. Hsu, R.J. Joyce, C. Kidd, E.J. Nelkin, S, Sorooshian, E.F. Stocker, J Tan, D.B. Wolff, P. Xie., 2020: Integrated Multi-satellite Retrievals for the Global Precipitation Measurement (GPM) Mission (IMERG), Satellite Precipitation Measurement. Springer International Publishing. 1. 343-353. https://doi.org/10.1007/978-3-030-24568-9_19

IPCC, Climate Change: The Physical Science Basis. Contribution of Working Group I to the Fifth Assessment Report of the Intergovernmental Panel on Climate Change., 2013: United Kingdom and New York, NY, USA: Cambridge University Press, 1535.

Jiang, H., Halverson, J. B., and Zipser, E. J., 2008: The influence of environmental moisture on TRMM-derived tropical cyclone precipitation over land and ocean, *Geophys. Res. Lett.*, 35, L17806. https://doi.org/10.1029/2008GL034658.

Jiang, H., and E. J. Zipser, 2010: Contribution of tropical cyclones to the global precipitation from eight seasons of TRMM data: Regional, seasonal, and interannual variations. *J. Climate,* 23, 1526–1543. https://doi.org/10.1175/2009JCLI3303.1

Jiang, H., C. Liu, and E. J. Zipser., 2011: A TRMM-based Tropical Cyclone Cloud and Precipitation Feature Database, *J. Appl. Meteor. Climatol.*, 50, 1255-1274. https://doi.org/10.1175/2011JAMC2662.1.

Kaplan, J., and DeMaria, M., 1995: A Simple Empirical Model for Predicting the Decay of Tropical Cyclone Winds after Landfall, *Journal of Applied Meteorology and Climatology*, 34(11), 2499-2512. https://doi.org/10.1175/1520-0450(1995)034<2499:ASEMFP>2.0.CO;2

Kim, D., C. Ho, D.R. Park, J.C. Chan, and Y. Jung, 2018: The Relationship between Tropical Cyclone Rainfall Area and Environmental Conditions over the Subtropical Oceans. *J. Climate*, 31, 4605–4616, https://doi.org/10.1175/JCLI-D-17-0712.1

Kim, D., C.-H. Ho, H. Murakami, and D.-S. R. Park., 2021: Assessing the Influence of Large-Scale Environmental Conditions on the Rainfall Structure of Atlantic Tropical Cyclones: An Observational Study. *Journal of Climate*, 34(6), 2093-2106, https://doi.org/10.1175/JCLI-D-20-0376.

Kim D., 2020: Rainfall structure of tropical cyclone over the globe. Ph.D. Diss. Seoul National University.

Kimball, S. K., 2008: Structure and Evolution of Rainfall in Numerically Simulated Landfalling Hurricanes, *Monthly Weather Review*, 136(10), 3822-3847. https://doi.org/10.1175/2008MWR2304.1

Knapp, K. R., H. J. Diamond, J. P. Kossin, M. C. Kruk, C. J. Schreck, 2018: International Best Track Archive for Climate Stewardship (IBTrACS) Project, Version 4. Subset from 1998 to 2016. NOAA National Centers for Environmental Information. available in May 2021. https://doi.org/10.7289/v5nk3bzp

Kossin, J. P., Knapp, K. R., Vimont, D. J., Murnane, R. J., and Harper, B. A., 2007: A globally consistent reanalysis of hurricane variability and trends, *Geophys. Res. Lett*., 34, L04815, https://doi.org/10.1029/2006GL028836.

Knutson, T., McBride, J., Chan, J. et al., 2010: Tropical cyclones and climate change. *Nature Geosci*, 3, 157–163. https://doi.org/10.1038/ngeo779.

Knutson, T. R., J. J. Sirutis, G. A. Vecchi, S. Garner, M. Zhao, H.-S. Kim, M. Bender, R. E. Tuleya, I. M. Held, and G. Villarini, 2013: Dynamical downscaling projections of late 21st century Atlantic hurricane activity: CMIP3 and CMIP5 model-based scenarios. *J. Climate*, 26, 6591-6617. https://doi.org/10.1175/JCLI-D-12-00539.1

Knutson, T., and Coauthors, 2020: Tropical Cyclones and Climate Change Assessment: Part II: Projected Response to Anthropogenic Warming. *Bull. Amer. Meteor. Soc*., 101, E303–E322, https://doi.org/10.1175/BAMS-D-18-0194.1.

Lau, W. K. M., and Y. P. Zhou., 2012: Observed recent trends in tropical cyclone rainfall over the North Atlantic and the North Pacific, *J. Geophys. Res.*, 117, D03104, https://doi.org/10.1029/2011JD016510.

Landsea, C.W., B.A.Harper, K.Hoarau, and J.A.Knaff., 2006: Can we detect trends in extreme tropical cyclones?, *Science*, 313, 452-454. https://doi.org/10.1126/science.1128448

Larson, J., Y. Zhou, and R. W. Higgins., 2005: Characteristics of Landfalling Tropical Cyclones in the United States and Mexico: Climatology and Interannual Variability. *J. of Climate*, 18, 1247–1262, https://doi.org/10.1175/JCLI3317.1.

Lin, Y., Zhao, M. & Zhang, M., 2015: Tropical cyclone rainfall area controlled by relative sea surface temperature. *Nature Communications* 6, 6591. https://doi.org/10.1038/ncomms7591.

Lonfat, M., Marks, F. D. Jr., & Chen, S. S., 2004: Precipitation distribution in tropical cyclones using the Tropical Rainfall Measuring Mission (TRMM) microwave imager: A global perspective. *Monthly Weather Review*, 132(7), 1645–1660., https://doi.org/10.1175/1520-0493(2004)132<1645: PDITCU>2.0.CO;2

Lonfat, M., R. Rogers, T. Marchok, and F.D. Marks Jr., 2007: A parametric model for predicting hurricane rainfall. *Monthly Weather Review*, 135, 3086-3097, https://doi.org/10.1175/MWR3433.1

Matyas, C.J., 2010: Associations between the size of hurricane rain fields at landfall and their surrounding environments. *Meteorology and Atmospheric Physics* 106, 135–148. https://doi.org/10.1007/s00703-009-0056-1.

Matyas, C. J., 2013: Processes Influencing Rain-Field Growth and Decay after Tropical Cyclone Landfall in the United States, *J. Appl. Meteor. Climatol*., 52, 1085–1096, https://doi.org/10.1175/JAMC-D-12-0153.1.

Matyas, C. J., 2014: Conditions associated with large rain-field areas for tropical cyclones landfalling over Florida, *Physical Geography*, 35:2, 93-106, https://doi.org/10.1080/02723646.2014.893476

Park, D.-S.R., J. Kim, K. Kang, and C. C. Nam, 2016: Highlighting socioeconomic damages caused by weakened tropical cyclones in the Republic of Korea. *Nat. Hazards*, 82, 1301–1315, https://doi.org/10.1007/s11069-016-2244-x2

Patricola, C.M., and M.F. Wehner., 2018: Anthropogenic influences on major tropical cyclone events. *Nature*, 563, 339–346. https://doi.org/10.1038/s41586-018-0673-2.

Pei, Y., and Jiang, H., 2018: Quantification of precipitation asymmetries of tropical cyclones using 16-year TRMM observations. *Journal of Geophysical Research*: *Atmospheres*, 123, 8091–8114. https://doi.org/10.1029/2018JD028545

Peterson T. C., T. R. Karl, J. P. Kossin, K. E. Kunkel, J. H. Lawrimore, J. R. McMahon, R. S. Vose and X. Yin., 2014: Changes in weather and climate extremes: State of knowledge relevant to air and water quality in the United States, *Journal of the Air & Waste Management Association*, 64, 1096-2247, https://doi.org/10.1080/10962247.2013.851044.

Prat, O. P., & Nelson, B. R., 2016: On the Link between Tropical Cyclones and Daily Rainfall Extremes Derived from Global Satellite Observations, *Journal of Climate*, 29(17), 6127-6135. https://doi.org/10.1175/JCLI-D-16-0289.1

Rappaport, E. N., 2014: Fatalities in the United States from Atlantic tropical cyclones: New data and interpretation. *Bull. Amer. Meteor. Soc*., 95, 341–346, https://doi.org/10.1175/BAMS-D-12-00074.1.

Rappaport, E. N., 2000: Loss of Life in the United States Associated with Recent Atlantic Tropical Cyclones. *Bull. Amer. Meteor. Soc*., 81, 2065–2074, https://doi.org/10.1175/1520-0477(2000)081<2065:LOLITU>2.3.CO;2.

Ren, F., Wu, G., Dong, W., Wang, X., Wang, Y., Ai, W., and Li, W., 2006: Changes in tropical cyclone precipitation over China, *Geophysical Research Letters*, 33, L20702. https://doi.org/10.1029/2006GL027951.

Reynolds, R. W., T. M. Smith, C. Liu, D. B. Chelton, K. S. Casey, and M. G. Schlax, 2007: Daily high-resolution-blended analyses for sea surface temperature. *J. Climate*, 20, 5473–5496, doi:10.1175/2007JCLI1824.1.

Rodgers, E. B., Chang, S. W., & Pierce, H. F., 1994: A satellite observational and numerical study of precipitation characteristics in western North Atlantic tropical cyclones. *Journal of Applied Meteorology*, 33(2), 129–139. https://doi.org/10.1175/1520-0450(1994)033%3C0129: ASOANS%3E2.0.CO;2

Rogers, R., S. S. Chen, J. Tenerelli, and H. Willoughby, 2003: A numerical study of the impact of vertical shear on the distribution of rainfall in Hurricane Bonnie (1998). *Monthly Weather Review*, 131, 1577–1599, https://doi.org/10.1175/2546.1.

Scoccimarro E., G. Villarini, S. Gualdi, A. Navarra, G. Vecchi, K. Walsh and M. Zhao., 2017: Tropical cyclone rainfall changes in a warmer climate. Hurricanes and Climate Change, J. Collins and K. Walsh, Eds., Springer, 243-255. https://doi.org/10.1007/978-3-319-47594-3_10.

Shimada, U., H. Owada, M. Yamaguchi, T. Iriguchi, M. Sawada, K. Aonashi, M. DeMaria, and K.D. Musgrave, 2018: Further Improvements to the Statistical Hurricane Intensity Prediction Scheme Using Tropical Cyclone Rainfall and Structural Features. *Weather and Forecasting*, 33, 1587–1603. https://doi.org/10.1175/WAF-D-18-0021.1

Schumacher, A., M. DeMaria, and J. Knaff., 2013: Summary of the New Statistical-Dynamical Intensity Forecast Models for the Indian Ocean and Southern Hemisphere and Resulting Performance, JTWC Project Final Rep. 1-11.

Shea, D. J., and W. M. Gray., 1973: The Hurricane's Inner Core Region. I. Symmetric and Asymmetric Structure. *J. Atmos. Sci.*, 30, 1544–1564, https://doi.org/10.1175/1520-0469(1973)030<1544:THICRI>2.0.CO;2.

Stansfield, A. M., K. A. Reed, C. M. Zarzycki, P. A. Ullrich, and D. R. Chavas., 2020: Assessing Tropical Cyclones' Contribution to Precipitation over the Eastern United States and Sensitivity to the Variable-Resolution Domain Extent. *J. Hydrometeor*., 21, 1425–1445, https://doi.org/10.1175/JHM-D-19-0240.1.

Touma, D., Stevenson, S., Camargo, S. J., Horton, D. E., & Diffenbaugh, N. S., 2019: Variations in the intensity and spatial extent of tropical cyclone precipitation. *Geophysical Research Letters*, 46, 13992– 14002. https://doi.org/10.1029/2019GL083452

Uddin, M., Li, Y., Cheung, K. K., Nasrin, Z. M., Wang, H., Wang, L., & Gao, Z., 2019: Rainfall contribution of Tropical Cyclones in the Bay of Bengal between 1998 and 2016 using TRMM satellite data. *Atmosphere*, 10(11), 699.

Villarini G., D.A. Lavers, E. Scoccimarro, M. Zhao, M.F. Wehner, G. Vecchi, and T. Knutson., 2014: Sensitivity of tropical cyclone rainfall to idealized global scale forcings. *J. Climate*, 27(12). https://doi.org/10.1175/JCLI-D-13-00780.1.

Webster P. J., G. J. Holland, J. A. Curry, and H.-R. Chang., 2005: Changes in Tropical Cyclone Number, Duration, and Intensity in a Warming Environment. *Science* 309, Issue 5742, 1844-1846, https://doi.org/10.1126/science.1116448

Willoughby, H. E., 2012: Distributions and trends of death and destruction from hurricanes in the United States, 1900-2008. *Natural Hazards Review*. 13(1), 57-64.

Wingo, M. T., and D. J. Cecil, 2010: Effects of vertical wind shear on tropical cyclone precipitation. *Monthly Weather Review,* 138, 645– 662, doi:10.1175/2009MWR2921.1.

Xu, W., Jiang, H., & Kang, X., 2014: Rainfall asymmetries of tropical cyclones prior to, during, and after making landfall in South China and Southeast United States. Atmospheric Research, 139, 18-26. https://doi.org/10.1016/j.atmosres.2013.12.015

Yu, Z., Wang, Y., & Xu, H., 2015: Observed Rainfall Asymmetry in Tropical Cyclones Making Landfall over China, *Journal of Applied Meteorology and Climatology*, 54(1), 117-136. https://doi.org/10.1175/JAMC-D-13-0359.1

Yu, Z., Wang, Y., Xu, H., Davidson, N., Chen, Y., Chen, Y., & Yu, H., 2017: On the Relationship between Intensity and Rainfall Distribution in Tropical Cyclones Making Landfall over China. *Journal of Applied Meteorology and Climatology*, 56(10), 2883–2901. https://www.jstor.org/stable/26394289

Zhang Qiang, Xihui Gu, Peijun Shi, Vijay P. Singh, 2017: Impact of tropical cyclones on flood risk in southeastern China: Spatial patterns, causes and implications, *Global and Planetary Change*, Volume 150, 81-93, https://doi.org/10.1016/j.gloplacha.2017.02.004.

VITA

OSCAR F. GUZMAN REY

	Born, Bogotá. D.C, Colombia
1994-2000	B.S., Engineering in Geodesy and Mapping District University of Bogota FJC. Bogotá, Colombia
2004-2006	M.Sc., Meteorology National University of Colombia Bogotá, Colombia
2004-2018	Founder and Chief technical officer Datum Ingeniería SAS. Bogota, Colombia
2021-2022	Doctoral Candidate & Research Assistant Florida International University Miami, Florida
2021-Present	Founder and CEO Datum LLC. Miami, Florida.

PUBLICATIONS

Guzman, O., & Jiang, H. (2021). Heavier Inner-Core Rainfall of Major Hurricanes in the North Atlantic Basin Than in Other Global Basins, *Journal of Climate*, 34(14), 5707-5721.

Guzman, O. and H. Jiang, 2021: Global Increase in Tropical Cyclone Rain Rate. *Nature Communications*. 12, 5344.

Guzman, O., & Jiang, H. (2022). Climatology of Tropical Cyclone Rainfall Magnitude at Different Landfalling Stages. *Journal of Applied Meteorology and Climatology*.